

Spectral Analysis and Computation for Homogenization of Advection Diffusion Processes in Steady Flows

N. B. Murphy* and J. Xin

University of California at Irvine, Department of Mathematics,

340 Rowland Hall, Irvine, CA 92697-3875, USA

E. Cherkaev, J. Zhu, and K. M. Golden

University of Utah, Department of Mathematics,

155 S 1400 E, RM 233, Salt Lake City, UT 84112-0090, USA

(Dated: July 14, 2019)

Advective diffusion plays a key role in the transport of salt, heat, buoys and markers in geophysical flows, in the dispersion of pollutants and trace gases in the atmosphere, and even in the dynamics of sea ice floes influenced by winds and ocean currents. The long time, large scale behavior of such systems is equivalent to an enhanced diffusion process with an effective diffusivity matrix \mathfrak{D}^* . Three decades ago a Stieltjes integral representation for the homogenized matrix, involving a spectral measure of a self adjoint operator, was developed. However, analytical calculations of \mathfrak{D}^* have been obtained for only a few simple flows, and numerical computations of the effective behavior based on this spectral representation have apparently not been attempted. We overcome these limitations by providing a mathematical foundation for the computation of Stieltjes integral representations of \mathfrak{D}^* . We explore two different approaches and for each approach we derive new Stieltjes integral representations and rigorous bounds for the symmetric and antisymmetric parts of \mathfrak{D}^* , involving the molecular diffusivity and a spectral measure μ of a self-adjoint operator that depends on the characteristics of a randomly perturbed periodic flow. In discrete formulations of each approach, we express μ explicitly in terms of standard (or generalized) eigenvalues and eigenvectors of Hermitian matrices. We develop and implement an efficient numerical algorithm that combines beneficial numerical attributes of each approach. We use this method to compute the effective behavior for model flows and relate spectral characteristics to flow geometry and transport properties.

* University of Utah, Department of Mathematics, 155 S 1400 E, RM 233, Salt Lake City, UT 84112-0090,
USA

I. INTRODUCTION

The advective enhancement of diffusive transport of passive scalars by complex fluid flows plays a key role in many important processes in the global climate system [63] and Earth’s ecosystems [15]. Advection by geophysical fluids intensifies the dispersion and large scale transport of heat [41], pollutants [55], and nutrients [15, 24] diffusing in their environment. Advective processes also enhance the large scale transport of plankton [24], which is an important component of the food web that sustains life in the polar oceans. The transport of sea ice floes in the polar oceans is diffusive in nature over short time scales as floes bump against each other, yet can be influenced and enhanced by eddie fluxes, storms and prevailing winds in the atmosphere as well as ocean currents [31, 51, 52, 63, 64]. Thermal transport *through* sea ice, coupling the temperature field in the upper ocean to the lower atmosphere, can be enhanced due to the presence of convective fluid flow in the porous brine microstructure of sea ice [21, 30, 32, 62].

It was discovered in the early 1900s [60] that complex fluid flows transport passive scalars in much the same way as molecular diffusion. The mathematical description of this phenomenon [61] demonstrated that the long time, large scale behavior of a diffusing particle or tracer being advected by an *incompressible* fluid velocity field is equivalent to an enhanced diffusion process with an effective diffusivity matrix \mathfrak{D}^* . Describing the enhancement of the effective transport properties by fluid advection is a challenging problem with theoretical and practical importance in many fields of science and engineering, ranging from turbulent combustion [2, 12, 50, 59, 65, 66] to mass, heat, and salt transport in geophysical flows [41].

A broad range of mathematical techniques have been developed that reduce the analysis of complex fluid flows, with rapidly varying structures in space and time, to solving averaged or *homogenized* equations that do not have rapidly varying data, but involve effective parameters [11, 17, 18, 33–35, 48, 66]. Homogenization of the advection diffusion equation for passive scalar transport by stochastically stationary, time-independent, *mean-zero* fluid velocity fields was treated in [35]. This reduced the analysis of advective diffusion to solving a diffusion equation involving a homogenized temperature field and a constant effective diffusivity matrix \mathfrak{D}^* .

An important consequence of this analysis is that the effective diffusivity \mathfrak{D}^* is given in terms of a solution of the so-called “cell problem” [35], which can be written as a steady state

diffusion equation involving a skew-symmetric random matrix \mathbf{H} [3, 4, 17, 18]. By adapting the analytic continuation method of homogenization theory for composite materials [8, 22, 39], it was shown [3, 4] that the cell problem could be written in resolvent form involving a self-adjoint random operator acting on the Hilbert space of *curl-free vector fields*. This, in turn, led to a Stieltjes integral representation for the *symmetric* part of \mathfrak{D}^* , involving the Péclet number Pe of the flow and a *spectral measure* of the operator. A key feature of the integral representation for \mathfrak{D}^* is that parameter information in Pe is *separated* from the geometry of the fluid velocity field. The velocity field geometry is encoded in the spectral measure through its moments. This parameter separation has led [3, 4, 17, 18] to rigorous forward bounds for the diagonal components of \mathfrak{D}^* .

The mathematical framework developed in [35] was adapted [33, 48] to the case of a periodic, time-dependent fluid velocity field with *non-zero mean*. It was shown [48] that, depending on the strength of the fluctuations relative to the mean flow, the effective diffusivity matrix \mathfrak{D}^* can be constant or a function of both space and time. When \mathfrak{D}^* is constant, only its symmetric part appears in the homogenized equation as an enhancement in the diffusivity. However, when \mathfrak{D}^* is a function of space and time, its antisymmetric part also plays a key role in the homogenized equation. Based on [9, 10], the cell problem associated with a *time-independent* flow was transformed [48] into a resolvent formula involving a self-adjoint operator, acting on a Sobolev space [19, 37] of spatially periodic *scalar fields*, which is also a Hilbert space. This, in turn, led to a discrete Stieltjes integral representation for the *antisymmetric* part of \mathfrak{D}^* , involving the Péclet number of the flow and a spectral measure of the operator.

Such methods have been extended to steady flows where particles diffuse according to linear collisions [49], solute transport in porous media [9, 10], anelastic (weakly compressible) flows [36], as well as to the setting of a time-dependent fluid velocity field [5, 33, 44]. All these approaches yield integral representations of the symmetric and, when appropriate, the antisymmetric part of \mathfrak{D}^* . Variational formulations of the effective parameter problem for \mathfrak{D}^* are given in [4, 17, 18].

We now discuss the main contributions of the present work. In [3, 4], a Stieltjes integral representation and associated rigorous bounds were developed for the diagonal components of \mathfrak{D}^* (which are components of the *symmetric* part of \mathfrak{D}^*); the off-diagonal components were ignored. In [48], using a different method, a Stieltjes integral representation was developed

for the off-diagonal components of the *antisymmetric* part of \mathfrak{D}^* (the diagonal components are zero); no bounds were developed using the spectral representation. Here we adapt and extend the mathematical frameworks developed in both [3, 4] and [48] to the case of a time-independent randomly perturbed periodic flow. We obtain *new* Stieltjes integral representations and rigorous bounds for both the symmetric and antisymmetric parts of \mathfrak{D}^* – for both its diagonal and off-diagonal components. These integral representations achieve a separation of the geometry of the fluid velocity – through the spectral measures of self-adjoint operators – from the relevant material property of the fluid, its molecular diffusivity.

For each approach, we provide a mathematical foundation for the computation of Stieltjes integral representations for \mathfrak{D}^* , by developing discrete, matrix formulations of the effective parameter problem. The spectral measure in each of these two approaches is given explicitly in terms of the eigenvalues and eigenvectors of either a standard or generalized Hermitian eigenvalue problem. In general, the numerical implementation of the generalized eigenvalue problem is more computationally expensive than a standard eigenvalue problem [47]. However, the approach involving the standard problem involves a matrix that is larger by a factor of the dimension d compared to the matrix of the other approach involving the generalized problem. The numerical eigenvalue decomposition of a matrix is quite expensive, and high resolution of the discretized domain results in very large matrices. Therefore, it is important to develop an efficient way to numerically compute the spectral measure. We provide a detailed matrix analysis that demonstrates both approaches can be formulated in terms of a common *standard* eigenvalue problem involving a matrix with the *smaller size* encountered in the generalized eigenvalue problem, thus combining beneficial numerical attributes of both approaches.

In the continuum setting, the self-adjoint operators used in [3, 4] and [48] both involve the inverse of the negative Laplacian $(-\Delta)^{-1}$, which is given in terms of convolution with the Green's function for $\Delta = \nabla^2$ [56]. In the discrete setting, the negative matrix Laplacian is full-rank, hence invertible when Dirichlet boundary conditions are considered, for example. However, the matrix Laplacian is rank-deficient, hence non-invertible when periodic boundary conditions are considered. The matrix analysis discussed above in the full-rank setting reveals useful structure with minimal effort. However, the matrix analysis of the rank-deficient setting is quite a bit more involved, but necessary, since here we investigate advection enhanced diffusion by periodic flows. This analysis demonstrates the two approaches considered yield

equivalent spectral representations for the effective diffusivity matrix \mathfrak{D}^* .

We utilize this unified mathematical framework to compute the effective diffusivity matrix \mathfrak{D}^* for some model periodic and randomly perturbed periodic flows, and describe the behavior of the enhancement of diffusive transport in terms of the behavior of the spectral measure. There are several approaches to computing \mathfrak{D}^* , including numerical solution of the underlying cell problem PDE [48], Monte Carlo methods [13], and a method accurate for large Péclet numbers [23]. Our work here was not motivated by a goal of finding a faster or more accurate method of computing \mathfrak{D}^* , although our approach does provide an alternative way of computing \mathfrak{D}^* and is quite robust.

Instead, for randomly perturbed periodic flows, our spectral method for computing \mathfrak{D}^* is set apart from more traditional methods in that it was developed not only to study homogenized behavior but to investigate *spectral statistics*. Indeed, the effective behavior of the system, as encapsulated by \mathfrak{D}^* , is closely connected to the statistical behavior of the spectral measure which, in turn, is determined by the statistics of the random eigenvalues and eigenvectors. Consequently, the spectral method enables the homogenization of advection diffusion processes to be viewed through the lens of random matrix theory. In the theory of two-phase composite materials, this approach has led to a new understanding of critical behavior of transport in high contrast composite materials as a percolation threshold is approached. The focus on calculating spectral measures in Stieltjes representations for composite materials through computation of eigenvalues and eigenvectors of random matrices led to the realization that critical behavior of classical transport at a percolation threshold can be viewed as a type of Anderson transition [45]. In the analysis enabled by the spectral approach for composites, we investigated the appearance, for example, of localization phenomena, mobility edges, and universal Wigner-Dyson statistics of the Gaussian Orthogonal Ensemble for the eigenvalue spacing distribution. The results in this manuscript lay the mathematical and computational groundwork for such investigations in the context of advection diffusion processes, where the geometry of the fluid velocity field plays the role of the microstructural properties of the composite. Our results in this direction are somewhat outside the scope of the current paper and will be published elsewhere, although we consider here some spectral characteristics and their relations to flow geometry and transport properties.

As another example of how the present work enables applications to geophysics, we consider advection diffusion within sea ice. The enhancement of the effective thermal conductivity of

sea ice due to the presence of convective fluid flow has long been known from an observational perspective [21, 32, 62]. The authors are unaware, though, of any predictive, theoretical works on this enhancement. In [30] the effective thermal conductivity of sea ice in the presence of *bulk* fluid convection is investigated, by applying the results developed here. Using Stieltjes integral representations, a series of bounds on the effective thermal conductivity were obtained for model flows using Padé approximants and the analytic continuation method, in terms of the Péclet number.

Motivated by the theoretical findings in the current work, in [44] we generalized the results given here to the setting of a time-dependent fluid velocity field $\mathbf{u} = \mathbf{u}(t, \mathbf{x})$. Furthermore we used different, abstract methods of functional analysis to generalize the equivalence results summarized in Theorem 5, Corollary 6, Lemma 9, and Theorem 10 of the current work to the continuum, steady and dynamic settings.

In order to streamline the presentation leading to the numerical results, we have placed in an appendix the development of integral representations for effective diffusivities using the approach introduced in [3, 4] — for both the continuum and discrete settings. The matrix analysis of the rank deficient setting and the equivalence results discussed above have also been placed in the appendix. Comments on the notation used throughout this manuscript are given in Appendix B.

II. HOMOGENIZATION OF THE ADVECTION DIFFUSION EQUATION

The dispersion of a passive scalar with density ϕ diffusing in a fluid with molecular diffusivity ε and being advected by a mean-zero incompressible velocity field \mathbf{u} satisfying $\nabla \cdot \mathbf{u} = 0$ and $\langle \mathbf{u} \rangle = 0$ is described by the advection diffusion equation

$$\phi_t(t, \mathbf{x}) = \mathbf{u}(\mathbf{x}) \cdot \nabla \phi(t, \mathbf{x}) + \varepsilon \Delta \phi(t, \mathbf{x}), \quad \phi(0, \mathbf{x}) = \phi_0(\mathbf{x}), \quad \mathbf{x} \in \mathbb{R}^d, \quad t > 0, \quad (1)$$

with initial density $\phi_0(\mathbf{x})$ given. Here, $\langle \cdot \rangle$ denotes volume averaging over the period cell \mathcal{V} , ϕ_t denotes partial differentiation of ϕ with respect to time t , $\Delta = \nabla \cdot \nabla = \nabla^2$ is the Laplacian, $\varepsilon > 0$, d is the system dimension, and we denote by 0 the null element in all linear spaces in question. Moreover, $\xi \cdot \zeta = \xi^\dagger \zeta$ and \dagger is the operation of complex-conjugate-transpose, with $\xi \cdot \xi = |\xi|^2$. Later, we will extensively use this form of the dot product over complex fields, with built in complex conjugation. However, we emphasize that all quantities considered in

this section are *real-valued*. We assume for now that the time-independent fluid velocity field \mathbf{u} is spatially periodic on the region $\mathcal{V} \subset \mathbb{R}^d$. Later, we will discuss the case of an array of randomly perturbed, periodic flows.

The long time, large scale dispersion of passive scalars can be described [61] by an effective diffusivity matrix \mathfrak{D}^* . An explicit representation for \mathfrak{D}^* can be found using methods of homogenization theory [7, 46]. These methods have demonstrated that the averaged or *homogenized* behavior of the advection diffusion equation in (1) is determined by a diffusion equation involving an averaged scalar density $\bar{\phi}$ and a (constant) effective diffusivity matrix \mathfrak{D}^* [35]

$$\bar{\phi}_t(t, \mathbf{x}) = \nabla \cdot [\mathfrak{D}^* \nabla \bar{\phi}(t, \mathbf{x})], \quad \bar{\phi}(0, \mathbf{x}) = \phi_0(\mathbf{x}). \quad (2)$$

The components \mathfrak{D}_{jk}^* , $j, k = 1, \dots, d$, of \mathfrak{D}^* are given by [35]

$$\mathfrak{D}_{jk}^* = \varepsilon \delta_{jk} + \langle u_j \chi_k \rangle, \quad (3)$$

The function χ_j in (3) satisfies a cell problem which is a steady state advection diffusion equation with a forcing term involving u_j , the j th component of the fluid velocity field \mathbf{u} [18, 35],

$$\mathbf{u} \cdot \nabla \chi_j + \varepsilon \Delta \chi_j = -u_j, \quad \langle \nabla \chi_j \rangle = 0. \quad (4)$$

Equations (2)–(4) follow from the assumption that the length scale associated with spatial variations of the initial density ϕ_0 is much larger than the length scale of spatial variations associated with the fluid velocity field \mathbf{u} [18, 35] (separation of scales). This information is incorporated into equation (1) by introducing a small dimensionless parameter $\delta \ll 1$ and writing [35]

$$\phi(0, \mathbf{x}) = \phi_0(\delta \mathbf{x}). \quad (5)$$

Anticipating that ϕ will have diffusive dynamics as $t \rightarrow \infty$, space and time are rescaled by $\mathbf{x} \mapsto \mathbf{x}/\delta$ and $t \mapsto t/\delta^2$. As $\delta \rightarrow 0$, the associated solution $\phi^\delta(t, \mathbf{x}) = \phi(t/\delta^2, \mathbf{x}/\delta)$ of equation (1) (in the rescaled variables) converges to $\bar{\phi}(t, \mathbf{x})$ which satisfies equation (2). The convergence is in an L^2 sense that depends on the technical assumptions made about the fluid velocity field \mathbf{u} [4, 17, 18, 33, 35, 48].

We emphasize that the cell problem in (4) involves only the fast variable \mathbf{x}/δ [35]. Other space-time scalings have also been considered, which have led to space-time dependent

\mathfrak{D}^* [48] and even anomalous diffusive dynamics [33]. Homogenization theorems for space-time dependent fluid velocity fields are treated in [11, 33, 48].

In our analysis of the effective diffusivity matrix \mathfrak{D}^* , it is beneficial to use non-dimensional parameters. We therefore assume that equation (1) has been non-dimensionalized as follows. Let ℓ and τ be typical length and time scales associated with the problem of interest. Mapping to the non-dimensional variables $t \mapsto t/\tau$ and $\mathbf{x} \mapsto \mathbf{x}/\ell$, one finds that ϕ satisfies the advection diffusion equation in (1) with a non-dimensional molecular diffusivity and fluid velocity field,

$$\varepsilon \mapsto \tau \varepsilon / \ell^2, \quad \mathbf{u} \mapsto \tau \mathbf{u} / \ell. \quad (6)$$

This demonstrates by non-dimensionalizing equation (1), the fluid velocity field \mathbf{u} is, in turn, divided by a quantity with dimensions of velocity and the molecular diffusivity is divided by a quantity with dimensions of velocity multiplied by spatial length. It is convenient to choose the rescaled \mathbf{u} and ε in a way that captures information about the fluid velocity field. However, it is also convenient to choose these rescaled variables in a way that *separates* the rescaled ε from the *geometry* of the flow; this leads to mathematically and physically meaningful properties of rigorous bounds for \mathfrak{D}^* which follow from the analytic structure of Stieltjes integral representations for \mathfrak{D}^* [4, 6] — discussed in Section III below.

We accomplish both of these goals as follows. Define the dimensional fluid velocity field by $\mathbf{u} = u_0 \mathbf{v}$, where the parameter u_0 has dimensions of velocity and represents the “flow strength” of \mathbf{u} which is independent of the geometry of the flow; the flow geometry is encapsulated in the non-dimensional vector field \mathbf{v} . With these definitions, we choose reference scales τ and ℓ in equation (6) to satisfy $u_0 = \ell/\tau$ so that $\mathbf{u} \mapsto \mathbf{v}$ and $\varepsilon \mapsto \varepsilon/u_0 \ell$. For example, in Section V we compute \mathfrak{D}^* for *BC*-flow [11] having dimensional fluid velocity field $\mathbf{u} = u_0 (C \cos y, B \cos x)$, where the flow strength $u_0 \in (0, \infty)$ is independent of the non-dimensional parameters $B, C \in [0, 1]$ which determine the streamline geometry of \mathbf{u} .

An example of a non-dimensional, parameter that compares the rate of scalar advection to the rate of diffusion is the Péclet number. We define it by the ratio $Pe = \ell u_0 / \varepsilon$, although other definitions have been used [33, 36]. The advection and diffusion dominated regimes are characterized by $Pe \gg 1$ and $Pe \ll 1$, respectively. Therefore, our choice of the rescaled ε satisfies $Pe = 1/\varepsilon$.

The *parameter separation* between Pe and the geometry of the flow is important for

rigorous upper and lower Padé approximant bounds for \mathfrak{D}^* [4, 43]. Padé approximants of \mathfrak{D}^* are given in terms of ratios of polynomials [6] $P(z)/Q(z)$, where $z = Pe^2$, $0 < z < \infty$, and the coefficients of these polynomials depend on the moments of a *spectral measure* that, in turn, depend on the fluid velocity field \mathbf{u} [4, 43]. For example, when \mathbf{u} is given by *BC*-flow the moments of the measure depend [43] on the parameters B and C . Our numerical investigations have shown if the non-dimensionalization of equation (1) is chosen in a way that the variable z also depends on the flow geometry through the ratio B/C , then this gives rise [43] to *positive real* roots for the polynomials $P(z)$ and $Q(z)$. This, in turn, gives rise to positive real roots and poles in the (rigorous) Padé approximant bounds for \mathfrak{D}^* , which is not physically or mathematically consistent with the known behavior of \mathfrak{D}^* [11, 17, 33, 48]. This demonstrates the importance of *parameter separation* between z and the flow geometry for Padé approximant bounds for \mathfrak{D}^* .

This way of non-dimensionalizing equation (1) is also convenient in the case of a time-dependent fluid velocity field [44], where the parameter u_0 again represents the flow strength and the vector field \mathbf{v} encapsulates the *geometric and dynamical* properties of the flow. For example, the space-time periodic flow with velocity field $\mathbf{u} = u_0((C \cos y, B \cos x) + \cos t (\gamma \sin y, \beta \sin x))$ has dynamical behavior exhibiting Lagrangian chaos [11, 44]. Here, the flow strength $u_0 \in (0, \infty)$ is independent of the parameters $B, C, \gamma, \beta \in [0, 1]$ which determine the geometric and dynamical properties of \mathbf{u} . This choice of non-dimensionalization gives a clearer interpretation of the advection and diffusion dominated regimes in terms of $Pe = 1/\varepsilon$ than that given in [44]. A detailed discussion of various non-dimensionalizations of equation (1) is given in [33, 36].

III. HILBERT SPACE AND INTEGRAL REPRESENTATIONS

In this section, we adapt and extend a method [9, 10, 48] which provides Stieltjes integral representations for the effective diffusivity matrix \mathfrak{D}^* . We do so by providing functional formulas for the symmetric \mathfrak{S}^* and antisymmetric \mathfrak{A}^* parts of \mathfrak{D}^* , involving the scalar field χ_j in equation (4). We also provide a Sobolev space formulation of the effective parameter problem [48] which yields a resolvent formula for χ_j , involving a self-adjoint operator that depends only on the fluid velocity field \mathbf{u} . This and the spectral theorem [53, 58] yield Stieltjes integral representations for \mathfrak{S}^* and \mathfrak{A}^* involving a spectral measure of the operator.

Consider the Hilbert space \mathcal{H} ,

$$\mathcal{H} = \{f \in L^2(\mathcal{V}, \nu) : f(\mathbf{x}) \text{ is periodic in } \mathcal{V} \text{ and } \langle f \rangle = 0\}, \quad (7)$$

where ν is the Lebesgue measure on \mathbb{R}^d , restricted to \mathcal{V} , and the σ -algebra associated with the underlying measure space is generated by the Lebesgue measurable subsets of \mathbb{R}^d . The Hilbert space \mathcal{H} is equipped with a sesquilinear inner product $\langle \cdot, \cdot \rangle$ defined by $\langle f, h \rangle = \langle \bar{f} h \rangle$, with $\langle h, f \rangle = \overline{\langle f, h \rangle}$ for $f, h \in \mathcal{H}$, which induces a norm $\|\cdot\|$ defined by $\|f\| = \langle f, f \rangle^{1/2}$ and $f \in \mathcal{H}$ implies $\|f\| < \infty$.

One could also consider a random fluid flow filling all of \mathbb{R}^d , with a velocity field \mathbf{u} determined by the probability space (Ω, P) with σ -algebra generated by the sets $\{\mathbf{u}(\mathbf{x}) \in B\}$, where $\mathbf{x} \in \mathbb{R}^d$ and B is a Borel subset of \mathbb{R}^d [4]. Here, Ω is the set of all geometric realizations of \mathbf{u} , which is indexed by the parameter $\omega \in \Omega$ representing one particular geometric realization, and P is the associated probability measure. The underlying Hilbert space in this case can be taken to be $\mathcal{H} = L^2(\Omega, P)$, i.e., the space of all P -measurable complex-valued scalar functions ξ satisfying $\|\xi\| = \langle |\xi|^2 \rangle^{1/2} < \infty$, where $\langle \cdot \rangle$ denotes ensemble averaging and the underlying sesquilinear inner-product is defined by $\langle \xi, \zeta \rangle = \langle \bar{\xi} \zeta \rangle$. In this case, one could consider a random fluid flow with a velocity field \mathbf{u} that is stationary [35] or ergodic [3, 4], for example, with regularity conditions at infinity, i.e., as $|\mathbf{x}| \rightarrow \infty$. In these cases, one works with an infinite medium directly, which presents substantial computational difficulties.

A more computationally tractable random system is given by a $n \times n$ array of randomly perturbed periodic flows [18]. In this case, the σ -algebra associated with the underlying probability space is generated by the Lebesgue measurable subsets of \mathbb{R}^d . Here, the Hilbert space \mathcal{H} is given by equation (7) and averaged quantities depend on the realization of the random medium because $\langle \cdot \rangle$ is given by volume averaging over the period cell \mathcal{V} [18]. The effective diffusivity matrix \mathfrak{D}^* is obtained by taking an infinite volume limit, $\mathfrak{D}^* = \lim_{n \rightarrow \infty} \mathfrak{D}_n^*$, of the finite volume effective diffusivity matrix \mathfrak{D}_n^* and evoking an ergodic theorem [18, 22]. Numerically, by the law of large numbers [16], it is natural to spatially average each statistical trial and then ensemble average over all of the sampled random realizations. This is the approach we take here.

In any case, once the Hilbert space \mathcal{H} is established, with associated average $\langle \cdot \rangle$, inner-product $\langle \cdot, \cdot \rangle$, and norm $\|\cdot\|$, the spectral theory presented in the remainder of this section progresses independent of the underlying details, as it lays on an axiomatic foundation [58].

For the sake of numerical tractability, we will assume that the Hilbert space \mathcal{H} is given by equation (7). The fluid velocity field \mathbf{u} can be assumed to represent a periodic or randomly perturbed periodic flow. Now, consider the Sobolev space $\mathcal{H}^{1,2}$, which itself is a Hilbert space [9, 10],

$$\mathcal{H}^{1,2} = \{f \in \mathcal{H} : \|f\|_{1,2} < \infty, \langle f \rangle = 0\}, \quad \|f\|_{1,2} = \langle |\nabla f|^2 \rangle^{1/2}, \quad (8)$$

where $\|\cdot\|_{1,2}$ is the norm induced by the underlying sesquilinear inner-product $\langle \cdot, \cdot \rangle_{1,2}$ defined by $\langle f, h \rangle_{1,2} = \langle \nabla f \cdot \nabla h \rangle$, with $\langle h, f \rangle_{1,2} = \overline{\langle f, h \rangle}_{1,2}$ (recall $\xi \cdot \zeta = \xi^\dagger \zeta$ includes complex conjugation).

Recall the definition of the components $\mathfrak{D}_{jk}^* = \varepsilon \delta_{jk} + \langle u_j \chi_k \rangle$, $j, k = 1, \dots, d$, of the effective diffusivity matrix \mathfrak{D}^* in (3). Rewrite the functional $\langle u_j \chi_k \rangle$ as [48],

$$\langle u_j \chi_k \rangle = \langle [\Delta \Delta^{-1} u_j] \chi_k \rangle = -\langle \nabla \Delta^{-1} u_j \cdot \nabla \chi_k \rangle = -\langle \Delta^{-1} u_j, \chi_k \rangle_{1,2}, \quad (9)$$

where we have integrated by parts and used the periodicity of the functions u_j and χ_k . Here, Δ^{-1} is based on convolution with the Green's function for the Laplacian Δ [56]. The symmetric \mathfrak{S}^* and antisymmetric \mathfrak{A}^* parts of the effective diffusivity matrix \mathfrak{D}^* are defined by

$$\mathfrak{D}^* = \mathfrak{S}^* + \mathfrak{A}^*, \quad \mathfrak{S}^* = \frac{1}{2} (\mathfrak{D}^* + [\mathfrak{D}^*]^T), \quad \mathfrak{A}^* = \frac{1}{2} (\mathfrak{D}^* - [\mathfrak{D}^*]^T). \quad (10)$$

Substituting into equation (9) the expression $-u_j = \mathbf{u} \cdot \nabla \chi_j + \varepsilon \Delta \chi_j$ for $-u_j$ in (4) yields the following functional formulas for the components \mathfrak{S}_{jk}^* and \mathfrak{A}_{jk}^* , $j, k = 1, \dots, d$, of \mathfrak{S}^* and \mathfrak{A}^*

$$\mathfrak{S}_{jk}^* = \varepsilon(\delta_{jk} + \langle \chi_j, \chi_k \rangle_{1,2}), \quad \mathfrak{A}_{jk}^* = \langle A \chi_j, \chi_k \rangle_{1,2}, \quad A = \Delta^{-1}[\mathbf{u} \cdot \nabla]. \quad (11)$$

Due to the incompressibility of the fluid velocity field, $\nabla \cdot \mathbf{u} = 0$, the operator A is antisymmetric on $\mathcal{H}^{1,2}$, i.e., $\langle A \xi, \zeta \rangle_{1,2} = -\langle \xi, A \zeta \rangle_{1,2}$ for all $\xi, \zeta \in \mathcal{H}^{1,2}$ (see equation (C1)). Since the scalar fields χ_j and $A \chi_j$ are *real-valued*, we have that $\langle \chi_j, \chi_k \rangle_{1,2} = \langle \chi_k, \chi_j \rangle_{1,2}$ and $\mathfrak{A}_{kj}^* = \langle A \chi_k, \chi_j \rangle_{1,2} = -\langle \chi_k, A \chi_j \rangle_{1,2} = -\langle A \chi_j, \chi_k \rangle_{1,2} = -\mathfrak{A}_{jk}^*$, confirming that \mathfrak{S}^* is symmetric and \mathfrak{A}^* is antisymmetric, with $\mathfrak{A}_{kk}^* = 0$.

Applying the operator Δ^{-1} to both sides of the cell problem $\varepsilon \Delta \chi_j + \mathbf{u} \cdot \nabla \chi_j = -u_j$ in equation (4) yields the following resolvent formula for χ_j involving the operator A in (11),

$$\chi_j = (\varepsilon + A)^{-1} g_j, \quad g_j = (-\Delta)^{-1} u_j. \quad (12)$$

Substituting the resolvent formula for χ_j in (12) into the bilinear functionals in equation (11) yields

$$\begin{aligned}\mathfrak{S}_{jk}^* &= \varepsilon(\delta_{jk} + \langle (\varepsilon + A)^{-1}g_j, (\varepsilon + A)^{-1}g_k \rangle_{1,2}), \\ \mathfrak{A}_{jk}^* &= \langle A(\varepsilon + A)^{-1}g_j, (\varepsilon + A)^{-1}g_k \rangle_{1,2}.\end{aligned}\quad (13)$$

Since \mathcal{V} is a bounded domain, the linear operator Δ^{-1} is bounded on \mathcal{H} with bounded operator norm $\|\Delta^{-1}\| < \infty$ [56]. When $|\mathbf{u}|$ is uniformly bounded on the period cell \mathcal{V} , $\sup_{\mathbf{x} \in \mathcal{V}} |\mathbf{u}(\mathbf{x})| < \infty$, the linear operator A is bounded on $\mathcal{H}^{1,2}$, with (see equations (C2) and (C3))

$$\|A\|_{1,2} \leq [\|\Delta^{-1}\| \sup_{\mathbf{x} \in \mathcal{V}} |\mathbf{u}(\mathbf{x})|^2]^{1/2} < \infty, \quad (14)$$

where $\|A\|_{1,2}$ denotes the operator norm of A induced by the norm $\|\cdot\|_{1,2}$ in equation (8). All of the fluid velocity fields that we consider in our numerical computations of \mathfrak{D}^* in Section V are uniformly bounded. More generally, for $u_k \in \mathcal{H}$, $k = 1, \dots, d$, the operator A is compact on $\mathcal{H}^{1,2}$ [9, 10, 48], hence bounded [56]. It follows that $M = -\imath A$, where $\imath = \sqrt{-1}$, is a bounded linear operator on $\mathcal{H}^{1,2}$ with $\|M\|_{1,2} = \|A\|_{1,2} < \infty$. Moreover, the skew-symmetry of A and the sesquilinearity of the $\mathcal{H}^{1,2}$ -inner-product imply that M is also symmetric, $\langle Mf, h \rangle_{1,2} = \langle f, Mh \rangle_{1,2}$. The bounded linear symmetric operator M with domain $\mathcal{H}^{1,2}$ is *self-adjoint* [53, 58].

The spectrum Σ of the self-adjoint operator M is real-valued, with spectral radius equal to its operator norm [53], i.e.,

$$\Sigma \subseteq [-\|A\|_{1,2}, \|A\|_{1,2}]. \quad (15)$$

The spectral theorem for bounded linear self-adjoint operators in Hilbert space states that there is a one-to-one correspondence between the operator M and a family of self-adjoint projection operators $\{Q(\lambda)\}_{\lambda \in \Sigma}$ — the resolution of the identity — satisfying [58]

$$\lim_{\lambda \rightarrow \inf \Sigma} Q(\lambda) = 0, \quad \lim_{\lambda \rightarrow \sup \Sigma} Q(\lambda) = I. \quad (16)$$

Furthermore, for all $\xi, \zeta \in \mathcal{H}^{1,2}$, the *complex-valued* function of the spectral variable λ defined by $\mu_{\xi\zeta}(\lambda) = \langle Q(\lambda)\xi, \zeta \rangle_{1,2}$ has real and imaginary parts that are of bounded variation [58]. Therefore, there is a *complex* Stieltjes measure $\mu_{\xi\zeta}$ associated with $\mu_{\xi\zeta}(\lambda)$ [20, 57, 58].

The spectral theorem also states, for all complex-valued functions $f \in L^2(\mu_{\xi\xi})$ and $h \in L^2(\mu_{\zeta\zeta})$, there exist linear operators denoted by $f(M)$ and $h(M)$ which are defined in terms of the bilinear functional $\langle f(M)\xi, h(M)\zeta \rangle_{1,2}$ [58]. In particular, this functional has the following Radon–Stieltjes integral representation involving the Stieltjes measure $\mu_{\xi\xi}$, for all $\xi, \zeta \in \mathcal{H}^{1,2}$,

$$\langle f(M)\xi, h(M)\zeta \rangle_{1,2} = \int_{-\infty}^{\infty} \overline{f}(\lambda) h(\lambda) d\mu_{\xi\xi}(\lambda), \quad \mu_{\xi\xi}(\lambda) = \langle Q(\lambda)\xi, \zeta \rangle_{1,2}, \quad (17)$$

where the integration is over the spectrum Σ of M [53, 58] and \overline{f} denotes complex conjugation of the scalar function f . Since the Stieltjes measure $\mu_{\xi\xi}$ has the property [58] $\int_a^b d\mu_{\xi\xi}(\lambda) = \mu_{\xi\xi}(b) - \mu_{\xi\xi}(a)$, equation (16) implies that the mass $\mu_{\xi\xi}^0$ of the measure $\mu_{\xi\xi}$ is given by

$$\mu_{\xi\xi}^0 = \int_{-\infty}^{\infty} d\mu_{\xi\xi}(\lambda) = \int_{-\infty}^{\infty} d\langle Q(\lambda)\xi, \zeta \rangle_{1,2} = \langle \xi, \zeta \rangle_{1,2}, \quad (18)$$

which is bounded in the sense that $|\mu_{\xi\xi}^0| \leq \|\xi\|_{1,2} \|\zeta\|_{1,2} < \infty$ for all $\xi, \zeta \in \mathcal{H}^{1,2}$. Due to the sesquilinearity of the inner-product and the fact that the projection operator $Q(\lambda)$ is self-adjoint on $\mathcal{H}^{1,2}$, the complex-valued function $\mu_{\xi\xi}(\lambda)$ satisfies $\mu_{\xi\xi}(\lambda) = \overline{\mu}_{\xi\xi}(\lambda)$ and $\mu_{\xi\xi}(\lambda) = \|Q(\lambda)\xi\|^2$, so $\mu_{\xi\xi}$ is a *positive* measure. The formulas in equations (16)–(18) will be used several times throughout this manuscript to clarify and streamline the development of various Stieltjes integral representations for the effective diffusivity matrix \mathfrak{D}^* . They will be used both in the continuum setting, as well as the discrete setting which leads to an efficient numerical algorithm for our computation of spectral representations for \mathfrak{D}^* for various model fluid flows in Section V.

We are now ready to present the main results of this section. For notational simplicity, denote the complex-valued function $\mu_{jk}(\lambda) = \langle Q(\lambda)g_j, g_k \rangle$, instead of $\mu_{g_j g_k}(\lambda)$, where $g_j = (-\Delta)^{-1}u_j$ is defined in (12). Denote the real and imaginary parts of the function $\mu_{jk}(\lambda)$ by $\text{Re } \mu_{jk}(\lambda)$ and $\text{Im } \mu_{jk}(\lambda)$ respectively.

Theorem 1 *Let $Q(\lambda)$ denote the resolution of the identity corresponding to the self-adjoint operator M . Then, the components \mathfrak{S}_{jk}^* and \mathfrak{A}_{jk}^* , $j, k = 1, \dots, d$, of the symmetric \mathfrak{S}^* and antisymmetric \mathfrak{A}^* parts of the effective diffusivity matrix \mathfrak{D}^* have the following Stieltjes-Radon integral representations*

$$\mathfrak{S}_{jk}^* = \varepsilon \left(\delta_{jk} + \int_{-\infty}^{\infty} \frac{d\text{Re } \mu_{jk}(\lambda)}{\varepsilon^2 + \lambda^2} \right), \quad \mathfrak{A}_{jk}^* = \int_{-\infty}^{\infty} \frac{\lambda d\text{Im } \mu_{jk}(\lambda)}{\varepsilon^2 + \lambda^2}. \quad (19)$$

For $j \neq k$, $\operatorname{Re} \mu_{jk}$ and $\operatorname{Im} \mu_{jk}$ are signed measures [20]. For $j = k$, $\operatorname{Re} \mu_{kk} = \mu_{kk}$ is a positive measure [20], which demonstrates that the effective transport of the scalar density ϕ is enhanced by the presence of an incompressible fluid velocity field \mathbf{u} , above the bare diffusive value ε

$$\mathfrak{S}_{kk}^* = \varepsilon \left(1 + \int_{-\infty}^{\infty} \frac{d\mu_{kk}(\lambda)}{\varepsilon^2 + \lambda^2} \right) \geq \varepsilon. \quad (20)$$

The mass μ_{jk}^0 of the measure μ_{jk} is real-valued and satisfies

$$\mu_{jk}^0 = \langle [(-\Delta)^{-1} u_j] u_k \rangle, \quad |\mu_{jk}^0| \leq \|\Delta^{-1} u_j\| \|u_k\| < \infty. \quad (21)$$

Proof of Theorem 1. We first provide integral representations for the bilinear functional formulas in equation (13) for \mathfrak{S}_{jk}^* and \mathfrak{A}_{jk}^* . Since we have already established the operator M is self-adjoint, we only need to identify the appropriate functions $f(\lambda)$ and $h(\lambda)$ as well as the Hilbert space members $\xi, \zeta \in \mathcal{H}^{1,2}$ in (17). Using $A = iM$, comparison of the functionals in equations (13) and (17) identifies $f(\lambda) = h(\lambda) = (\varepsilon + i\lambda)^{-1}$ for the first formula in (13), while $f(\lambda) = i\lambda(\varepsilon + i\lambda)^{-1}$ and $h(\lambda) = (\varepsilon + i\lambda)^{-1}$ for the second formula, with $\xi = g_j$ and $\zeta = g_k$ for both of these formulas.

Now we just need to verify $f, h \in L^2(\mu_{kk})$ for all $k = 1, \dots, d$ and $0 < \varepsilon < \infty$. From equation (18), the mass μ_{jk}^0 of the measure μ_{jk} is given by $\mu_{jk}^0 = \langle g_j, g_k \rangle_{1,2} = \langle \nabla \Delta^{-1} u_j \cdot \nabla \Delta^{-1} u_k \rangle$. Integration by parts and the Cauchy-Schwartz inequality [20] then yield equation (21). In particular $|\mu_{jk}^0| \leq \|\Delta^{-1}\| \|u_k\|^2 < \infty$, as Δ^{-1} has bounded operator norm $\|\Delta^{-1}\|$ on $L^2(\mathcal{V})$ [56]. Consequently, since $0 < (\varepsilon^2 + \lambda^2)^{-1} \leq 1/\varepsilon^2 < \infty$ and $0 < \lambda^2(\varepsilon^2 + \lambda^2)^{-1} < 1$ for all $0 < \varepsilon < \infty$, it is clear that $f, h \in L^2(\mu_{kk})$. Consequently, the spectral theorem in (17) implies that the functional formulas for \mathfrak{S}_{jk}^* and \mathfrak{A}_{jk}^* in equation (13) have the following Stieltjes integral representations

$$\mathfrak{S}_{jk}^* = \varepsilon \left(\delta_{jk} + \int_{-\infty}^{\infty} \frac{d\mu_{jk}(\lambda)}{\varepsilon^2 + \lambda^2} \right), \quad \mathfrak{A}_{jk}^* = - \int_{-\infty}^{\infty} \frac{i\lambda d\mu_{jk}(\lambda)}{\varepsilon^2 + \lambda^2}, \quad (22)$$

which involve the *complex measure* μ_{jk} .

We now show how the integrals for \mathfrak{S}_{jk}^* and \mathfrak{A}_{jk}^* in (22) can be represented in terms of the *signed measures* $\operatorname{Re} \mu_{jk}$ and $\operatorname{Im} \mu_{jk}$. Since ε, χ_k, u_k , and g_k in (13) are *real-valued*, we have from (12) the following symmetry conditions

$$\begin{aligned} \langle (\varepsilon I + A)^{-1} g_j, (\varepsilon I + A)^{-1} g_k \rangle_{1,2} &= \langle (\varepsilon I + A)^{-1} g_k, (\varepsilon I + A)^{-1} g_j \rangle_{1,2} \\ \langle A (\varepsilon I + A)^{-1} g_j, (\varepsilon I + A)^{-1} g_k \rangle_{1,2} &= \langle (\varepsilon I + A)^{-1} g_k, A (\varepsilon I + A)^{-1} g_j \rangle_{1,2}. \end{aligned} \quad (23)$$

These symmetries, the sesquilinearity of the \mathcal{H} -inner-product, the linearity [58] of the Stieltjes integrals in equation (22) with respect to the function $\mu_{jk}(\lambda)$, and the two identities $\operatorname{Re} \mu_{jk}(\lambda) = (\mu_{jk}(\lambda) + \bar{\mu}_{jk}(\lambda))/2$ and $\operatorname{Im} \mu_{jk}(\lambda) = (\mu_{jk}(\lambda) - \bar{\mu}_{jk}(\lambda))/(2i)$ yield equation (19). This concludes our proof of Theorem 1 \square .

Theorem 2 *Let Σ denote the spectrum of the operator M , denote $\lambda_+ = \sup_{\lambda \in \Sigma} |\lambda|$, and assume $0 < \varepsilon < \infty$. Then, the diagonal components $\mathfrak{S}_{kk}^* = \mathfrak{D}_{kk}^*$ of the effective diffusivity matrix satisfy the following, rigorous upper [4] and lower bounds*

$$\varepsilon [1 + \mu_{kk}^0 / (\varepsilon^2 + \lambda_+^2)] \leq \mathfrak{S}_{kk}^* \leq \varepsilon [1 + \mu_{kk}^0 / \varepsilon^2]. \quad (24)$$

For $j \neq k$, let $\operatorname{Re} \mu_{jk} = \operatorname{Re} \mu_{jk}^+ - \operatorname{Re} \mu_{jk}^-$ and $\operatorname{Im} \mu_{jk} = \operatorname{Im} \mu_{jk}^+ - \operatorname{Im} \mu_{jk}^-$ denote the Jordan decomposition of the signed measures $\operatorname{Re} \mu_{jk}$ and $\operatorname{Im} \mu_{jk}$, respectively, and denote the total variation of these measures by $|\operatorname{Re} \mu|_{jk} = \operatorname{Re} \mu_{jk}^+ + \operatorname{Re} \mu_{jk}^-$ and $|\operatorname{Im} \mu|_{jk} = \operatorname{Im} \mu_{jk}^+ + \operatorname{Im} \mu_{jk}^-$, respectively. Finally, denote the masses of the measures $\operatorname{Re} \mu_{jk}^+$, $\operatorname{Re} \mu_{jk}^-$, and $|\operatorname{Im} \mu|_{jk}$ by $[\operatorname{Re} \mu_{jk}^+]^0$, $[\operatorname{Re} \mu_{jk}^-]^0$, and $|\operatorname{Im} \mu|_{jk}^0$, respectively. Then, the off-diagonal components \mathfrak{S}_{jk}^* and \mathfrak{A}_{jk}^* , $j \neq k$, satisfy the following, rigorous upper and lower bounds

$$\varepsilon \frac{[\operatorname{Re} \mu_{jk}^+]^0}{\varepsilon^2 + \lambda_+^2} - \frac{[\operatorname{Re} \mu_{jk}^-]^0}{\varepsilon} \leq \mathfrak{S}_{jk}^* \leq \frac{[\operatorname{Re} \mu_{jk}^+]^0}{\varepsilon} - \varepsilon \frac{[\operatorname{Re} \mu_{jk}^-]^0}{\varepsilon^2 + \lambda_+^2}, \quad j \neq k, \quad (25)$$

$$-\frac{\lambda_+ |\operatorname{Im} \mu|_{jk}^0}{\varepsilon^2} \leq \mathfrak{A}_{jk}^* \leq \frac{\lambda_+ |\operatorname{Im} \mu|_{jk}^0}{\varepsilon^2}, \quad j \neq k. \quad (26)$$

Proof of Theorem 2. Assume that $0 < \varepsilon < \infty$. From equation (15), the spectrum Σ of the *compact* [9, 10, 33] operator $M = -iA$ is a bounded subset of \mathbb{R} . The spectrum is discrete [56] away from the spectral origin $\lambda = 0$ and comes in \pm pairs [48] with an accumulation point at $\lambda = 0$ [56]. Denote $\lambda_+ = \sup_{\lambda \in \Sigma} |\lambda|$ and note that $\inf_{\lambda \in \Sigma} \lambda^2 = 0$. The inequalities $1/(\varepsilon^2 + \lambda_+^2) \leq 1/(\varepsilon^2 + \lambda^2) \leq 1/\varepsilon^2$, hold for all $\lambda \in \Sigma$. Consequently, since μ_{kk} is a positive measure with finite mass μ_{kk}^0 , the inequalities in (24) hold [20]. It may happen that $\mu_{kk}^0 = 0$, hence $\mathfrak{S}_{kk}^* = \varepsilon$, e.g., shear flow orthogonal to the k th direction [4, 17].

When $j \neq k$, $\operatorname{Re} \mu_{jk}$ is a signed measure. By the Jordan decomposition of $\operatorname{Re} \mu_{jk}$, there are unique, *positive* measures $\operatorname{Re} \mu_{jk}^+$ and $\operatorname{Re} \mu_{jk}^-$ such that $\operatorname{Re} \mu_{jk} = \operatorname{Re} \mu_{jk}^+ - \operatorname{Re} \mu_{jk}^-$. Moreover, associated with the signed measure $\operatorname{Re} \mu_{jk}$ is its *total variation* $|\operatorname{Re} \mu|_{jk}$ [20]

$$\operatorname{Re} \mu_{jk} = \operatorname{Re} \mu_{jk}^+ - \operatorname{Re} \mu_{jk}^-, \quad |\operatorname{Re} \mu|_{jk} = \operatorname{Re} \mu_{jk}^+ + \operatorname{Re} \mu_{jk}^-. \quad (27)$$

From equation (21) the measures $\text{Re } \mu_{jk}^+$ and $\text{Re } \mu_{jk}^-$ have bounded mass, which we denote $[\text{Re } \mu_{jk}^+]^0$ and $[\text{Re } \mu_{jk}^-]^0$, respectively, thus the mass $|\text{Re } \mu|_{jk}^0$ of the measure $|\text{Re } \mu|_{jk}$ is also bounded. Since we have [20] that $|\mathfrak{S}_{jk}^*| \leq \int d|\text{Re } \mu|_{jk}(\lambda)/(\varepsilon^2 + \lambda^2)$, the upper bound in equation (24) with μ_{kk}^0 replaced by $|\text{Re } \mu|_{jk}^0$ holds for the positive quantity $|\mathfrak{S}_{jk}^*|$. These bounds for \mathfrak{S}_{jk}^* can be improved upon by separately considering the positive and negative contributions of the integral representation for \mathfrak{S}_{jk}^* , yielding equation (25). In a similar way, we obtain the bounds for \mathfrak{A}_{jk}^* in equation (26). This concludes our proof of Theorem 2 \square .

We conclude this section by noting that bounds on \mathfrak{S}_{kk}^* can also be obtained using variational methods [4, 17, 18] as well as Padé approximants [4, 6] of Stieltjes functions.

IV. DISCRETE SETTING: SOBOLEV SPACE OF SCALAR FIELDS

For our numerical computations of the effective diffusivity \mathfrak{D}^* in Section V, we consider a discrete approximation of the cell problem in equation (4) written as $(\varepsilon + iM)\chi_j = g_j$. Here $M = -iA$, $A = \Delta^{-1}[\mathbf{u} \cdot \nabla]$, and $g_j = -\Delta^{-1}u_j$, as defined in equations (11) and (12). In this section, we manipulate these formulas in order to develop a numerical algorithm which enables numerical computations of \mathfrak{D}^* by directly computing a discrete representation of the spectral measure μ_{jk} in equation (19), in terms of the eigenvalues and eigenvectors of a *generalized* eigenvalue problem. This is not a trivial extension of the spectral theory for the continuum setting discussed in Section III, as the matrix representation of the operator $(-\Delta)^{-1}[\mathbf{u} \cdot \nabla]$ is *not* Hermitian. The special structure of the generalized eigenvalue problem itself makes these matrix operators Hermitian only with respect to a discrete Sobolev-like inner-product analogous to the inner-product $\langle \cdot, \cdot \rangle_{1,2}$ introduced after equation (8). Moreover, the eigenvector orthogonality is only with respect to this inner-product.

Towards this goal, we begin by noting that since $\mathbf{u}(\mathbf{x})$ is incompressible, $\nabla \cdot \mathbf{u} = 0$, there is a real (non-dimensional) *antisymmetric* matrix $\mathsf{H}(\mathbf{x})$ [3, 4] such that

$$\mathbf{u} = \nabla \cdot \mathsf{H}, \quad \mathsf{H}^T = -\mathsf{H}, \tag{28}$$

where H^T denotes transposition of the matrix H . Due to the anti-symmetry of the matrix H in equation (28) and the symmetry of the Hessian operator $\nabla \nabla$ when acting on a sufficiently smooth space of functions, we have $\mathsf{H} : \nabla \nabla \varphi = 0$ for all such smooth functions φ , where $:$ denotes matrix contraction. Consequently, $\nabla \cdot [\mathsf{H} \nabla \varphi] = [\nabla \cdot \mathsf{H}] \cdot \nabla \varphi + \mathsf{H} : \nabla \nabla \varphi = [\nabla \cdot \mathsf{H}] \cdot \nabla \varphi$,

or

$$\nabla \cdot [\mathbf{H} \nabla] = [\nabla \cdot \mathbf{H}] \cdot \nabla, \quad (29)$$

as operators acting on such functions. With (29) we can write the operator $M = \imath(-\Delta)^{-1}[\mathbf{u} \cdot \nabla]$ as $M = \imath(-\Delta)^{-1}\nabla \cdot [\mathbf{H} \nabla]$.

We now discuss our discrete formulation of the effective parameter problem, which leads to Stieltjes integral representations for the symmetric \mathfrak{S}^* and antisymmetric \mathfrak{A}^* components of the effective diffusivity matrix \mathfrak{D}^* , involving a discrete spectral measure. For notational brevity, assume the period cell \mathcal{V} is square. In the discrete setting [42], \mathcal{V} is represented by a square grid of size L , which is bijectively mapped to a vector with L^d components. The functions $u_j(\mathbf{x})$ and $\chi_j(\mathbf{x})$ are mapped to vectors \mathbf{u}_j and $\boldsymbol{\chi}_j$ with L^d components, respectively, and the matrix $\mathbf{H}(\mathbf{x})$ is mapped to a square banded antisymmetric matrix of size $N = L^d d$ (see Section V A for details). For simplicity, we will not make a notational distinction for \mathbf{H} between the discrete and continuum settings, as the context will be clear.

The differential operator ∇ is represented by a finite difference matrix ∇ [14, 42], where $\nabla^T = (\nabla_1^T, \dots, \nabla_d^T)$ and ∇_j , $j = 1, \dots, d$, are also finite difference matrices. Moreover, the divergence operator $\nabla \cdot$ is given by $-\nabla^T$ and the matrix representation of the negative Laplacian $-\Delta$ is given by $\nabla^T \nabla$. Consequently, we may write the discrete, matrix representation \mathbf{M} of the self-adjoint operator $M = \imath(-\Delta)^{-1}\nabla \cdot [\mathbf{H} \nabla]$ as $\mathbf{M} = (\nabla^T \nabla)^{-1}[-\imath \nabla^T \mathbf{H} \nabla]$. This composition of the Hermitian matrix $-\imath \nabla^T \mathbf{H} \nabla$ and the real-symmetric matrix $(\nabla^T \nabla)^{-1}$ is neither real-symmetric nor Hermitian symmetric. From equation (C1) we see that the symmetry properties of the integro-differential operator M depend intimately on the inner-product $\langle f, h \rangle_{1,2} = \langle \nabla f \cdot \nabla h \rangle$ of the underlying Sobolev space $\mathcal{H}^{1,2}$ defined in equation (8). Therefore, we anticipate the properties of this inner-product must be incorporated into the discrete formulation of integral representations for \mathfrak{D}^* .

We now provide a matrix formulation of the effective parameter problem introduced in Section III, which involves a *generalized eigenvalue problem* that has the Sobolev-type inner-product as a central feature. In particular, this formulation retains the key properties of the weak form of the eigenvalue problem $\langle M\varphi_n, \varphi_n \rangle_{1,2} = \lambda_n$. Namely, the operator M is self-adjoint *with respect to the inner-product* $\langle \cdot, \cdot \rangle_{1,2}$, its eigenfunctions $\varphi_n \in \mathcal{H}^{1,2}$ are orthonormal $\langle \varphi_n, \varphi_m \rangle_{1,2} = \delta_{nm}$, $n, m = 1, 2, 3, \dots$, with respect to the inner-product $\langle \cdot, \cdot \rangle_{1,2}$, and the spectrum Σ of M is real valued, $\Sigma \subset \mathbb{R}$. Towards this goal, consider the eigenvalue

problem $M\varphi_n = \lambda_n\varphi_n$ in the following “strong” form,

$$\imath \nabla \cdot [\mathsf{H} \nabla \varphi_n] = \lambda_n (-\Delta) \varphi_n. \quad (30)$$

Using a discrete version of equation (30), we will establish the integral representations in (19) for discrete versions of the functionals $\mathfrak{S}_{jk}^* = \varepsilon(\delta_{jk} + \langle \chi_j, \chi_k \rangle_{1,2})$ and $\mathfrak{A}_{jk}^* = \langle \imath M \chi_j, \chi_k \rangle_{1,2}$ in (11), involving a discrete spectral measure.

By our discussion in this section, the matrix representation of the eigenvalue problem in (30) is

$$\mathsf{B} \mathbf{z}_n = \lambda_n \mathsf{C} \mathbf{z}_n, \quad \mathsf{B} = -\imath \nabla^T \mathsf{H} \nabla, \quad \mathsf{C} = \nabla^T \nabla. \quad (31)$$

The first formula in equation (31) is a *generalized eigenvalue problem* [47] associated with the pencil $\mathsf{B} - \lambda \mathsf{C}$, where B and C are Hermitian and real-symmetric matrices, respectively, of size $K = L^d$. The λ_n and \mathbf{z}_n , $n = 1, \dots, K$, are known as generalized eigenvalues and eigenvectors, respectively. The matrix $\mathsf{C} = \nabla^T \nabla$ is clearly positive semi-definite. In this section, we will assume that C is positive definite, hence invertible. We will discuss the case where C is positive semi-definite in Appendix G, which is necessary for the setting where ∇ incorporates *periodic* boundary conditions — needed for our study of advection enhanced diffusion by a spatially periodic fluid velocity field \mathbf{u} .

Since B and C are Hermitian and real-symmetric, respectively, and C is positive definite, the generalized eigenvalue problem in (31) has properties which are similar to the properties of the standard symmetric eigenvalue problem [47]. In particular, the generalized eigenvalues λ_n are all real, the generalized eigenvectors \mathbf{z}_n form a basis for \mathbb{C}^K , and the \mathbf{z}_n are orthonormal in the following sense $\mathbf{z}_n^\dagger \mathsf{C} \mathbf{z}_m = \delta_{nm}$, $n, m = 1, \dots, K$ [47]. Since $\mathsf{C} = \nabla^T \nabla$ is real-valued, this is equivalent to the Sobolev-type orthogonality condition

$$\nabla \mathbf{z}_n \cdot \nabla \mathbf{z}_m = \delta_{nm}. \quad (32)$$

In other words, the generalized eigenvectors \mathbf{z}_n are orthonormal with respect to the “discrete inner-product” $\langle \cdot, \cdot \rangle_{1,2}$ defined by $\langle \boldsymbol{\xi}, \boldsymbol{\zeta} \rangle_{1,2} = \langle \nabla \boldsymbol{\xi} \cdot \nabla \boldsymbol{\zeta} \rangle$, for $\boldsymbol{\xi}, \boldsymbol{\zeta} \in \mathbb{C}^K$ and $\langle \cdot \rangle$ denotes ensemble averaging. Denoting by \mathbf{Z} the matrix with columns consisting of the generalized eigenvectors \mathbf{z}_n , equation (32) is seen to be equivalent to $[\nabla \mathbf{Z}]^\dagger [\nabla \mathbf{Z}] = \mathbf{I}$, or $\mathbf{Z}^\dagger \mathsf{C} \mathbf{Z} = \mathbf{I}$. A key feature of the generalized eigenvalue problem is that the matrix \mathbf{Z} simultaneously diagonalizes B and C . Specifically, if Λ is the diagonal matrix whose elements on the main diagonal are the

generalized eigenvalues λ_n , then [47]

$$\mathbf{Z}^\dagger \mathbf{B} \mathbf{Z} = \Lambda, \quad \mathbf{Z}^\dagger \mathbf{C} \mathbf{Z} = \mathbf{I}. \quad (33)$$

We now derive the discrete version of equations (16)–(18) comprising the key results of the spectral theorem, for the generalized eigenvalue problem setting. These derivations will streamline and clarify our results for the current section, showing how the derived series representations of the symmetric \mathfrak{S}^* and antisymmetric \mathfrak{A}^* parts of the effective diffusivity matrix \mathfrak{D}^* can be written as the Stieltjes integrals in equation (19), involving a discrete spectral measure. This derivation will also clarify and streamline our results in the appendix, which lead to the numerical algorithm used in Section V for spectral computations of \mathfrak{D}^* for periodic fluid flows. The numerical algorithm used in Section V is analogous to the algorithm that we develop in the current section, which is elegant for the full-rank setting — revealing a great deal of structure with minimal effort. The matrix analysis of the rank-deficient setting developed in Appendix G is quite a bit more involved. Developing the full-rank setting in the current section first, makes the results of the rank-deficient setting more transparent and the final results more anticipated.

Since the \mathbf{z}_n , $n = 1, \dots, K$, form a basis for \mathbb{C}^K and satisfy the orthogonality relation in (32), for all $\boldsymbol{\xi} \in \mathbb{C}^K$ we have $\boldsymbol{\xi} = \sum_n (\nabla \mathbf{z}_n \cdot \nabla \boldsymbol{\xi}) \mathbf{z}_n = \sum_n (\mathbf{z}_n [\nabla \mathbf{z}_n]^\dagger \nabla) \boldsymbol{\xi}$, which implies

$$\sum_{n=1}^K \mathbf{Q}_n = \mathbf{I}, \quad \mathbf{Q}_n = \mathbf{z}_n [\nabla \mathbf{z}_n]^\dagger \nabla, \quad \mathbf{Q}_l \mathbf{Q}_m = \mathbf{Q}_l \delta_{lm}, \quad (34)$$

where the matrix operators \mathbf{Q}_n , $n = 1, \dots, K$, are self-adjoint with respect to the *discrete* inner-product $\langle \cdot, \cdot \rangle_{1,2}$ defined above, i.e., $\langle \mathbf{Q}_n \boldsymbol{\xi}, \boldsymbol{\zeta} \rangle_{1,2} = \langle \boldsymbol{\xi}, \mathbf{Q}_n \boldsymbol{\zeta} \rangle_{1,2}$ for all $\boldsymbol{\xi}, \boldsymbol{\zeta} \in \mathbb{C}^K$. From $\mathbf{B} \mathbf{z}_n = \lambda_n \mathbf{C} \mathbf{z}_n$ and equation (34) we have that $\mathbf{B} \mathbf{Q}_n = \lambda_n \mathbf{C} \mathbf{Q}_n$ which is equivalent to $\mathbf{C}^{-1} \mathbf{B} \mathbf{Q}_n = \lambda_n \mathbf{Q}_n$, since the matrix \mathbf{C} is invertible. This formula and (34) then imply that the matrix $\mathbf{C}^{-1} \mathbf{B}$ has the spectral decomposition $\mathbf{C}^{-1} \mathbf{B} = \sum_n \lambda_n \mathbf{Q}_n$. By the mutual orthogonality of the projection matrices \mathbf{Q}_n and by induction, we have that $[\mathbf{C}^{-1} \mathbf{B}]^m = \sum_n \lambda_n^m \mathbf{Q}_n$ for all $m \in \mathbb{N}$. This, in turn, implies that $f(\mathbf{C}^{-1} \mathbf{B}) = \sum_n f(\lambda_n) \mathbf{Q}_n$ for any polynomial $f : \mathbb{R} \mapsto \mathbb{C}$.

From the mutual orthogonality of the projection matrices \mathbf{Q}_n and their symmetry with respect to the discrete inner-product $\langle \cdot, \cdot \rangle_{1,2}$ it follows that, for all $\boldsymbol{\xi}, \boldsymbol{\zeta} \in \mathbb{C}^K$ and all complex-valued polynomials $f(\lambda)$ and $h(\lambda)$, the bilinear functional $\langle f(\mathbf{C}^{-1} \mathbf{B}) \boldsymbol{\xi}, h(\mathbf{C}^{-1} \mathbf{B}) \boldsymbol{\zeta} \rangle_{1,2}$ has the integral representation in (17), with M substituted by $\mathbf{C}^{-1} \mathbf{B}$ and other appropriate notational changes. Moreover, the complex-valued function $\mu_{\boldsymbol{\xi}\boldsymbol{\zeta}}(\lambda) = \langle Q(\lambda) \boldsymbol{\xi}, \boldsymbol{\zeta} \rangle_{1,2}$ in (17) is now given

by $\mu_{\xi\zeta}(\lambda) = \langle Q(\lambda)\xi, \zeta \rangle_{1,2}$, where the associated matrix representation $Q(\lambda)$ of the projection operator $Q(\lambda)$ and the discrete spectral measure $d\mu_{\xi\zeta}(\lambda)$ are given by

$$Q(\lambda) = \sum_{n: \lambda_n \leq \lambda} \theta(\lambda - \lambda_n) Q_n, \quad d\mu_{\xi\zeta}(\lambda) = \sum_{n: \lambda_n \leq \lambda} \langle \delta_{\lambda_n}(d\lambda) [\nabla Q_n \xi \cdot \nabla \zeta] \rangle. \quad (35)$$

Here, $\theta(\lambda)$ is the Heaviside function, satisfying $\theta(\lambda) = 0$ for $\lambda < 0$ and $\theta(\lambda) = 1$ for $\lambda \geq 0$, and $\delta_{\lambda_n}(d\lambda) = d\theta(\lambda - \lambda_n)$ is the δ -measure centered at λ_n . From equation (34) and well known properties of $\theta(\lambda)$, we have that $Q(\lambda)$ satisfies equation (16). From equation (34) and well known properties of the δ -measure, the mass $\mu_{\xi\zeta}^0$ of the spectral measure in (35) satisfies equation (18) with appropriate notational changes. We are now ready to present the main result of this section.

Theorem 3 Consider the generalized eigenvalue problem $Bz_n = \lambda_n Cz_n$ in (31). Let Z be the matrix with columns consisting of the eigenvectors z_n and Λ be the diagonal matrix with eigenvalues λ_n on the diagonal, which satisfy equation (33). The discrete, matrix representations of the bilinear functional formulas for \mathfrak{S}_{jk}^* and \mathfrak{A}_{jk}^* in equation (11) are given by

$$\mathfrak{S}_{jk}^* = \varepsilon(\delta_{jk} + \langle \nabla \chi_j \cdot \nabla \chi_k \rangle), \quad \mathfrak{A}_{jk}^* = \langle \nabla C^{-1}[iB]\chi_j \cdot \nabla \chi_k \rangle. \quad (36)$$

Also, the discrete representation of the resolvent formula for χ_j in equation (12) is given by

$$\chi_j = Z(\varepsilon I + i\Lambda)^{-1} Z^\dagger \mathbf{u}_j. \quad (37)$$

The discrete representations of the bilinear functional formulas for \mathfrak{S}_{jk}^* and \mathfrak{A}_{jk}^* in (13) are given by

$$\begin{aligned} \mathfrak{S}_{jk}^* &= \varepsilon(\delta_{jk} + \langle (\varepsilon I + i\Lambda)^{-1} Z^\dagger \mathbf{u}_j \cdot (\varepsilon I + i\Lambda)^{-1} Z^\dagger \mathbf{u}_k \rangle), \\ \mathfrak{A}_{jk}^* &= \langle i\Lambda(\varepsilon I + i\Lambda)^{-1} Z^\dagger \mathbf{u}_j \cdot (\varepsilon I + i\Lambda)^{-1} Z^\dagger \mathbf{u}_k \rangle. \end{aligned} \quad (38)$$

Consequently, from the discrete analogue of equation (23) and the formulas for \mathfrak{S}_{jk}^* and \mathfrak{A}_{jk}^* in (38), we have the following series representations

$$\mathfrak{S}_{jk}^*/\varepsilon - \delta_{jk} = \sum_{n=1}^K \frac{\operatorname{Re}[(\overline{z_n^\dagger \mathbf{u}_j})(z_n^\dagger \mathbf{u}_k)]}{\varepsilon^2 + \lambda_n^2}, \quad \mathfrak{A}_{jk}^* = \sum_{n=1}^K \frac{\lambda_n \operatorname{Im}[(\overline{z_n^\dagger \mathbf{u}_j})(z_n^\dagger \mathbf{u}_k)]}{\varepsilon^2 + \lambda_n^2}. \quad (39)$$

Finally, defining $\mathfrak{g}_j = (\nabla^T \nabla)^{-1} \mathbf{u}_j$ and recalling the projection matrix Q_n in (34), we have

$$\overline{(z_n^\dagger \mathbf{u}_j)}(z_n^\dagger \mathbf{u}_k) = \nabla Q_n \mathfrak{g}_j \cdot \nabla \mathfrak{g}_k. \quad (40)$$

It follows from equations (39) and (40) that the series representations for \mathfrak{S}_{jk}^* and \mathfrak{A}_{jk}^* in (39) have the Stieltjes integral representations in equation (19), involving the discrete spectral measure μ_{jk} in (35) with $\xi = \mathfrak{g}_j$ and $\zeta = \mathfrak{g}_k$.

Proof of Theorem 3. From the matrix representation $A = (\nabla^T \nabla)^{-1}(\nabla^T H \nabla)$ of the operator $A = \Delta^{-1} \nabla \cdot [H \nabla]$ and equation (31), the matrix representation of the functional formulas $\mathfrak{S}_{jk}^* = \varepsilon(\delta_{jk} + \langle \chi_j, \chi_k \rangle_{1,2})$ and $\mathfrak{A}_{jk}^* = \langle A\chi_j, \chi_k \rangle_{1,2}$ in equation (11) are given by (36). Moreover, the matrix representation of the cell problem $\varepsilon\Delta\chi_j + \nabla \cdot [H \nabla]\chi_j = -u_j$ in (4) is given by

$$(\varepsilon C + iB)\chi_j = u_j. \quad (41)$$

The matrix Z is invertible, as the generalized eigenvectors z_n form a basis for \mathbb{C}^K . Consequently, by equation (33) we have that $B = Z^{-\dagger}\Lambda Z^{-1}$, $C = Z^{-\dagger}Z^{-1}$. It now follows from equation (41) that $Z^{-\dagger}(\varepsilon I + i\Lambda)Z^{-1}\chi_j = u_j$, which implies the resolvent formula for χ_j in equation (37).

Substituting the resolvent formula for χ_j in (37) into equation (36) yields equation (38), where we have used that $[\nabla Z]^\dagger = [\nabla Z]^{-1}$. The quadratic form $Z^\dagger u_j \cdot Z^\dagger u_k$ arising in (38) can be written in terms of the projection matrices Q_n defined in (34) as follows

$$Z^\dagger u_j \cdot Z^\dagger u_k = \sum_{n=1}^K \overline{(z_n^\dagger u_j)(z_n^\dagger u_k)} = \sum_{n=1}^K z_n z_n^\dagger u_j \cdot u_k. \quad (42)$$

We now demonstrate that $z_n z_n^\dagger u_j \cdot u_k = \nabla Q_n g_j \cdot \nabla g_k$, where $g_j = (\nabla^T \nabla)^{-1} u_j$,

$$z_n z_n^\dagger u_j \cdot u_k = z_n z_n^\dagger [\nabla^T \nabla] g_j \cdot [\nabla^T \nabla] g_k = [\nabla z_n] [\nabla z_n]^\dagger \nabla g_j \cdot \nabla g_k = \nabla Q_n g_j \cdot \nabla g_k, \quad (43)$$

which establishes equation (40). This concludes our proof of Theorem 3 \square .

In Section V we use a generalization of equation (39) to compute Stieltjes integral representations for the symmetric \mathfrak{S}^* and antisymmetric \mathfrak{A}^* parts of the effective diffusivity matrix \mathfrak{D}^* for some model, periodic fluid velocity fields. This generalization, discussed in Theorem 10 below, is a direct analogue of equation (39) and holds for the setting where the matrix gradient ∇ with periodic boundary conditions is rank-deficient, so the negative matrix Laplacian $\nabla^T \nabla$ is *non-invertible*.

We conclude this section with a discussion that helps reduce the amount of memory required to store the eigenvalues and spectral weights comprising the discrete spectral measure, which

is useful when computing a large number of statistical realizations associated with randomly perturbed periodic flows. From the formula for $\mu_{\xi\zeta}(\lambda)$ above equation (35), the fact that the matrix ∇ and vectors \mathbf{g}_k are real-valued, and the two identities $\text{Re } \mu_{jk}(\lambda) = (\mu_{jk}(\lambda) + \bar{\mu}_{jk}(\lambda))/2$ and $\text{Im } \mu_{jk}(\lambda) = (\mu_{jk}(\lambda) - \bar{\mu}_{jk}(\lambda))/(2i)$, we have

$$\begin{aligned}\text{Re } \mu_{jk}(\lambda) &= \frac{1}{2} \sum_{n: \lambda_n \leq \lambda} \langle \theta(\lambda - \lambda_n) [\nabla(Q_n + \bar{Q}_n) \mathbf{g}_j \cdot \nabla \mathbf{g}_k] \rangle \\ \text{Im } \mu_{jk}(\lambda) &= \frac{1}{2i} \sum_{n: \lambda_n \leq \lambda} \langle \theta(\lambda - \lambda_n) [\nabla(Q_n - \bar{Q}_n) \mathbf{g}_j \cdot \nabla \mathbf{g}_k] \rangle.\end{aligned}\quad (44)$$

with $[\nabla(Q_n + \bar{Q}_n) \mathbf{g}_j \cdot \nabla \mathbf{g}_k] = 2\text{Re}[\nabla Q_n \mathbf{g}_j \cdot \nabla \mathbf{g}_k]$ and $[\nabla(Q_n - \bar{Q}_n) \mathbf{g}_j \cdot \nabla \mathbf{g}_k] = 2i\text{Im}[\nabla Q_n \mathbf{g}_j \cdot \nabla \mathbf{g}_k]$.

Consider the generalized eigenvalue problem in equation (31) written as $[iB]\mathbf{z}_n = i\lambda_n C\mathbf{z}_n$, with $B = -i\nabla^T H \nabla$ and $C = \nabla^T \nabla$. Since the matrices iB and C are real-valued we have $[iB]\bar{\mathbf{z}}_n = -i\lambda_n C\bar{\mathbf{z}}_n$. Consequently, the (generalized) eigenvectors \mathbf{z}_n come in complex conjugate pairs and the λ_n come in \pm pairs. Therefore, if the size K of these matrices is even, then we may re-number the index set \mathcal{I}_K as $\mathcal{I}_K = \{-K/2, \dots, -1, 1, \dots, K/2\}$ such that $\lambda_{-n} = -\lambda_n$ and $\mathbf{z}_{-n} = \bar{\mathbf{z}}_n$. If K is odd then $\lambda_0 = 0$ is also an eigenvalue with a *real-valued* eigenvector \mathbf{z}_0 . Consequently, the representations of the measures $\text{Re } \mu_{jk}$ and $\text{Im } \mu_{jk}$, following from the functions in equation (44), can be simplified [48] to depend only on the restricted index set $\{n \geq 0 : \lambda_n \leq \lambda\}$. This is clear from equations (19) and (44), since for $n \geq 0$ we have $\lambda_{-n}^2 = (-\lambda_n)^2 = \lambda_n^2$ and $\mathbf{z}_{-n} = \bar{\mathbf{z}}_n$, thus $Q_{-n} = \bar{Q}_n$. It follows that

$$\begin{aligned}\text{Re}[\nabla Q_n \mathbf{g}_j \cdot \nabla \mathbf{g}_k] + \text{Re}[\nabla Q_{-n} \mathbf{g}_j \cdot \nabla \mathbf{g}_k] &= 2\text{Re}[\nabla Q_n \mathbf{g}_j \cdot \nabla \mathbf{g}_k] \\ \lambda_n \text{Im}[\nabla Q_n \mathbf{g}_j \cdot \nabla \mathbf{g}_k] + \lambda_{-n} \text{Im}[\nabla Q_{-n} \mathbf{g}_j \cdot \nabla \mathbf{g}_k] &= 2\lambda_n \text{Im}[\nabla Q_n \mathbf{g}_j \cdot \nabla \mathbf{g}_k],\end{aligned}\quad (45)$$

with $\lambda_0 \text{Im}[Q_0 \mathbf{g}_j \cdot \mathbf{g}_k] \equiv 0$. For numerical computations of statistical properties of advection enhanced diffusion by randomly perturbed periodic flows, a useful consequence of this is only *half* of the eigenvalues and spectral weights need to be held in memory, as the other half are redundant, which saves memory consumption.

V. SPECTRAL COMPUTATIONS OF THE EFFECTIVE DIFFUSIVITY MATRIX

In Section IV, we developed a mathematical framework that provides discrete Stieltjes integral representations for the symmetric \mathfrak{S}^* and antisymmetric \mathfrak{A}^* parts of the effective

diffusivity matrix \mathfrak{D}^* . These discrete integral representations can be written as the series shown in equation (39) or the integrals shown in (19), involving the discrete spectral measure in (35) with the appropriate notational changes described in Theorem 3. This framework assumes that the matrix gradient ∇ has Dirichlet boundary conditions, for example, so the matrix is *full-rank* and the negative matrix Laplacian $\nabla^T \nabla$ is invertible. However, for our studies of advection enhanced diffusion by spatially periodic fluid velocity fields, we need to use a matrix gradient ∇ with periodic boundary conditions and this matrix is *rank-deficient*. In order to streamline our presentation leading to the numerical results of the current section, in Appendix G we extend the discrete mathematical framework developed Section IV to the rank-deficient setting. This analysis, in the proof of Theorem 10 below, shows the discrete Stieltjes integral representations for \mathfrak{S}^* and \mathfrak{A}^* are given by direct analogues of the formulas in equation (39).

In this section, we use these direct analogues of the formulas in equation (39) to compute \mathfrak{D}^* for various model periodic flows and randomly perturbed periodic flows. As a benchmark test, we compute the spectral measure and \mathfrak{D}^* for a shear flow, which are known in closed form [4], and a cell flow with closed streamlines, for which it is known [17, 18] that $\mathfrak{D}^* \sim \varepsilon^{1/2}$ for $\varepsilon \ll 1$. Our numerical results are in good agreement with the theoretical results. We also consider a fluid velocity field that has a free parameter. As the parameter varies, the flow transitions from cell flow with closed streamlines to shear flow in the diagonal x - y direction. This gives rise to transitional behavior in the spectral measure, which governs transitional behavior in the effective diffusivity matrix \mathfrak{D}^* . For the sake of brevity, we will focus our attention on the ε -behavior of the components \mathfrak{S}_{jk}^* , $j, k = 1, \dots, d$, of \mathfrak{S}^* . Also, for computational simplicity, we have restricted our computations to dimension $d = 2$.

A. Numerical Methods

By equation (28), the time-independent fluid velocity field $\mathbf{u} = \mathbf{u}(\mathbf{x})$ is given in terms of an antisymmetric matrix $\mathbf{H} = \mathbf{H}(\mathbf{x})$, $\mathbf{u} = \nabla \cdot \mathbf{H}$. For dimension $d = 2$, the matrix \mathbf{H} is determined by a stream function $\Psi = \Psi(\mathbf{x})$,

$$\mathbf{H} = \begin{bmatrix} 0 & \Psi \\ -\Psi & 0 \end{bmatrix}, \quad (46)$$

yielding $\mathbf{u} = [-\partial_y \Psi, \partial_x \Psi]$, where ∂_x denotes partial differentiation in the variable x , for example. In this section we consider two flows with free parameters which transition from cell flow to shear flow as parameters vary. In particular, we consider BC-flow [11] and “cat’s eye” flow [17], which are defined by the following stream functions Ψ_{BC} and Ψ_{CE} , respectively,

$$\Psi_{BC}(\mathbf{x}) = B \sin x - C \sin y, \quad \Psi_{CE}(\mathbf{x}) = \sin x \sin y + \alpha \cos x \cos y, \quad (47)$$

where we have denoted $\mathbf{x} = (x, y)$. The corresponding fluid velocity fields are

$$\begin{aligned} \mathbf{u}_{BC}(\mathbf{x}) &= (C \cos y, B \cos x), \\ \mathbf{u}_{CE}(\mathbf{x}) &= (-\sin x \cos y + \alpha \cos x \sin y, \cos x \sin y - \alpha \sin x \cos y). \end{aligned} \quad (48)$$

The flow geometry of these fluid velocity fields transition from shear flow to cell flow structure as the system parameters $\alpha, B, C \in [0, 1]$ vary.

Streamlines of a 2D flow are level sets of the stream function Ψ , which define a family of curves that are instantaneously tangent to the fluid velocity field \mathbf{u} , since $\mathbf{u} = [-\partial_y \Psi, \partial_x \Psi]$ implies that $\mathbf{u} \cdot \nabla \Psi = 0$. In Fig. 1, we display streamlines of the flows in equation (47) for various parameter values. The streamlines for cat’s eye flow are symmetric about the line $y = x$, which follows from the symmetry of the stream function $\Psi_{CE}(x, y) = \Psi_{CE}(y, x)$. The stream function for BC-flow has a more complicated symmetry $\Psi(x, y; B, C) = -\Psi(y, x; C, B)$. This symmetry indicates that if the values of B and C are interchanged, $B \longleftrightarrow C$, then the original flow is recovered from a 90° rotation ($x \rightarrow y$, $y \rightarrow -x$) followed by a reflection about the x -axis ($y \rightarrow -y$). Consequently, flows elongated in the y -direction become flows elongated in the x -direction under the interchange $B \longleftrightarrow C$. Consistently, our numerical computations of μ_{jk} and \mathfrak{S}_{jk}^* , $j, k = 1, 2$, exhibit these symmetries. For BC-flow, these symmetries allow us to restrict our attention to the behavior of μ_{jk} and \mathfrak{S}_{jk}^* as only one parameter varies. Here we discuss our results for cat’s eye flow for various (deterministic) values of the parameter α as well as α uniformly distributed on the interval $[0, p]$ for various values of p . For the sake of brevity, we consider BC-shear flow in the x and y -directions only, which are obtained for parameter values $(B, C) = (0, 1)$ and $(B, C) = (1, 0)$, respectively, and do not display our results for the transitional behavior from one extreme to the other. The spectral measure and \mathfrak{D}^* were computed for BC-cell flow in [44].

In Section III, we gave an overview of the effective parameter problem for the setting of randomly perturbed, \mathcal{V} -periodic flows and introduced the Hilbert space \mathcal{H} in equation (7).

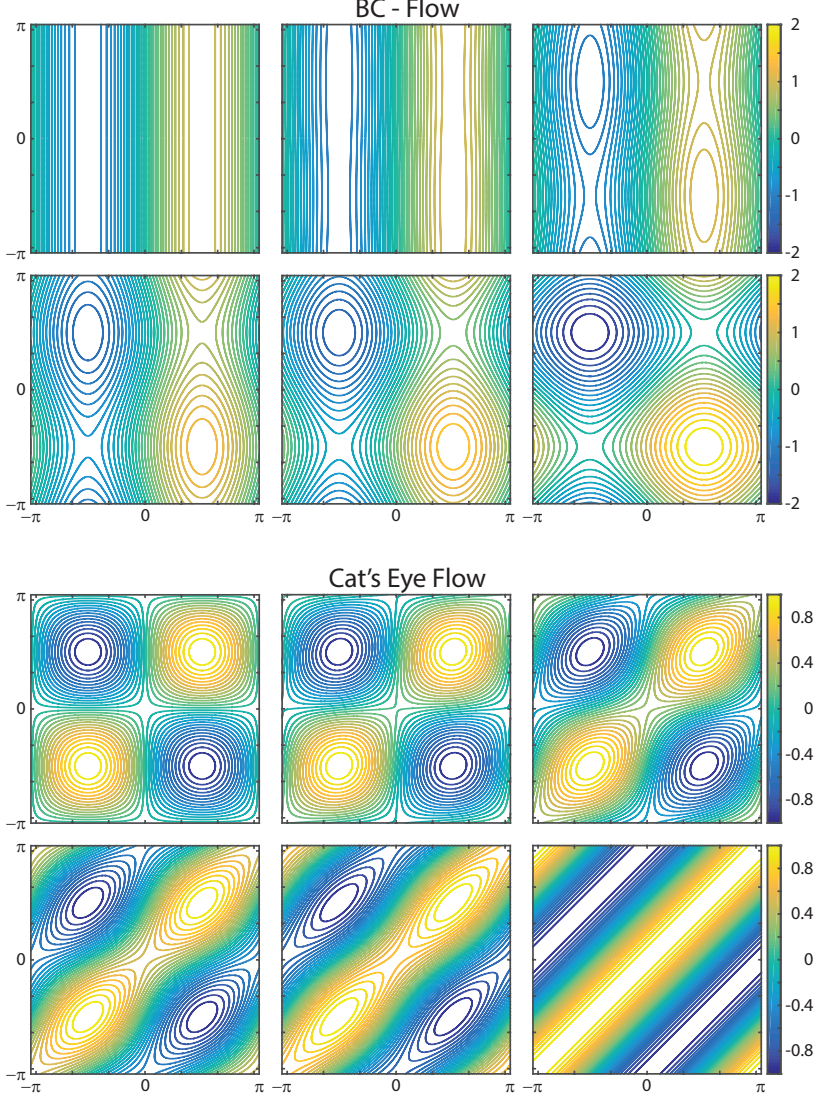


FIG. 1. Transitions in flow structure. The streamlines for BC-flow and cat's eye flow are displayed for various parameter values, transitioning from shear to cell flow structure. From left to right and top to bottom, the parameter values associated with BC-flow are $B = 1$ fixed and $C = 0, 0.01, 0.1, 0.3, 0.5$ and 1, while those for cat's eye flow are $\alpha = 0, 0.1, 0.3, 0.5, 0.7$, and 1.

Numerically, it is natural to set \mathcal{H} to be the space of randomly perturbed \mathcal{V} -periodic functions, $\mathcal{H} = L^2(\mathbf{m} \times P)$, where P is the probability measure associated with the random variable α [29]. In this case, by Fubini's theorem [20], $\langle \cdot \rangle$ can be considered to denote spatial averaging followed by statistical averaging.

We now discuss in more detail our discrete, matrix formulation of the effective parameter problem. To illustrate how to generalize these ideas to dimension d larger than $d = 2$, we

will maintain aspects of our general notation. In this discrete setting, the spatial region $\mathcal{V} = [0, 2\pi]^d$, for example, is replaced by a square lattice \mathcal{V}_L^d of size L containing L^d equally spaced points in \mathcal{V} . As discussed in Section IV, the differential operators ∇ and $\nabla \cdot$ are replaced by finite difference, matrix operators ∇ and $-\nabla^T$, respectively, with suitable boundary conditions. Periodic boundary conditions will be assumed throughout this section. Since these matrices operate on vectors, the d -dimensional lattice \mathcal{V}_L^d must be bijectively mapped to a one dimensional lattice \mathcal{V}_N of size $N = L^d d$. The specific structure of \mathcal{V}_N and ∇ depend on the bijective mapping Θ chosen. In our computations discussed in this section, we used the mapping Θ described in [42].

The spatially dependent d -dimensional vector field $\mathbf{v}(\mathbf{x}) = (v_1(\mathbf{x}), \dots, v_d(\mathbf{x}))$, say, is bijectively mapped by Θ to a discretized *constant* vector $(\mathbf{v}_1, \dots, \mathbf{v}_2)$ with N elements, where the vectors \mathbf{v}_i , $i = 1, \dots, d$, each have L^d elements and contain all of the spatial information about the $v_i(\mathbf{x})$ for $\mathbf{x} \in \mathcal{V}_L^d$. Similarly, the d -dimensional standard basis vector $\mathbf{e}_1 = (1, 0, \dots, 0)$ is mapped to the N -dimensional vector $(\mathbf{1}, \mathbf{0}, \dots, \mathbf{0})$, where $\mathbf{1}$ and $\mathbf{0}$ are vectors of ones and zeros with L^d elements, and similarly for the \mathbf{e}_j for $j = 2, \dots, d$. Therefore, the vectors $\hat{\mathbf{e}}_j$, $j = 1, \dots, d$, satisfying

$$\hat{\mathbf{e}}_j = \Theta(\mathbf{e}_j)/L^{d/2}, \quad \hat{\mathbf{e}}_j \cdot \hat{\mathbf{e}}_k = \delta_{jk}, \quad (49)$$

serve as “lattice standard basis vectors.” With this convention, the division by $L^{d/2}$ in (49) takes care of the uniform L -scaling in discrete approximations of spatial integrals; instead of the $(2\pi)^d$ normalized Lebesgue measure $d\mathbf{x}$ we have $\Delta\mathbf{x} = (2\pi/L)^d/(2\pi)^d$ when $\mathcal{V} = [0, 2\pi]^d$ and the spatial average $\langle \xi(\mathbf{x}) \zeta(\mathbf{x}) \rangle_{\mathcal{V}}$ becomes $\xi \cdot \zeta / L^d$. In a similar way, the 2×2 matrix $\mathbf{H}(\mathbf{x})$ in (46) becomes a $N \times N$ antisymmetric banded matrix, where the stream function $\Psi(\mathbf{x})$ is represented by a diagonal $L^d \times L^d$ matrix and the zero element 0 is represented by a matrix of zeros. As in previous sections, for notational simplicity, we will not make a notational distinction for the matrix \mathbf{H} between the continuum and discrete settings as the context will be clear.

In Theorem 10 of Appendix G below we extend our results developed in Theorem 1 of Section III to the setting where the matrix gradient ∇ has periodic boundary conditions and is rank-deficient. This is accomplished by considering the singular value decomposition (SVD) $\nabla = \mathbf{U}\Sigma\mathbf{V}^T$. Here, ∇ is of size $N \times K$, say, where $K = L^d$ and $N = Kd$. Also, $\Sigma = \text{diag}(\sigma_1, \dots, \sigma_K)$, where $0 \leq \sigma_1 \leq \dots \leq \sigma_K$. The matrices \mathbf{U} and \mathbf{V} are of size $N \times K$

and $K \times K$, respectively, and satisfy $\mathbf{U}^T \mathbf{U} = \mathbf{I}$ and $\mathbf{V}^T \mathbf{V} = \mathbf{V}\mathbf{V}^T = \mathbf{I}$, where \mathbf{I} is the identity matrix of size K [14]. When ∇ is of full rank, then the singular values satisfy $\sigma_j > 0$ for all $j = 1, \dots, K$ and the matrix Laplacian $\nabla^T \nabla = \mathbf{V}\Sigma^2\mathbf{V}^T$ is invertible. When ∇ is rank-deficient, then there are K_1 non-zero singular values and $K_0 = K - K_1$ zero singular values, say. For example, when $d = 2$ the nullity of ∇ is 1 so $K_1 = K - 1$. In this case, we write $\mathbf{U} = [\mathbf{U}_0 \ \mathbf{U}_1]$, $\Sigma = \text{diag}(\mathbf{O}, \Sigma_1)$, and $\mathbf{V} = [\mathbf{V}_0 \ \mathbf{V}_1]$, where \mathbf{O} is a matrix of zeros, so that $\nabla = \mathbf{U}_1 \Sigma_1 \mathbf{V}_1^T$ and the negative matrix Laplacian $\nabla^T \nabla = \mathbf{V}_1 \Sigma_1^2 \mathbf{V}_1^T$ is non-invertible, since $\mathbf{V}_1 \mathbf{V}_1^T \neq \mathbf{I}$.

The associated matrix analysis in Appendix G demonstrates that the spectral measure μ_{jk} underlying the Stieltjes integral representation of \mathfrak{S}_{jk}^* is given by

$$d\mu_{jk}(\lambda) = \sum_{n: \lambda_n^1 \leq \lambda} \langle m_{jk}(n) \delta_{\lambda_n^1}(d\lambda) \rangle, \quad (50)$$

where λ_n^1 , $n = 1, \dots, K_1$, are the eigenvalues of the matrix $-\imath \mathbf{U}_1^T \mathbf{H} \mathbf{U}_1$, while various equivalent representations of the spectral weights $m_{jk}(n)$, $j, k = 1, \dots, d$, are given in equation (G7) of Theorem 10 below. For notational simplicity, in this section we denote $\text{Re } \mu_{jk}$ by μ_{jk} . In our computations of μ_{jk} we used

$$m_{jk}(n) = \text{Re} [([\mathbf{r}_n^1]^\dagger \mathbf{U}_1^T \mathbf{H} \hat{\mathbf{e}}_j) ([\mathbf{r}_n^1]^\dagger \mathbf{U}_1^T \mathbf{H} \hat{\mathbf{e}}_k)], \quad n = 1, \dots, K_1, \quad (51)$$

which follows from equations (43), (44), (G6), and (G7). Here \mathbf{r}_n^1 , $n = 1, \dots, K_1$, are the *complex* eigenvectors of the matrix $-\imath \mathbf{U}_1^T \mathbf{H} \mathbf{U}_1$. Consequently $m_{kk}(n) \geq 0$, so μ_{kk} is a positive measure and μ_{jk} , $j \neq k$, is a signed measure, where $m_{jk}(n)$ in (51) can take positive or negative values.

To reveal the structure of μ_{12} and \mathfrak{S}_{12}^* in our numerical computations discussed in Section VB below, we denote the spectral weights $m_{jk}(n)$ associated with the Jordan decomposition $\mu_{jk} = \mu_{jk}^+ - \mu_{jk}^-$ in (27) by $m_{jk}^+(n)$ and $m_{jk}^-(n)$, where $m_{jk}^\pm(n) \geq 0$. Also, we define the functions $[\mathfrak{S}_{12}^*]^+$ and $[\mathfrak{S}_{12}^*]^-$

$$[\mathfrak{S}_{12}^*]^+(\varepsilon) = \max\{\mathfrak{S}_{12}^*(\varepsilon), 0\}, \quad [\mathfrak{S}_{12}^*]^- (\varepsilon) = \max\{-\mathfrak{S}_{12}^*(\varepsilon), 0\}, \quad (52)$$

for each $0 < \varepsilon < \infty$, so that $\mathfrak{S}_{12}^* = [\mathfrak{S}_{12}^*]^+ - [\mathfrak{S}_{12}^*]^-$, $[\mathfrak{S}_{12}^*]^\pm(\varepsilon) = \mathfrak{S}_{12}^*(\varepsilon; \mu_{12}^\pm)$, and $[\mathfrak{S}_{12}^*]^\pm \geq 0$.

In the case of a non-random fluid velocity field \mathbf{u} , we used $L = 200$ so that $K_1 = 39,999$. The eigenvalues λ_n^1 and eigenvectors \mathbf{r}_n^1 of the non-random Hermitian matrix $-\imath \mathbf{U}_1^T \mathbf{H} \mathbf{U}_1$ were computed using the Matlab function *eig()*. In this case, the averaging $\langle \cdot \rangle$ in (50) is interpreted

as spatial averaging over the period cell \mathcal{V} . In the setting of a randomly perturbed flow, we used $L = 100$ so that $K_1 = 9,999$. In this case, the averaging $\langle \cdot \rangle$ in (50) is interpreted as spatial averaging followed by ensemble averaging over $\sim 10^3$ statistical trials.

The numerical accuracy of the eigenvalue problem is determined by the *eigenvalue condition numbers* $\mathcal{K}(\lambda_n^1)$, $n = 1, \dots, K_1$, which are the reciprocals of the cosines of the angles between the left and right eigenvectors. Large eigenvalue condition numbers of a Hermitian matrix implies that it is near a matrix with multiple eigenvalues, while eigenvalue condition numbers close to 1 imply that the eigenvalue problem is well-conditioned. The eigenvalue problem for the matrix $-\imath \mathbf{U}_1^T \mathbf{H} \mathbf{U}_1$ is extremely well conditioned with $\max_n |1 - \mathcal{K}(\lambda_n^1)| \sim 10^{-14}$ typical, computed using Matlab's function *condeig()*.

To our knowledge, Matlab does not provide a function that describes the accuracy of the computed SVD of the matrix $\nabla = \mathbf{U} \Sigma \mathbf{V}^T$. In order to better understand the numerical accuracy in the entries of the matrix \mathbf{U} , which is central to our computational method, we performed the following tests. For the case of Dirichlet boundary conditions, the matrix ∇ is full-rank, hence the matrix Laplacian $\nabla^T \nabla$ is invertible. We computed the matrix $\Gamma = \nabla (\nabla^T \nabla)^{-1} \nabla^T$ directly using Matlab's *mldivide* function, i.e., $\Gamma = \nabla ((\nabla^T \nabla) \backslash \nabla^T)$, and also using the SVD of the matrix ∇ , with $\Gamma = \mathbf{U} \mathbf{U}^T$. We then computed the component-wise maximum difference $\max_{lm} |[\nabla ((\nabla^T \nabla) \backslash \nabla^T) - \mathbf{U} \mathbf{U}^T]_{lm}|$. When $L = 100$ and $L = 200$ this difference is $\sim 10^{-15}$, which gives an idea of the accuracy of the SVD of ∇ for the rank-deficient, periodic setting. The matrix Γ is used extensively throughout Appendix E. In all of our computations, Matlab's sparse architecture was employed wherever possible to reduce roundoff error.

B. Numerical Results

Before we discuss our numerical results in this section, it is helpful to first describe the relationship between the spectral measure μ_{jk} and the ε -behavior of \mathfrak{S}_{jk}^* . This relationship is easiest to understand when $j = k$, in terms of the enhancement in scalar transport above the bare diffusive value ε , as shown in equation (20). Consider μ_{kk} and \mathfrak{S}_{kk}^* , for some $k = 1, \dots, d$, and write the formula in (20) as

$$\mathfrak{S}_{kk}^*(\varepsilon) = \varepsilon + \mathcal{E}_{kk}(\varepsilon), \quad \mathcal{E}_{kk}(\varepsilon) = \varepsilon \int_{-\infty}^{\infty} \frac{d\mu_{kk}(\lambda)}{\varepsilon^2 + \lambda^2}, \quad (53)$$

where $\mathcal{E}_{kk}(\varepsilon) \geq 0$ denotes the *enhancement* above ε . By equation (15), the spectrum Σ of the self-adjoint operator M is a bounded subset of \mathbb{R} . Consequently, in the *diffusion dominated regime* where $\varepsilon \gg |\lambda|$ for all $\lambda \in \Sigma$, we have [20] $\mathfrak{S}_{kk}^* \sim \varepsilon + \mu_{kk}^0/\varepsilon$. The enhancement $\mathcal{E}_{kk}(\varepsilon) \sim \mu_{kk}^0/\varepsilon$ is only nominal in this regime where $\varepsilon \gg 1$ and is independent of the distribution of measure mass — dependent only the total mass. However, in the *advection dominated regime* where $\varepsilon \ll 1$, if the spectral measure μ_{kk} has significant mass near the spectral origin $\lambda = 0$, e.g., if the spectral weights $m_{kk}(n)$ in (50) have values significantly greater than zero for $|\lambda_n| \ll 1$, then the integrand associated with $\mathcal{E}_{kk}(\varepsilon)$ can introduce singular behavior that competes with the small ε prefactor in front of the integral, giving rise to a significant enhancement $\mathcal{E}_{kk}(\varepsilon)$ for $0 < \varepsilon \ll 1$. Although, if the mass of the measure is zero or extremely small in a neighborhood of $\lambda = 0$, then the enhancement $\mathcal{E}_{kk}(\varepsilon)$ can be less pronounced, since the small ε prefactor dominates the (lack of) singular behavior in the integrand near $\varepsilon = 0$. This illustrates that in the advection dominated regime, where $0 < \varepsilon \ll 1$, the ε -behavior of the enhancement $\mathcal{E}_{kk}(\varepsilon)$ depends strongly on the details of the spectral measure μ_{kk} near $\lambda = 0$.

We emphasize that, due to roundoff error and finite resolution ($L < \infty$) effects, our numerical approximations of μ_{jk} and the ε -behavior of \mathfrak{S}_{jk} breakdown for extremely small values of ε . For example, in the discrete setting, it is highly unlikely that $\lambda_n = 0$ is (exactly) a numerical eigenvalue solution of equation (30), even though in the continuum setting $\lambda = 0$ is an accumulation point [28, 56] of the discrete spectra for the compact [9, 10] operator M . Therefore, our numerical simulations can probe the ε -behavior of \mathfrak{S}_{jk} for moderately small values of ε but the approximation ultimately breaks down in the limit $\varepsilon \rightarrow 0$. However, for moderately small values of ε , our description above regarding the relationship between μ_{jk} and the ε -behavior of \mathfrak{S}_{jk} is still valid — illustrating that the details of the spectral measure μ_{jk} near the spectral origin $\lambda = 0$ strongly influence the ε -behavior of \mathfrak{S}_{jk} when $\varepsilon \ll 1$.

These concepts are illustrated in our computations of μ_{jk} and \mathfrak{S}_{jk} for “cat’s eye” flow displayed in Section V B 2 below. As the free parameter α increases from 0 to 1, the flow transitions from cell flow with closed streamlines to shear flow in the $y = x$ direction, as shown in Fig. 1. Our computations of μ_{jk} display a transitional behavior near $\lambda = 0$ which gives rise to a pronounced change in the ε -behavior of \mathfrak{S}_{jk} near $\varepsilon = 0$, as well as a significant enhancement in \mathfrak{S}_{kk} above the bare diffusive value ε .

As a benchmark result, we demonstrate in Section V B 1 that our computations accurately

capture the known behavior of μ_{kk} and \mathfrak{D}_{kk}^* for shear flow in the k th direction [4], where $\mu_{kk} = \mu_{kk}^0 \delta_0(d\lambda)$ and $\mathfrak{D}_{kk}^* = \varepsilon + \mu_{kk}^0/\varepsilon$. As another benchmark result, we demonstrate in Section V B 2 that our computations accurately capture the known [17, 18] asymptotic behavior $\mathfrak{D}_{kk}^* \sim \varepsilon^a$ with critical exponent $a = 1/2$, for $\varepsilon \ll 1$. In particular, the numerical methods developed in this manuscript compute $a \approx 0.54$, with a 8% error relative to the true value. For the sake of comparison, our Fourier approach to computing the spectral measure μ_{kk} discussed in [44] computes $a \approx 0.52$, with a 4% relative error, and our implementation of the linear systems approach to computing \mathfrak{D}_{kk}^* discussed in [48] computes $a \approx 0.49$ with a 2% relative error. This marked increase in the accuracy of the linear systems approach is largely due to the ability to handle larger matrix sizes which, in turn, is due to the $O(N^2)$ numerical complexity of the method compared to the $O(N^3)$ numerical complexity of the spectral measure method.

1. BC-shear flow

In the continuum setting, it is known [4] for shear flow in the x -direction that the measure μ_{11} is given by a δ -measure concentrated at the spectral origin, while $\mu_{22} \equiv 0$, and similarly for shear flow in the y -direction. As a baseline result, we computed the spectral measures and effective diffusivities for BC-shear-flow in both the x and y -directions, which are obtained for parameter values $(B, C) = (0, 1)$ and $(B, C) = (1, 0)$, respectively. Our computations for the components μ_{jk} , $j, k = 1, 2$, of the spectral measure for BC-shear-flow displayed in Fig. 2 are in good agreement with this theoretical prediction in [4].

Fig. 2 displays the streamlines for BC-shear-flow in (a) the x -direction and (b) the y -direction. In Fig. 2c the components \mathfrak{S}_{jk}^* , $j, k = 1, 2$, of the effective diffusivity matrix are displayed for BC-shear-flow in the x -direction. The analogous result for BC-shear-flow in the y -direction is visually identical to Fig. 2c under the mapping $\mathfrak{S}_{11}^* \leftrightarrow \mathfrak{S}_{22}^*$, i.e., under the exchange of the colors black \leftrightarrow blue. The components μ_{jk} , $j, k = 1, 2$, of the spectral measure are displayed for BC-shear-flow in (d) the x -direction and (e) the y -direction.

We focus our discussion on the results for BC-shear-flow in the x -direction, as the discussion regarding BC-shear-flow in the y -direction is analogous. For all $n = 1, \dots, K_1$, the spectral weights $m_{22}(n)$ in Fig. 2d satisfy $m_{22}(n) \lesssim 10^{-29}$. With the effects of finite resolution ($L < \infty$) and roundoff error associated with a machine epsilon of $\sim 10^{-16}$, these

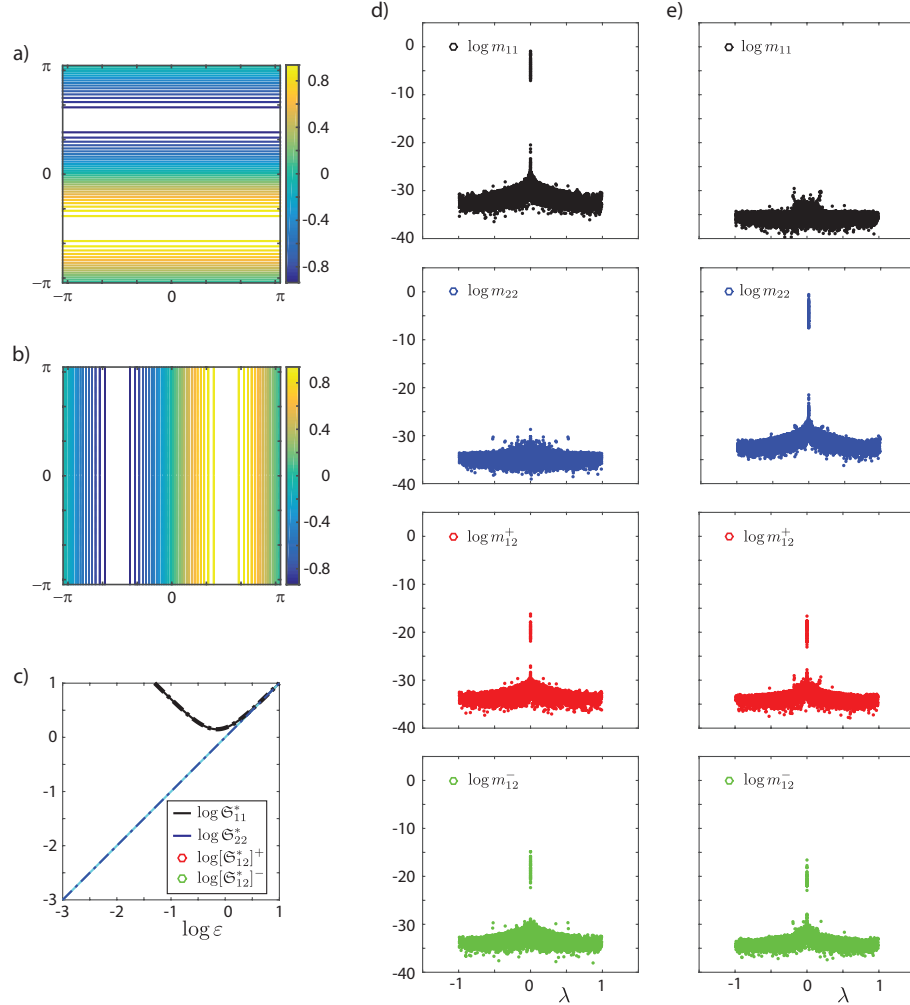


FIG. 2. Shear flow baseline result. The streamlines of BC-shear-flow in (a) the x -direction and (b) the y -direction. (c) The ε behavior of \mathfrak{S}_{jk}^* , $j, k = 1, 2$, for shear flow in the x -direction. The weights m_{jk} of the spectral measure $\text{Re } \mu_{jk}$ for shear flow in (d) the x -direction and (e) the y -direction as a function of λ . Consistent with theoretical predictions, the measure associated with the direction of the flow resembles a delta measure centered at the origin, while the other two components have spectral weights m_{jk} with very small magnitudes.

spectral weights can be considered “numerically zero.” The spectral weights $m_{12}^\pm(n)$ satisfy $m_{12}^\pm(n) \lesssim 10^{-28}$ for λ_n away from the spectral origin $\lambda = 0$ with a peak near $\lambda = 0$ having magnitudes $m_{12}^\pm(n) \lesssim 10^{-16}$. The spectral weights for the x -direction satisfy $m_{11}(n) \lesssim 10^{-28}$ away from $\lambda = 0$, while the weights near $\lambda = 0$ satisfy $10^{-9} \lesssim m_{11} \lesssim 10^{-1}$, resembling a δ -measure with virtually all of its mass concentrated near $\lambda = 0$. This is consistent with theoretical predictions [4]. Due to the anti-symmetry of the *real-valued* matrix $\mathbf{U}_1^T \mathbf{H} \mathbf{U}_1$, its

complex eigenvectors and purely imaginary eigenvalues come in complex conjugate pairs [25]. Consequently, the eigenvalues of the Hermitian matrix $-\imath \mathbf{U}_1^T \mathbf{H} \mathbf{U}_1$ come in \pm pairs with identical spectral weights, resulting in the symmetry about $\lambda = 0$ displayed by the spectral measures in Fig. 2.

Due to the high concentration of measure mass in μ_{11} very near the spectral origin, our computation of \mathfrak{S}_{11}^* displayed in Fig. 2c behaves like it's being governed by a delta function concentrated at the origin. In particular, Fig. 2c shows that the computed ε -behavior of \mathfrak{S}_{11}^* , displayed in black color with solid line-style, lays right on top of the graph of its upper bound $\varepsilon [1 + \mu_{11}^0 / \varepsilon^2]$ given in (24), with $\mu_{11}^0 \approx 4.975 \times 10^{-1}$, displayed in black color and dash-dot line-style. (We had to increase the line-width of the upper bound to be able to distinguish between the two black lines.) Due to the extremely small magnitudes of the spectral weights m_{22} and m_{12}^\pm , with measure masses $\mu_{22}^0 \approx 5.33 \times 10^{-29}$, $[\mu_{12}^0]^+ \approx 1.03 \times 10^{-16}$, and $[\mu_{12}^0]^- \approx 3.34 \times 10^{-15}$, both the upper and lower bounds for \mathfrak{S}_{22}^* and \mathfrak{S}_{12}^* in equations (24) and (25) are very close to ε and 0, respectively; the graph of \mathfrak{S}_{22}^* is virtually right on top of the lower bound ε in cyan color and solid line-style, and the magnitudes of $[\mathfrak{S}_{12}^*]^+$ and $[\mathfrak{S}_{12}^*]^-$ are so small they don't even appear. Since the support of the spectral measure is contained in the interval $[-1, 1]$, the components of the effective diffusivity approach their bare diffusive value $\varepsilon \delta_{jk}$ for large ε , as discussed above.

In [44] we developed Fourier methods for the computation of the spectral measure μ_{jk} for *BC*-cell flow, with $B = C = 1$. In particular, the eigenvalue problem $M\varphi_n = \lambda_n \varphi_n$ associated with the operator $M = -\imath \Delta^{-1} [\mathbf{u} \cdot \nabla]$ was transformed into an infinite algebraic system of equations defining a discrete, generalized eigenvalue problem. The Fourier coefficients of the eigenfunctions φ_n , $n = 1, 2, 3, \dots$, for the continuum setting comprise the components of the generalized eigenvectors in the discrete setting. Since we already treated *BC*-cell flow in [44], and for the sake of brevity, we now turn our attention to a discussion regarding our numerical results for “cat’s eye flow” displayed in Fig. 3.

2. Cat’s eye flow

Since the streamlines for cat’s eye flow in Fig. 1 are symmetric about the line $y = x$ for all $\alpha \in [0, 1]$, as discussed above, we anticipate that $\mu_{11} = \mu_{22}$. Our computations of the components μ_{jk} , $j, k = 1, 2$, of the spectral measure shown in Figures 3 and 5 display

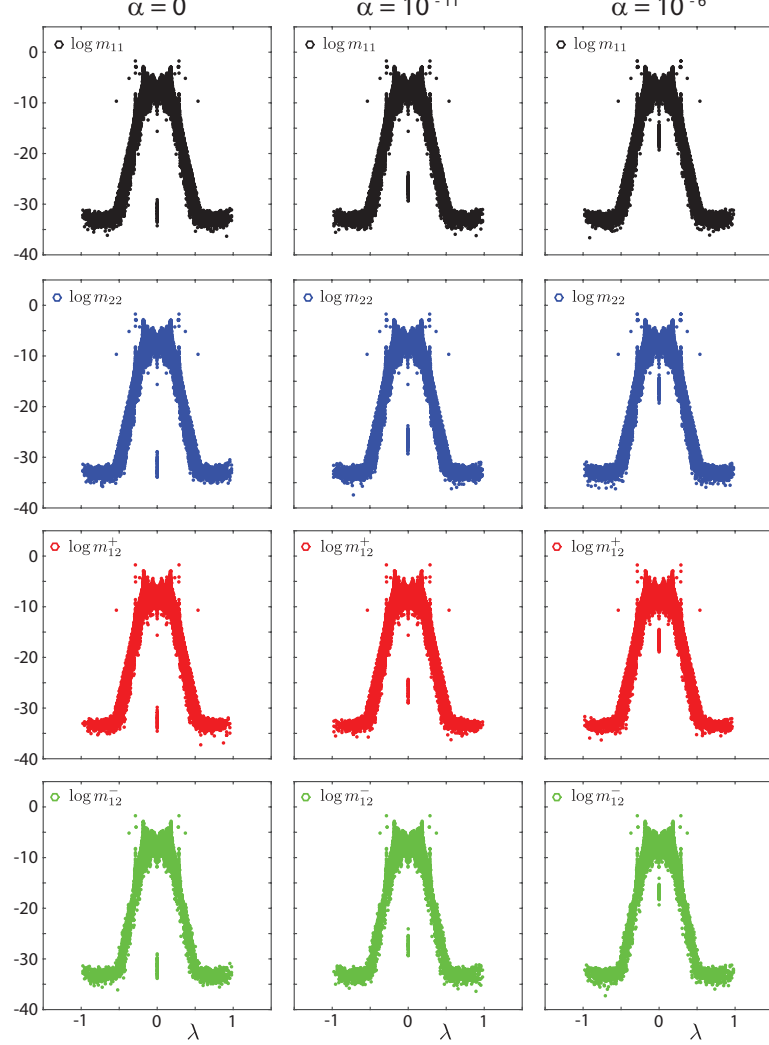


FIG. 3. Transition away from cat's eye cell flow. The spectral weights m_{jk} for the components $\text{Re } \mu_{jk}$, $j, k = 1, 2$, of the spectral measure are displayed with increasing values of the free parameter α from left to right. As the parameter α increases, the streamlines of the flow transition away from cell structures to open channels. This is reflected in the measure by a dramatic increase in the magnitude of the spectral weights m_{jk} associated with the “accumulation point” of the measure at $\lambda = 0$, while the other weights change only slightly.

this symmetry. A closer look at these figures reveals a deeper symmetry, namely that $\mu_{11} = \mu_{22} = |\mu_{12}|$, where $|\mu_{12}| = \mu_{12}^+ + \mu_{12}^-$ is the total variation of the signed measure μ_{12} introduced in equation (27), i.e., superimposing the panels for m_{12}^+ and m_{12}^- in Figures 3 and 5, yield the figure panels for m_{11} and m_{22} . We have also numerically verified the behavior $\mu_{11} = \mu_{22} = |\mu_{12}|$.

Since the operator $A = \Delta^{-1}[\nabla \cdot \mathbf{u}]$ is compact [9, 10], its spectra is discrete with an accumulation point at the spectral origin $\lambda = 0$ [56]. This accumulation point behavior of the measures μ_{jk} , $j, k = 1, 2$, can be seen in all of the panels of Fig. 3. When the parameter $\alpha = 0$, the streamlines of cat's eye flow are closed cell structures, as shown in Fig. 1, so that large scale transport occurs only when $\varepsilon > 0$ [17]. In this case, the computed “accumulation point” has eigenvalues λ_n with very small magnitude $10^{-19} \lesssim |\lambda_n| \lesssim 10^{-14}$. (It is clear that a finite number of eigenvalues does not constitute an accumulation point, but we will use this terminology to identify the concentration of eigenvalues near $\lambda = 0$ shown in Figures 3 – 5 and to set ideas.) However, the spectral measure weights $m_{kk}(n)$ and $m_{jk}^\pm(n)$ of the accumulation point have even smaller magnitudes with $10^{-35} \lesssim m_{kk}(n) \lesssim 10^{-29}$, and similarly for $m_{jk}^\pm(n)$, as shown in Fig. 3. Consequently, this component of the spectral measure does not contribute significantly to the enhancement $\mathcal{E}_{jk}(\varepsilon) = \varepsilon \sum_n m_{jk}(n)/(\varepsilon^2 + \lambda_n^2)$ of $\mathfrak{S}_{jk}^*(\varepsilon) = \varepsilon \delta_{jk} + \mathcal{E}_{jk}(\varepsilon)$. Plotting the panels of Fig. 3 with log scale x -axis reveals that there is a *gap* in the spectral measure with no spectra in the interval $10^{-14} \lesssim |\lambda_n| \lesssim 10^{-7}$, as shown in Fig. 4. The other component of the spectral measure has spectra in the interval $10^{-7} \lesssim |\lambda_n| \lesssim 10^0$ and weights $10^{-37} \lesssim m_{kk}(n) \lesssim 10^{-1}$. However, the part of this component of the spectral measure with spectral weights having more significant magnitudes $10^{-4} \lesssim m_{kk}(n) \lesssim 10^{-1}$ are associated with eigenvalues with magnitude $|\lambda_n| \gtrsim 10^{-1}$ and consequently also do not contribute significantly to the enhancement \mathcal{E}_{jk} .

When $0 < \alpha \ll 1$, open channels connect neighboring cells and large scale transport takes place both in thin boundary layers and within the channels [17]. This is reflected in the spectral measure $d\mu_{jk}(\lambda) = \sum_n \langle m_{jk}(n) \delta_{\lambda_n^1}(d\lambda) \rangle$ in equation (50) by a dramatic increase in the magnitude of the spectral weights $m_{kk}(n)$ and $m_{12}^\pm(n)$ associated with the accumulation point — by more than *14 orders of magnitude* with $10^{-19} \lesssim m_{kk}(n) \lesssim 10^{-15}$ — corresponding to a change of only 10^{-6} in the magnitude of α , as shown in Figures 3 and 4. The associated change in the spectral weights away from $\lambda = 0$ is nominal. However, Fig. 4 reveals that as α increases from 0 to 10^{-6} a localized portion of the accumulation point begins to migrate away from $\lambda = 0$ to the other component of the spectral measure with spectra in the interval $10^{-7} \lesssim |\lambda_n| \lesssim 10^0$ — decreasing the mass of the accumulation point for μ_{kk} . Moreover, all of the positive masses $m_{12}^+(n)$ migrate away from the accumulation point so the accumulation point of μ_{12} becomes comprised with purely negative weights. From this discussion, it is clear that the increased magnitudes of the masses comprising the accumulation point provide

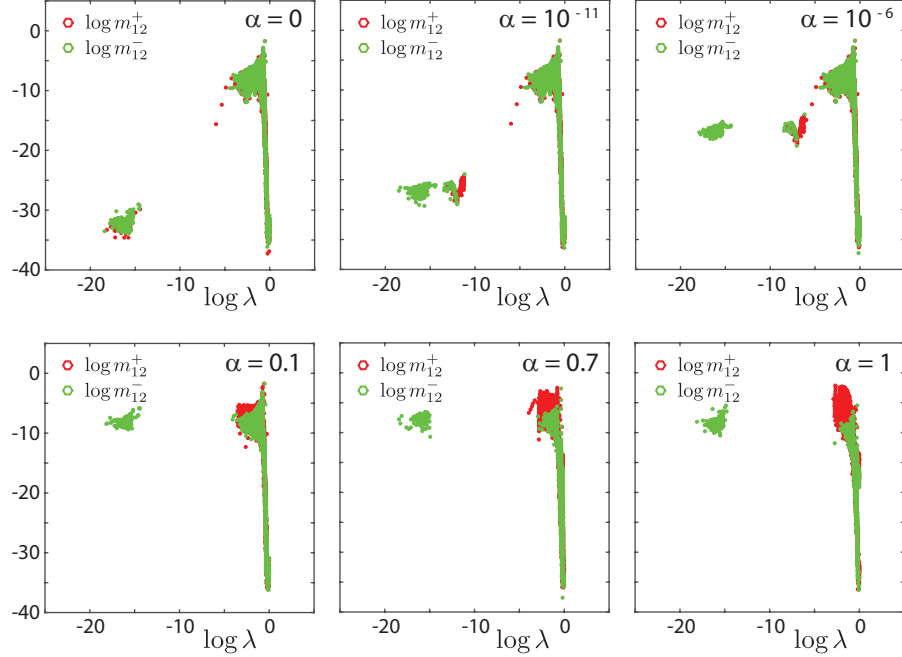


FIG. 4. Migration of positive measure mass from the computed “accumulation point” near the spectral origin. As the free parameter α of cat’s eye flow increases from zero, the magnitude of the spectral weights m_{12}^\pm comprising the accumulation point increase dramatically. Moreover, the spectra associated with the positive weights m_{12}^+ migrate away from the spectral origin until the accumulation point is comprised only of negative valued mass. The corresponding behavior for m_{kk} , $k = 1, 2$, is determined by the relation $\mu_{kk} = |\mu_{12}|$ between the components of the spectral measure $d\mu_{jk}(\lambda) = \sum_n \langle m_{jk}(n) \delta_{\lambda_n^1} d\lambda \rangle$.

an increased contribution to the enhancement $\mathcal{E}_{jk}(\varepsilon)$ for $\varepsilon \sim 10^{-14}$, for example, but only a moderate increase, and the increase in $\mathcal{E}_{jk}(\varepsilon)$ for $10^{-7} \lesssim \varepsilon \lesssim 10^0$ is also not significant.

As the value of α increases to $\alpha = 1$, the magnitudes of the masses comprising the accumulation point increase until they reach maximum values with $10^{-11} \lesssim m_{kk}(n) \lesssim 10^{-5}$, associated with eigenvalues with magnitudes $10^{-19} \lesssim |\lambda_n| \lesssim 10^{-14}$, as shown in Fig. 4. This marked increase in the magnitudes of the spectral weights provide a significant contribution to the enhancement $\mathcal{E}_{jk}(\varepsilon)$ for $\varepsilon \sim 10^{-14}$, for example. Moreover, as α increases in the range $(10^{-1}, 10^0)$, a significant transitional behavior arises in the other component of the spectral measure away from $\lambda = 0$, as shown in Figures 4 and 5. In particular, a bulge of measure weights with significant magnitude forms for eigenvalues in the range $10^{-4} \lesssim |\lambda_n| \lesssim 10^{-1}$, with a marked increase in weight magnitude from $10^{-7} \lesssim m_{kk}(n) \lesssim 10^{-4}$ to $10^{-7} \lesssim m_{kk}(n) \lesssim 10^{-2}$.

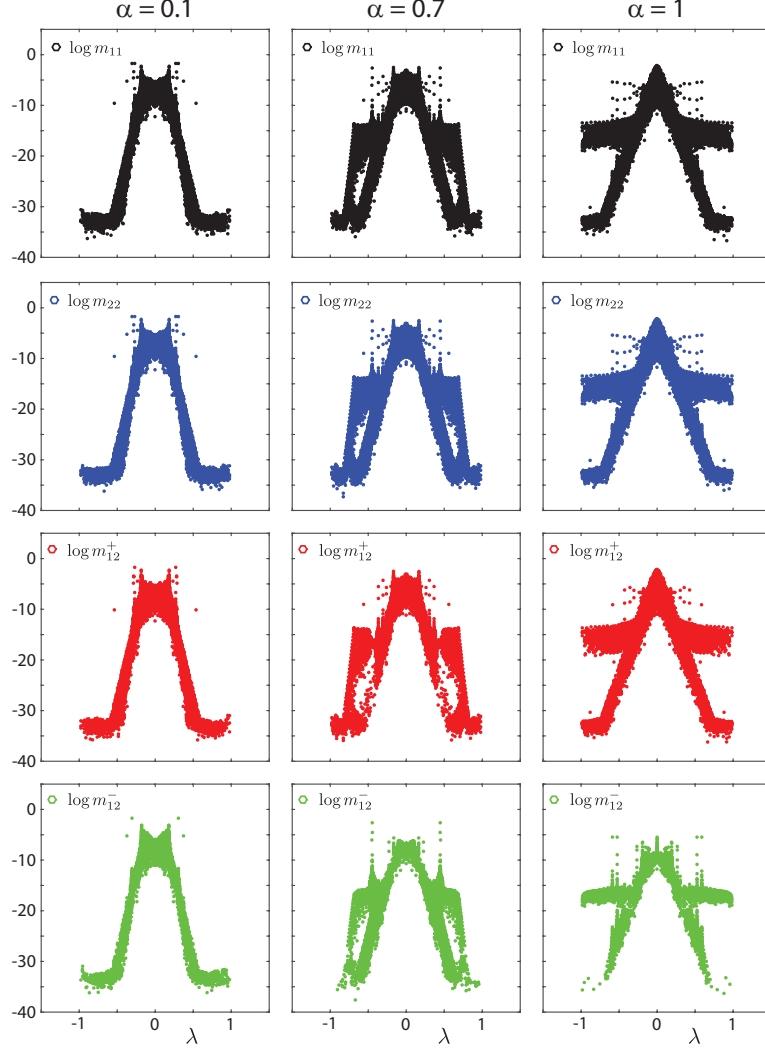


FIG. 5. Transition toward cat's eye shear flow. The spectral weights m_{jk} for the components $\text{Re } \mu_{jk}$, $j, k = 1, 2$, of the spectral measure are displayed with increasing values of the free parameter α from left to right. As the value of the parameter α increases, the streamlines become more elongated in the x - y diagonal direction, becoming shear flow when $\alpha = 1$. This is reflected in the spectral measure by an increase in the breadth of the spectral region with significant measure mass.

This provides a significant contribution to the enhancement $\mathcal{E}_{jk}(\varepsilon)$ even for $10^{-4} \lesssim \varepsilon \lesssim 10^{-1}$.

The behavior of \mathfrak{S}_{jk}^* that we deduced from the behavior of the spectral measure μ_{jk} is consistent with our computations of the components \mathfrak{S}_{jk}^* , $j, k = 1, 2$, of the matrix \mathfrak{S}^* , which are displayed in Fig. 6. Since the support of the spectral measure μ_{jk} is contained in the interval $[-1, 1]$, the components \mathfrak{S}_{jk}^* of the effective diffusivity approach their bare diffusive value $\varepsilon \delta_{jk}$ as ε surpasses $\varepsilon = 1$, as discussed in the beginning of Section V B.

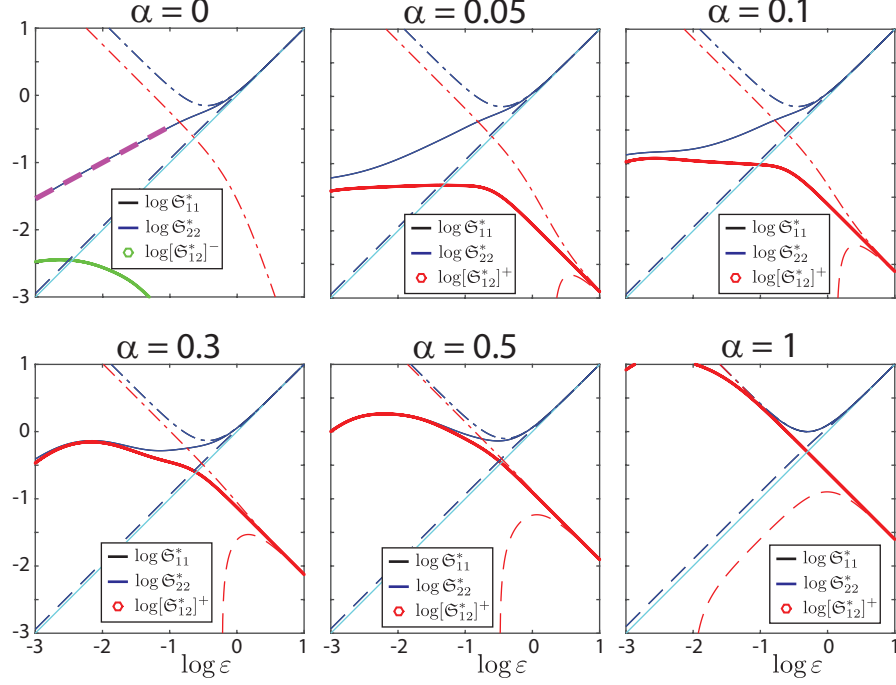


FIG. 6. Transitional behavior of the effective diffusivity from cat's eye cell flow to shear flow. The behavior of the components \mathfrak{S}_{jk}^* , $j, k = 1, 2$, of the effective diffusivity as a function of the non-dimensionalized molecular diffusivity ε and increasing values of the free parameter α from left to right and top to bottom. The upper and lower bounds corresponding to \mathfrak{S}_{jk}^* are in dash-dot and dashed line-style, respectively, and are the same line colors as the line colors for \mathfrak{S}_{kk}^* , $k = 1, 2$, and red for \mathfrak{S}_{12}^* . The trivial lower bound ε for \mathfrak{S}_{kk}^* is in cyan color and solid line-style. When the lower bound for \mathfrak{S}_{12}^* becomes negative it tends to $-\infty$ in this log-scale. For $\alpha = 0$, a polynomial fit to \mathfrak{S}_{kk}^* is also displayed in magenta color and dashed line-style. As the value of the parameter α increases and the flow transitions from cell to shear structure, there is a substantial enhancement in the effective diffusivity for small values of ε .

For cat's eye cell-flow, when $\alpha = 0$ the log-log plot of \mathfrak{S}_{kk}^* displays a linear trend for $10^{-3} \lesssim \varepsilon \lesssim 10^{-1}$, capturing the known [17, 18] power law behavior $\mathfrak{S}_{kk}^* \sim \varepsilon^a$ as $\varepsilon \rightarrow 0$. The polynomial fit $P(\varepsilon)$ to this line is given by $P(\varepsilon) = 0.54\varepsilon + 0.08$. This calculation of the critical exponent $a = 0.54$ has a 8% error relative to the value of the theoretical result $a = 1/2$ [17, 18]. The presence of spectral weights with magnitudes $10^{-7} \lesssim m_{kk}(n) \lesssim 10^{-4}$ and associated eigenvalues $10^{-4} \lesssim |\lambda_n| \lesssim 10^{-1}$ give rise to a moderate enhancement in \mathfrak{S}_{kk}^* . This enhancement increases from a fraction of an order of magnitude to one and a half orders

of magnitude above its bare diffusive value ε , as ε decreases from 10^{-1} to 10^{-3} , as shown in Fig. 3 for $\alpha = 0$.

We deduced from Fig. 3 that for $\alpha \in (0, 10^{-2})$ the behavior of the spectral measure gives rise to only a moderate enhancement $\mathcal{E}_{jk}(\varepsilon) = \varepsilon \sum_n m_{jk}(n)/(\varepsilon^2 + \lambda_n^2)$ of the effective diffusivity $\mathfrak{S}_{jk}^*(\varepsilon) = \varepsilon \delta_{jk} + \mathcal{E}_{jk}(\varepsilon)$ both for the advection dominated regime where $\varepsilon \sim 10^{-14}$, for example, and for the transitional regime $10^{-3} \lesssim \varepsilon \lesssim 10^{-1}$. This is consistent with the behavior of \mathfrak{S}_{jk}^* shown in Fig. 6 for $\alpha = 0$ and $\alpha = 0.05$. We further deduced from Figures 4 and 5 that for $\alpha \in (10^{-2}, 1)$ the behavior of the spectral measure gives rise to a significant enhancement for both $\varepsilon \sim 10^{-14}$ and $10^{-3} \lesssim \varepsilon \lesssim 10^{-1}$ where there is a marked increase in spectral weight magnitude from $10^{-7} \lesssim m_{kk}(n) \lesssim 10^{-4}$ to $10^{-7} \lesssim m_{kk}(n) \lesssim 10^{-2}$ for eigenvalues satisfying $10^{-4} \lesssim |\lambda_n| \lesssim 10^{-1}$. This is consistent with the panels of Fig. 6 corresponding to $0.1 \leq \alpha \leq 1$, with \mathfrak{S}_{jk}^* enhanced many orders of magnitude above its bare diffusive value $\delta_{jk} \varepsilon$, and \mathfrak{S}_{kk}^* as well as \mathfrak{S}_{12}^* closely following their upper bounds for $\varepsilon \gtrsim 10^{-0.5}$ when $\alpha = 1$.

We conclude this section with a description of various symmetries arising in our numerical computations and their consequences. We discussed above that our computations of μ_{jk} , $j = 1, 2$, display the symmetry $\mu_{11} = \mu_{22} = |\mu_{12}|$. This gives rise to the symmetry $\mathfrak{S}_{11}^*(\varepsilon) = \mathfrak{S}_{22}^*(\varepsilon) = \varepsilon + \mathcal{E}_{12}(\varepsilon; \mu_{12}^+) + \mathcal{E}_{12}(\varepsilon; \mu_{12}^-)$ between the components of the effective diffusivity, where we have denoted $\mathcal{E}_{jk}(\varepsilon; \mu_{jk}) = \varepsilon \int d\mu_{jk}(\lambda)/(\varepsilon^2 + \lambda^2)$, e.g., $\mathfrak{S}_{11}^*(\varepsilon) = \varepsilon + \mathcal{E}(\varepsilon; \mu_{11})$. The symmetry $\mathfrak{S}_{11}^* = \mathfrak{S}_{22}^*$ can be clearly seen in our computations of \mathfrak{S}_{jk}^* , $j, k = 1, 2$, displayed in Fig. 6; the two curves lay right on top of one another, as do their upper and lower bounds as $\mu_{11}^0 = \mu_{22}^0$. We have also numerically explored the empirical relationship $\mathfrak{S}_{11}^* \approx \varepsilon + [\mathfrak{S}_{12}^*]^+ + [\mathfrak{S}_{12}^*]^-$ by plotting \mathfrak{S}_{11}^* and $\varepsilon + [\mathfrak{S}_{12}^*]^+ + [\mathfrak{S}_{12}^*]^-$ on one graph. For most values of α and ε considered, the three curves lay virtually on top of each other (not shown), and when there is a deviation of $\varepsilon + [\mathfrak{S}_{12}^*]^+ + [\mathfrak{S}_{12}^*]^-$ from \mathfrak{S}_{11}^* , it is slight. This property also leads to the inequalities $\mathfrak{S}_{11}^* \geq \varepsilon + [\mathfrak{S}_{12}^*]^+$ and $\mathfrak{S}_{11}^* \geq \varepsilon + [\mathfrak{S}_{12}^*]^-$, with $\mathfrak{S}_{11}^* = \mathfrak{S}_{22}^*$, which is consistent with the behavior of \mathfrak{S}_{jk}^* shown in Fig. 6.

3. Randomly perturbed cat's eye flow

We now discuss our computations of the components μ_{jk} and \mathfrak{S}_{jk}^* , $j, k = 1, 2$, of the spectral measure and effective diffusivity matrix, respectively, for randomly perturbed cat's

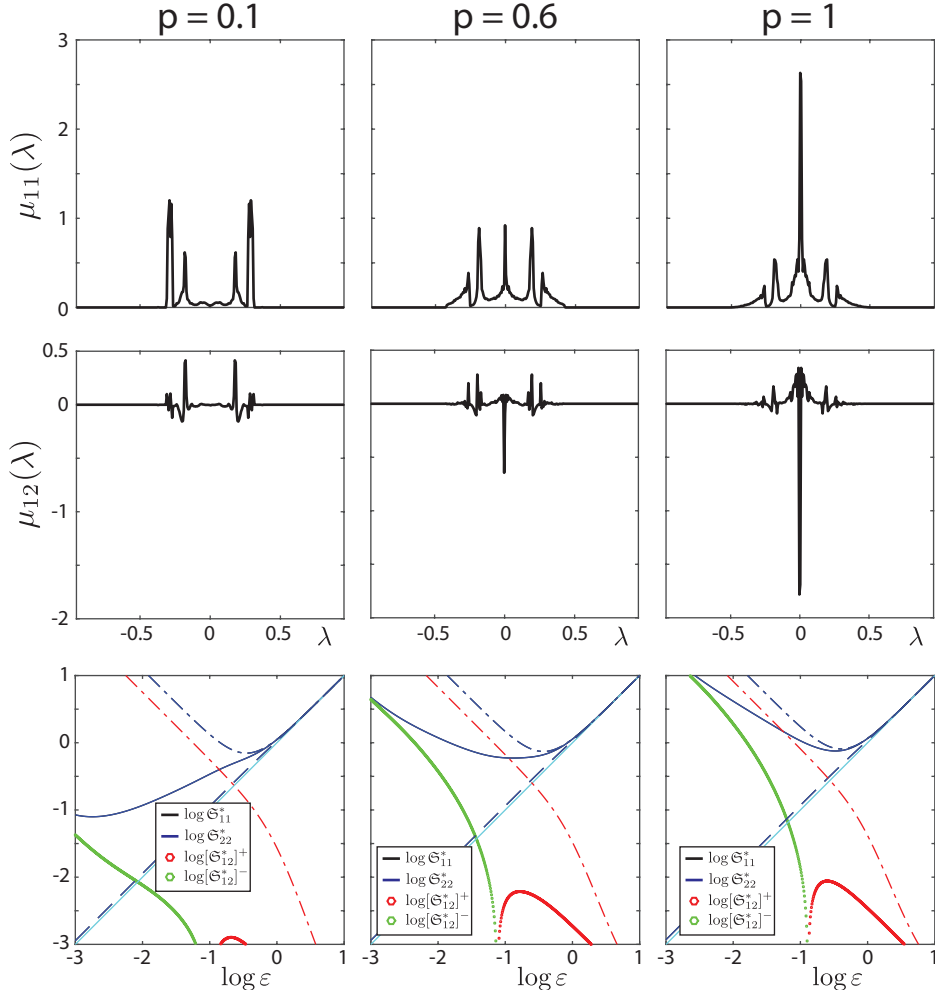


FIG. 7. Spectral functions and effective diffusivities for randomly perturbed cat's eye flow. The random parameter α is uniformly distributed on the interval $[0, p]$. The spectral functions $\mu_{jk}(\lambda)$ are displayed with corresponding effective diffusivities \mathfrak{S}_{jk}^* directly below for various values of p , increasing from left to right. As p increases and the streamlines of the flow become more elongated in the x - y direction, on average, the region about the spectral origin $\lambda = 0$ with substantial measure mass increases in breadth and magnitude. This gives rise to a substantial enhancement in the components \mathfrak{S}_{jk}^* of the effective diffusivity for larger values of the non-dimensionalized molecular diffusivity ε . The color scheme of the panels for \mathfrak{S}_{jk}^* is the same as that in Fig. 6.

eye flow with α uniformly distributed on the interval $[0, p]$. For each statistical trial of a sample space Ω_0 , with $|\Omega_0| \sim 10^3$ and $L = 100$, we computed *every* eigenvalue λ_n^1 and eigenvector \mathbf{r}_n^1 , $n = 1, \dots, K_1$, of the matrix $-\imath \mathbf{U}_1^T \mathbf{H} \mathbf{U}_1$ to form the spectral measure μ_{jk} in equation (50). In order to visually determine the behavior of the function $\mu_{jk}(\lambda) = \langle \mathbf{Q}(\lambda) \hat{\mathbf{e}}_j, \hat{\mathbf{e}}_k \rangle$ underlying

the spectral measure μ_{jk} , we plot a histogram representation of $\mu_{jk}(\lambda)$ called the *spectral function*, which we will also denote by $\mu_{jk}(\lambda)$. We now describe how we computed this graphical representation of the measure μ_{jk} . First, the spectral interval $I \supseteq \Sigma$ was divided into V sub-intervals I_v , $v = 1, \dots, V$, of equal length. In our computations of the spectral functions we typically used $V \sim 10^2$. Second, for fixed v , we identified all of the eigenvalues that satisfy $\lambda_n^1(\omega) \in I_v$, for $n = 1, \dots, K_1$ and $\omega \in \Omega_0$. The assigned value of $\mu_{jk}(\lambda)$ at the midpoint λ of the interval I_v , is the sum of the spectral weights $m_{jk}(\omega)$ associated with all such $\lambda_n^1(\omega) \in I_v$, normalized by $|\Omega_0|$. In this way, the area underneath the curve is the measure mass μ_{jk}^0 .

Consistent with the symmetries of the randomly perturbed flow, our computations of the spectral function satisfy $\mu_{11}(\lambda) = \mu_{22}(\lambda)$, hence the ensemble averaged components \mathfrak{S}_{jk}^* of the effective diffusivity also satisfy $\mathfrak{S}_{11}^* = \mathfrak{S}_{22}^*$, as shown in Fig. 7. Similar to our computations for non-random α , when $p = 0.1$ the measure mass of μ_{jk} , $j, k = 1, 2$, near the spectral origin $\lambda = 0$ is quite small and, on average, the region with significant magnitude increases in breadth as p increases, with the formation of a high concentration of measure mass at the spectral origin $\lambda = 0$ as $p \rightarrow 1$ — due to the incorporation of statistical realizations with near shear-flow characteristics associated with $\alpha \approx 1$. This average increase in the breadth of the region with significant mass and the formation of the high concentration of measure mass at $\lambda = 0$ gives rise to a substantial enhancement of the components \mathfrak{S}_{jk}^* of the effective diffusivity above the bare molecular diffusivity values $\varepsilon \delta_{jk}$. The sign changes in $\mu_{12}(\lambda)$ give rise to sign changes in $\mathfrak{S}_{12}^* = [\mathfrak{S}_{12}]^+ - [\mathfrak{S}_{12}]^-$. In the log-log plot of \mathfrak{S}_{12}^* a negative singularity forms in \mathfrak{S}_{12}^* at the location of sign changes.

VI. CONCLUSIONS

We adapted and extended two methods previously introduced in [3, 4] and [9, 10, 48] to provide new Stieltjes integral representations for the symmetric \mathfrak{S}^* and antisymmetric \mathfrak{A}^* parts of effective diffusivity matrix \mathfrak{D}^* in (19) — for all components of these homogenized matrices. Each integral representation involves the non-dimensionalized molecular diffusivity ε and a spectral measure of a self-adjoint operator acting on an appropriate Hilbert space. We utilized these integral representations to derive rigorous bounds for the off-diagonal components of the matrices \mathfrak{S}^* and \mathfrak{A}^* . We also proved the spectral measures of both methods

are identical, establishing that the two approaches yield equivalent spectral representations for \mathfrak{D}^* .

We developed discrete formulations of these two mathematical frameworks involving matrix representations of the self-adjoint operators and developed a standard and *non-standard* spectral theorem in terms of a standard and *generalized* eigenvalue problem, respectively. This matrix analysis provided the Stieltjes integral representations for \mathfrak{S}^* and \mathfrak{A}^* in (19), involving discrete spectral measures given explicitly in terms of the eigenvalues and eigenvectors of the matrices. We developed these discrete frameworks for both of the settings where the matrix gradient ∇ has Dirichlet boundary conditions, for example, and is therefore *full-rank*, and where ∇ has periodic boundary conditions and is therefore *rank-deficient*. In our studies of advection enhanced diffusion by a *periodic* fluid velocity field \mathbf{u} here, it is necessary to use a matrix gradient ∇ with periodic boundary conditions. We also proved, in both the full-rank and rank-deficient settings, that the spectral measures of both methods are identical, establishing that the two approaches yield equivalent spectral representations for the effective diffusivity matrix \mathfrak{D}^* . More specifically, this matrix analysis demonstrates both approaches can be formulated in terms of a common *standard* eigenvalue problem involving a matrix with the *smaller size* encountered in the generalized eigenvalue problem, thus combining the beneficial numerical attributes of both approaches.

We employed these discrete formulations to compute the components \mathfrak{S}_{jk}^* , $j, k = 1, \dots, d$, of the matrix \mathfrak{S}^* for some model 2D ($d = 2$) periodic flows and randomly perturbed periodic flows, by directly computing the associated discrete spectral measure $\text{Re } \mu_{jk}$. As a baseline result, we computed \mathfrak{S}_{jk}^* and $\text{Re } \mu_{jk}$ for *BC*-shear-flow, for which the spectral measure is known [4]. Our numerical results are in good agreement with the theoretical result. We also computed \mathfrak{S}_{jk}^* and $\text{Re } \mu_{jk}$ for the “cat’s eye” flow, for both the non-random and randomly perturbed settings, as a function of a free parameter. As the parameter varies, the flow transitions from cell-flow to shear-flow in the diagonal direction $y = x$. For cat’s eye cell-flow, our computations capture the known [17, 18] power law behavior $\mathfrak{S}_{kk}^* \sim \varepsilon^{1/2}$ for $\varepsilon \ll 1$. The spectral measure $\text{Re } \mu_{jk}$ and \mathfrak{S}_{jk}^* have transitional behavior as the parameter varies. This reveals how the details of $\text{Re } \mu_{kk}$ near the spectral origin govern the enhancement of \mathfrak{S}_{kk}^* above its bare diffusive value ε in the advection dominated regime where $\varepsilon \ll 1$, and similarly for \mathfrak{S}_{12}^* . Consistent with the symmetries of the flow, our computations indicate that $\text{Re } \mu_{11} = \text{Re } \mu_{22}$. Our computations of $\text{Re } \mu_{12}$ for cat’s eye flow also suggest a deeper

symmetry, namely $|\operatorname{Re} \mu_{12}| = \operatorname{Re} \mu_{11} = \operatorname{Re} \mu_{22}$, where $|\operatorname{Re} \mu_{12}|$ is the total variation of the signed measure $\operatorname{Re} \mu_{12}$. Our computations of \mathfrak{S}_{jk}^* are consistent with these symmetries and rigorous bounds derived in Theorem 2. In order to streamline the presentation of the main theoretical and numerical results in the body of the manuscript, we have placed more detailed developmental material in an appendix.

In almost 30 years since the initial formulation [3, 4] of Stieltjes integral representations for the effective diffusivity matrix \mathfrak{D}^* , analytical calculations of \mathfrak{D}^* have been obtained for only a few simple flows, such as shear flow. Our results help further advance the applicability of this spectral measure approach by providing a mathematical foundation for computation of spectral representations of \mathfrak{D}^* . For randomly perturbed periodic flows, the spectral method differs from more traditional methods in that it enables statistical investigation of the random eigenvalues and eigenvectors, thus connecting homogenization of advection diffusion processes to random matrix theory [45]. The results in this manuscript lay the groundwork for such investigations.

VII. ACKNOWLEDGMENTS

We gratefully acknowledge support from the Applied and Computational Analysis Program and the Arctic and Global Prediction Program at the US Office of Naval Research through grants N00014-12-10861, N00014-13-10291, and N00014-18-1-2552. We are also grateful for support from the Division of Mathematical Sciences at the U.S. National Science Foundation (NSF) through Grants DMS-0940249, DMS-1413454, DMS-1715680, DMS-1211179, and DMS-1522383. Finally, we would like to thank the NSF Math Climate Research Network (MCRN) for their support of this work.

Appendix A: Appendix overview

In order to streamline the presentation of the main theoretical and numerical results in the body of the manuscript, we have placed more detailed developmental material in a series of appendices here. We now give an overview of the topics covered in this appendix. In Appendix B, we comment on the notation used throughout this manuscript. In Appendix C, we derive important properties of the linear operator $A = \Delta^{-1}[\mathbf{u} \cdot \nabla]$ defined in equation (11).

In Theorem 1 of Section III we adapted and extended a method [9, 10, 48] involving a self-adjoint operator M acting on a Sobolev space of scalar-valued functions which provides the Stieltjes integral representations for \mathfrak{S}^* and \mathfrak{A}^* in equation (19). In Appendix D below, we adapt and extend a different method [3, 4] involving a self-adjoint operator \mathbf{M} acting on the Hilbert space of curl-free vector-valued functions which also leads to the Stieltjes integral representations for \mathfrak{S}^* and \mathfrak{A}^* in equation (19). These results are summarized in a corollary (Corollary 4) of Theorem 1.

In Theorem 5 of Appendix D, we prove that the spectral measures arising in Theorem 1 and Corollary 4 are identical, establishing that the two approaches yield equivalent spectral representations of \mathfrak{D}^* . This is accomplished by proving that the masses and all the moments of the two spectral measures are equal and citing the Hausdorff moment problem for measures with bounded support [1, 58]. In a corollary (Corollary 6) of Theorem 5 we utilize a one-to-one isometric correspondence [44] between the Sobolev space arising in Theorem 1 and the Hilbert space arising in Corollary 4, to extend the results of Theorem 5 to every spectral measure associated with the two self-adjoint operators M and \mathbf{M} . This corollary also proves that the masses and all the moments of the two spectral measures are equal in the generalized setting of a space-time periodic flow, possibly associated with chaotic dynamics and unbounded spectrum [44]. In the setting of unbounded spectrum the Hamburger or Stieltjes moment problems are instead relevant, and more conditions must be met beyond the equality of the masses and moments to ensure the measures are identical, such as Carleman's criterion [1]. In [44] an alternate method was used to determine that the spectral measures arising in the two different approaches are indeed identical in the time-dependent setting.

In Appendix E, we develop a discrete formulation of the mathematical framework given in Appendix D, involving a Hermitian matrix representation for the self-adjoint operator \mathbf{M} . We also briefly review the standard spectral theorem for Hermitian matrices. This provides the Stieltjes integral representations for \mathfrak{S}^* and \mathfrak{A}^* in (19) involving a discrete spectral measure, given explicitly in terms of the eigenvalues and eigenvectors of the matrix. This discrete framework holds for the setting where the matrix gradient has Dirichlet boundary conditions, for example, and is therefore *full-rank*. These results are analogues of those in Theorem 3 and are summarized in Corollary 7. In Theorem 8, we develop a *projection method* that is used to generalize the results in Theorem 3 and Corollary 7 to the setting where the matrix gradient has periodic boundary conditions, for example, and is therefore *rank-deficient*. The

results of Theorem 8 are also used to prove the discrete spectral representations arising in Theorem 3 and Corollary 7 are equivalent in this rank-deficient setting.

Specifically, in Lemma 9 of Appendix F, we use properties of the singular value decomposition of the matrix gradient ∇ to reveal symmetries between the two discrete approaches formulated in Section IV and Appendix E, establishing that the two approaches yield equivalent spectral representations of the effective diffusivity matrix \mathfrak{D}^* when ∇ is full-rank. In particular, we establish in the proof of Lemma 9 that the eigenvalues and generalized eigenvalues underlying the spectral measures for each method are in fact eigenvalues of a Hermitian matrix arising in both methods. Moreover, the eigenvectors \mathbf{w}_n and generalized eigenvectors \mathbf{z}_n of the two methods are related by $\mathbf{w}_n = \nabla \mathbf{z}_n$, which leads to the equivalence of the discrete spectral measures of the two approaches.

In Theorem 10 of Appendix G, we generalize Lemma 9 to the rank-deficient setting. This generalizes both the numerical algorithms developed in Section IV and Appendix E to the setting of periodic boundary conditions and combines beneficial numerical attributes of each algorithm. In Section V, this common method is used to compute \mathfrak{S}^* for model flows and relate spectral characteristics to flow geometry and transport properties.

Appendix B: Notation

We now briefly discuss the notation used throughout the manuscript. Operators are denoted by capital letters while functions comprising the domains of these operators are denoted by lowercase letters. (Capital letters are also used to denote the size of matrices.) Furthermore, vector-valued functions are denoted by lowercase bold font, e.g., $\boldsymbol{\xi}$, while scalar-valued functions are denoted by lowercase non-bold font, e.g., ξ . Matrices denoted by capital Latin letters are in math-serif font, e.g., H , B , C , Z , Q , A , U , V , W , etc. Integro-differential operators mapping scalar-valued functions to scalar-valued functions are in standard math-italic font, e.g., A and M . Integro-differential operators mapping vector-valued functions to vector-valued functions are in math-boldface font, e.g., \mathbf{A} and \mathbf{M} . We use a similar notation for differential operators, e.g., $\nabla \xi$ and $-\Delta \xi$ and their discrete, matrix counterparts $\nabla \boldsymbol{\xi}$ and $\nabla^T \nabla \boldsymbol{\xi}$, respectively. All homogenized matrices are in Gothic font and have a super-script asterisk, e.g., \mathfrak{D}^* , \mathfrak{S}^* , and \mathfrak{A}^* .

Appendix C: Properties of the linear operator A

In this section we derive various properties of the linear operator $A = \Delta^{-1}[\mathbf{u} \cdot \nabla]$ defined in equation (11). In particular, we demonstrate that A is antisymmetric on the Hilbert space $\mathcal{H}^{1,2}$ defined in (8). Moreover, we show that A is bounded on $\mathcal{H}^{1,2}$ and we provide an upper bound for $\|A\|_{1,2}$ when \mathbf{u} is uniformly bounded on the period cell \mathcal{V} .

We first show that the incompressibility condition $\nabla \cdot \mathbf{u} = 0$ implies that the operator A is antisymmetric on $\mathcal{H}^{1,2}$ [9, 10], i.e., $\langle Af, h \rangle_{1,2} = -\langle f, Ah \rangle_{1,2}$. On the Hilbert space \mathcal{H} defined in equation (7), the linear operator Δ^{-1} satisfies $\langle \Delta \Delta^{-1} f, h \rangle = \langle f, h \rangle$ in a distributional sense, for all $f, h \in \mathcal{H}$ [19, 37, 44]. Consequently, integration by parts and $\nabla \cdot \mathbf{u} = 0$ yields [9, 10, 44, 48]

$$\begin{aligned} \langle Af, h \rangle_{1,2} &= \langle [\nabla(\Delta^{-1})(\mathbf{u} \cdot \nabla)f] \cdot \nabla h \rangle \\ &= -\langle [(\mathbf{u} \cdot \nabla)f], h \rangle \\ &= -\langle [\nabla \cdot (\mathbf{u}f)], h \rangle \\ &= \langle f, [(\mathbf{u} \cdot \nabla)h] \rangle \\ &= \langle f, [\Delta(\Delta^{-1})(\mathbf{u} \cdot \nabla)h] \rangle \\ &= -\langle \nabla f \cdot [\nabla(\Delta^{-1})(\mathbf{u} \cdot \nabla)h] \rangle \\ &= -\langle f, Ah \rangle_{1,2}, \end{aligned} \tag{C1}$$

for all $f, h \in \mathcal{H}^{1,2}$ and real-valued incompressible \mathbf{u} (see [44] for more details).

Now, we derive the bound for $\|A\|_{1,2}$ given in equation (14). From the Cauchy-Schwartz inequality $|\langle f, h \rangle| \leq \|f\| \|h\|$ we have

$$\begin{aligned} \|Af\|_{1,2}^2 &= |\langle \nabla[\Delta^{-1}(\mathbf{u} \cdot \nabla f)] \cdot \nabla[\Delta^{-1}(\mathbf{u} \cdot \nabla f)], f \rangle| \\ &= |-\langle [\Delta^{-1}(\mathbf{u} \cdot \nabla f)], (\mathbf{u} \cdot \nabla f) \rangle| \\ &\leq \|\Delta^{-1}(\mathbf{u} \cdot \nabla f)\| \|\mathbf{u} \cdot \nabla f\| \\ &\leq \|\Delta^{-1}\| \|\mathbf{u} \cdot \nabla f\|^2. \end{aligned} \tag{C2}$$

We now provide an upper bound for $\|\mathbf{u} \cdot \nabla f\|$ when the components u_k , $k = 1, \dots, d$, of the fluid velocity field \mathbf{u} are uniformly bounded on the period cell \mathcal{V} . By the Cauchy-Schwartz inequality, $|\xi \cdot \zeta| \leq |\xi| |\zeta|$, we have

$$\|\mathbf{u} \cdot \nabla f\|^2 = \langle |\mathbf{u} \cdot \nabla f|^2 \rangle \leq \langle |\mathbf{u}|^2 |\nabla f|^2 \rangle \leq \sup_{\mathbf{x} \in \mathcal{V}} |\mathbf{u}(\mathbf{x})|^2 \|f\|_{1,2}^2. \tag{C3}$$

The result in equation (14) is now clear.

Appendix D: Curl-free fields and the effective diffusivity matrix

In this section, we adapt and extend an alternative method [3, 4] to the method discussed in Section III which leads to the integral representations for the symmetric \mathfrak{S}^* and anti-symmetric \mathfrak{A}^* parts of the effective diffusivity matrix \mathfrak{D}^* in equation (19). More specifically, in Appendix D 1 we provide functional formulas for \mathfrak{S}^* and \mathfrak{A}^* that are analogous to the formulas in (11). We review a Hilbert space formulation of this effective parameter problem [3, 4, 17, 18, 33] in Appendix D 2 which leads to a resolvent formula for $\nabla\chi_j$ that is analogous to the resolvent formula for χ_j in (12), involving a self-adjoint operator. We use this result and the spectral theorem [53, 58] to provide the Stieltjes integral representations for \mathfrak{S}^* and \mathfrak{A}^* in (19), involving a spectral measure of the operator. Finally, we prove the spectral measure corresponding to the Stieltjes integral representation for \mathfrak{D}^* in equation (19) of Theorem 1 is identical to the spectral measure corresponding the Stieltjes integral representation for \mathfrak{D}^* developed in the current section. This establishes that the two different approaches yield equivalent spectral representations of \mathfrak{D}^* .

1. Functional formulas for the effective diffusivity matrix

In this section, we derive functional formulas for the symmetric \mathfrak{S}^* and antisymmetric \mathfrak{A}^* parts of the effective diffusivity matrix \mathfrak{D}^* that are analogous to the formulas in equation (11). Using equation (29) and the representation of the fluid velocity field \mathbf{u} in (28), the advection diffusion equation in (1) can be written as a diffusion equation [17, 18],

$$\phi_t = \nabla \cdot [\mathbf{D} \nabla \phi], \quad \phi(0, \mathbf{x}) = \phi_0(\mathbf{x}), \quad \mathbf{D} = \varepsilon \mathbf{I} + \mathbf{H}. \quad (\text{D1})$$

Moreover, the cell problem in (4) can be written as a steady-state diffusion equation [17, 18],

$$\nabla \cdot [\mathbf{D}(\nabla \chi_k + \mathbf{e}_k)] = 0, \quad \langle \nabla \chi_k \rangle = 0, \quad k = 1, \dots, d. \quad (\text{D2})$$

Here, \mathbf{e}_k is a standard basis vector, $k = 1, \dots, d$, and $\mathbf{D}(\mathbf{x}) = \varepsilon \mathbf{I} + \mathbf{H}(\mathbf{x})$ can be viewed as a local diffusivity matrix with coefficients

$$D_{jk} = \varepsilon \delta_{jk} + H_{jk}, \quad j, k = 1, \dots, d, \quad (\text{D3})$$

where δ_{jk} is the Kronecker delta and \mathbf{l} is the identity operator on \mathbb{R}^d .

Substituting into equation (3) the expression for u_j in (4) and using equation (28), $\mathbf{u} = \nabla \cdot \mathbf{H}$, shows the components \mathfrak{S}_{jk}^* and \mathfrak{A}_{jk}^* of \mathfrak{S}^* and \mathfrak{A}^* can be written in terms of the following functional formulas involving the *real-valued* vector field $\nabla \chi_k$,

$$\mathfrak{S}_{jk}^* = \varepsilon(\delta_{jk} + \langle \nabla \chi_j \cdot \nabla \chi_k \rangle), \quad \mathfrak{A}_{jk}^* = \langle \mathbf{H} \nabla \chi_j \cdot \nabla \chi_k \rangle. \quad (\text{D4})$$

The functional formulas in (D4) are analogous to the functional formulas in equation (11). The symmetry $\mathfrak{S}_{jk}^* = \mathfrak{S}_{kj}^*$ of the matrix \mathfrak{S}^* follows from (D4) and the fact that the vector field $\nabla \chi_k$ is real-valued so that $\langle \nabla \chi_j \cdot \nabla \chi_k \rangle = \langle \nabla \chi_k \cdot \nabla \chi_j \rangle$. Moreover, the positivity condition $\langle \nabla \chi_k \cdot \nabla \chi_k \rangle = \langle |\nabla \chi_k|^2 \rangle \geq 0$ demonstrates that the effective transport of the scalar density ϕ is always *enhanced* by the presence of an incompressible velocity field, i.e., $\mathfrak{D}_{kk}^* = \mathfrak{S}_{kk}^* \geq \varepsilon$. The equality $\mathfrak{D}_{kk}^* = \mathfrak{S}_{kk}^*$ follows from the skew-symmetry of the matrix \mathfrak{A}^* , $\mathfrak{A}_{kj}^* = -\mathfrak{A}_{jk}^*$, hence $\mathfrak{A}_{kk}^* = 0$. The skew-symmetry of \mathfrak{A}^* follows from the skew-symmetry of the *real-valued* matrix \mathbf{H} , $\mathfrak{A}_{jk}^* = \langle \mathbf{H} \nabla \chi_j \cdot \nabla \chi_k \rangle = -\langle \nabla \chi_j \cdot \mathbf{H} \nabla \chi_k \rangle = -\langle \mathbf{H} \nabla \chi_k \cdot \nabla \chi_j \rangle = -\mathfrak{A}_{kj}^*$.

2. The analytic continuation method and integral representations of \mathfrak{D}^*

In this section we begin by noting that the cell problem in equation (D2) is equivalent [3, 4, 17, 18] to the quasi-static limit of Maxwell's equations [22, 27, 40], which describe the transport properties of an electromagnetic wave in a composite material,

$$\nabla \times \mathbf{E}_k = 0, \quad \nabla \cdot \mathbf{J}_k = 0, \quad \mathbf{J}_k = \mathbf{D} \mathbf{E}_k, \quad \langle \mathbf{E}_k \rangle = \mathbf{e}_k, \quad \mathbf{D} = \varepsilon \mathbf{l} + \mathbf{H}. \quad (\text{D5})$$

Here, $\mathbf{E}_k = \nabla \chi_k + \mathbf{e}_k$ plays the role of the local electric field, $\mathbf{J}_k = \mathbf{D} \mathbf{E}_k$ plays the role of the local current density, and $\mathbf{D} = \varepsilon \mathbf{l} + \mathbf{H}$ plays the role of the local conductivity matrix of the medium. Since \mathbf{H} is skew-symmetric, the intensity-flux relation $\mathbf{J}_k = \mathbf{D} \mathbf{E}_k$ is not the usual Fourier law, but instead resembles that of a Hall medium [17, 18, 26, 40].

In [3, 4], the analytic continuation method for representing transport in composites was adapted to provide a Stieltjes integral representation for the symmetric part of the effective diffusivity matrix \mathfrak{D}^* , involving a spectral measure of a self-adjoint operator. This method provides Stieltjes integral representations for the bulk transport coefficients of composite media [22], such as the effective electrical conductivity. This method is based on the spectral theorem of Hilbert space theory and a resolvent formula for, say, the electric field, involving a

self-adjoint operator [22] or matrix [42] which depends only on the composite geometry. In this section, we adapt the method developed in [3, 4] to provide Stieltjes integral representations for *both* the symmetric and antisymmetric parts of the effective diffusivity matrix \mathfrak{D}^* , which encodes the flow geometry of the fluid velocity field in a spectral measure of a self-adjoint operator.

Following the discussion leading to equation (8), we consider a fluid velocity field that is spatially periodic on a region $\mathcal{V} \subset \mathbb{R}^d$, and define the Hilbert space \mathcal{H} [18, 33]

$$\mathcal{H} = \{\boldsymbol{\xi} \in \otimes_{n=1}^d L^2(\mathcal{V}, \nu) : \boldsymbol{\xi}(\mathbf{x}) \text{ is periodic in } \mathcal{V} \text{ and } \langle \boldsymbol{\xi} \rangle = 0\}, \quad (\text{D6})$$

which is analogous to the Hilbert space \mathcal{H} defined in equation (7), where \mathcal{H} is defined over vector-fields instead of scalar-fields as in \mathcal{H} . The Hilbert space \mathcal{H} is equipped with a sesquilinear inner-product $\langle \cdot, \cdot \rangle$ defined by $\langle \boldsymbol{\xi}, \boldsymbol{\zeta} \rangle = \langle \boldsymbol{\xi} \cdot \boldsymbol{\zeta} \rangle$, with $\boldsymbol{\xi} \cdot \boldsymbol{\zeta} = \boldsymbol{\xi}^\dagger \boldsymbol{\zeta}$, \dagger is the operation of complex-conjugate-transpose, and $\langle \boldsymbol{\zeta}, \boldsymbol{\xi} \rangle = \overline{\langle \boldsymbol{\xi}, \boldsymbol{\zeta} \rangle}$ for $\boldsymbol{\xi}, \boldsymbol{\zeta} \in \mathcal{H}$. This inner-product induces a norm $\|\cdot\|$ defined by $\|\boldsymbol{\xi}\| = \langle \boldsymbol{\xi}, \boldsymbol{\xi} \rangle^{1/2}$ and $\boldsymbol{\xi} \in \mathcal{H}$ implies that $\|\boldsymbol{\xi}\| < \infty$. Now consider the associated Hilbert space \mathcal{H}_x of curl-free fields [4, 17, 18, 22, 40, 44],

$$\mathcal{H}_x = \{\boldsymbol{\xi} \in \mathcal{H} : \boldsymbol{\nabla} \times \boldsymbol{\xi} = 0 \text{ weakly and } \langle \boldsymbol{\xi} \rangle = 0\}. \quad (\text{D7})$$

The curl-free vector field $\boldsymbol{\nabla} \chi_k$ in the cell problem in (D2) is mean-zero $\langle \boldsymbol{\nabla} \chi_k \rangle = 0$. When the matrix D in equation (D1) is bounded in the operator norm $\|\cdot\|$ induced by the \mathcal{H} -inner-product [20], $\|D\| < \infty$, then there exists unique $\boldsymbol{\nabla} \chi_k \in \mathcal{H}_x$ satisfying equation (D2) [22, 46]. We assume that

$$0 < \varepsilon < \infty, \quad \|H\| < \infty, \quad (\text{D8})$$

which together imply $\|D\| < \infty$.

The linear operator $\boldsymbol{\Gamma} = \boldsymbol{\nabla}(\Delta^{-1})\boldsymbol{\nabla} \cdot$ is a projection onto the Hilbert space \mathcal{H}_x in the sense that $\boldsymbol{\Gamma} : \mathcal{H} \mapsto \mathcal{H}_x$ and $\boldsymbol{\Gamma} \boldsymbol{\xi} = \boldsymbol{\xi}$ (weakly) for all $\boldsymbol{\xi} \in \mathcal{H}_x$, in particular $\boldsymbol{\Gamma} \boldsymbol{\nabla} \chi_k = \boldsymbol{\nabla} \chi_k$ [17, 44]. It is based on convolution with respect to the Green's function for the Laplacian $\Delta = \nabla^2$ [38, 56]. Applying the integro-differential operator $\boldsymbol{\nabla} \Delta^{-1}$ to the cell problem in equation (D2) yields $\boldsymbol{\Gamma}[(\varepsilon I + H)(\boldsymbol{\nabla} \chi_k + \mathbf{e}_k)] = 0$. Since $\boldsymbol{\Gamma} \mathbf{e}_k = 0$ and $\boldsymbol{\Gamma} \boldsymbol{\nabla} \chi_k = \boldsymbol{\nabla} \chi_k$, this formula is equivalent to $(\varepsilon I + \boldsymbol{\Gamma} H \boldsymbol{\Gamma}) \boldsymbol{\nabla} \chi_k = -\boldsymbol{\Gamma} H \mathbf{e}_k$, which yields the following resolvent formula for $\boldsymbol{\nabla} \chi_k$

$$\boldsymbol{\nabla} \chi_k = (\varepsilon I + A)^{-1} \mathbf{g}_k, \quad A = \boldsymbol{\Gamma} H \boldsymbol{\Gamma}, \quad \mathbf{g}_k = -\boldsymbol{\Gamma} H \mathbf{e}_k, \quad (\text{D9})$$

which is analogous to equation (12). Since Γ is a projection operator onto $\mathcal{H}_x \subset \mathcal{H}$, it is bounded by unity in operator norm on \mathcal{H} , $\|\Gamma\| \leq 1$ [20, 54]. Integration by parts and the symmetry of the operator Δ^{-1} [56] (or the projective nature of Γ itself) shows that Γ is also a *symmetric* operator, i.e., $\langle \Gamma \xi \cdot \zeta \rangle = \langle \xi \cdot \Gamma \zeta \rangle$ for all $\xi, \zeta \in \mathcal{H}$ [44]. These two properties show that Γ with domain \mathcal{H} is a *self-adjoint* operator [53]. Since Γ is self-adjoint and $\Gamma \nabla \chi_k = \nabla \chi_k$, we may write \mathfrak{A}_{jk}^* in equation (D4) as $\mathfrak{A}_{jk}^* = \langle \mathbf{A} \nabla \chi_j \cdot \nabla \chi_k \rangle$. Consequently, substituting the resolvent formula for $\nabla \chi_k$ in equation (D9) into the functional formulas in equation (D4) yields

$$\begin{aligned}\mathfrak{S}_{jk}^* &= \varepsilon(\delta_{jk} + \langle (\varepsilon I + \mathbf{A})^{-1} \mathbf{g}_j \cdot (\varepsilon I + \mathbf{A})^{-1} \mathbf{g}_k \rangle), \\ \mathfrak{A}_{jk}^* &= \langle \mathbf{A} (\varepsilon I + \mathbf{A})^{-1} \mathbf{g}_j \cdot (\varepsilon I + \mathbf{A})^{-1} \mathbf{g}_k \rangle,\end{aligned}\quad (\text{D10})$$

which is a direct analogue of equation (13).

Since Γ is self-adjoint on \mathcal{H} , the anti-symmetry of the matrix H implies that $\mathbf{A} = \Gamma \mathsf{H} \Gamma$ is an *antisymmetric* operator on \mathcal{H} , i.e., $\langle \mathbf{A} \xi \cdot \zeta \rangle = -\langle \xi \cdot \mathbf{A} \zeta \rangle$. We emphasize that the operator \mathbf{A} depends only on the fluid velocity field via equation (28). By equation (D8), the operator \mathbf{A} is bounded on \mathcal{H} with $\|\mathbf{A}\| \leq \|\mathsf{H}\| < \infty$. This, the skew-symmetry of \mathbf{A} , and the sesquilinearity of the \mathcal{H} -inner-product imply that $\mathbf{M} = -\imath \mathbf{A}$, where $\imath = \sqrt{-1}$, is a bounded symmetric operator, hence self-adjoint on \mathcal{H} with $\|\mathbf{M}\| = \|\mathbf{A}\| < \infty$. The spectrum Σ of the self-adjoint operator \mathbf{M} is real-valued with spectral radius equal to its operator norm [53], thus

$$\Sigma \subseteq [-\|\mathsf{H}\|, \|\mathsf{H}\|]. \quad (\text{D11})$$

We are now ready to present the main results of this section. We start with the following corollary of Theorem 1.

Corollary 4 *Let $\mathbf{Q}(\lambda)$ denote the resolution of the identity corresponding to the self-adjoint operator \mathbf{M} . Then, the components \mathfrak{S}_{jk}^* and \mathfrak{A}_{jk}^* , $j, k = 1, \dots, d$, of the symmetric \mathfrak{S}^* and antisymmetric \mathfrak{A}^* parts of the effective diffusivity matrix \mathfrak{D}^* have the Stieltjes-Radon integral representations in (19) with μ_{jk} replaced by the spectral measure $\tilde{\mu}_{jk}$ of \mathbf{M} in the $(\mathbf{g}_j, \mathbf{g}_k)$ state. The bounds in Theorem 2 hold for these integral representations for \mathfrak{S}_{jk}^* and \mathfrak{A}_{jk}^* . The mass $\tilde{\mu}_{jk}^0$ of the measure $\tilde{\mu}_{jk}$ is real-valued and satisfies*

$$\tilde{\mu}_{jk}^0 = \langle \mathsf{H}^T \Gamma \mathsf{H} \mathbf{e}_j \cdot \mathbf{e}_k \rangle, \quad |\mu_{jk}^0| \leq \|\mathsf{H}\|^2 < \infty. \quad (\text{D12})$$

Proof of Corollary 4. Exactly as in the proof of Theorem 1, equation (D10) and a direct analogue of equation (17) leads to the Stieltjes integral representations in (19), involving a Stieltjes measure $\tilde{\mu}_{jk}$ associated with the function of the spectral variable λ defined by $\tilde{\mu}_{jk}(\lambda) = \langle \mathbf{Q}(\lambda)\mathbf{g}_j, \mathbf{g}_k \rangle$. Here $\mathbf{g}_k = -\boldsymbol{\Gamma}\mathbf{H}\mathbf{e}_k$ is defined in (D9) and $\{\mathbf{Q}(\lambda)\}_{\lambda \in \Sigma}$ is the family of self-adjoint projection operators that is in one-to-one correspondence with the bounded linear self-adjoint operator \mathbf{M} on the Hilbert space \mathcal{H}_\times [53, 58]. From equation (18) and the fact that $\boldsymbol{\Gamma}$ is a self-adjoint projection operator on \mathcal{H}_\times , the mass $\tilde{\mu}_{jk}^0$ of the measure $\tilde{\mu}_{jk}$ is real-valued and satisfies

$$\tilde{\mu}_{jk}^0 = \langle \mathbf{g}_j, \mathbf{g}_k \rangle = \langle \boldsymbol{\Gamma}\mathbf{H}\mathbf{e}_j \cdot \boldsymbol{\Gamma}\mathbf{H}\mathbf{e}_k \rangle = \langle \mathbf{H}^T \boldsymbol{\Gamma}\mathbf{H}\mathbf{e}_j \cdot \mathbf{e}_k \rangle, \quad |\tilde{\mu}_{jk}^0| \leq \|\mathbf{H}\|^2 < \infty. \quad (\text{D13})$$

By analogy, the bounds in Theorem 2 also hold for these integral representations for \mathfrak{S}_{jk}^* and \mathfrak{A}_{jk}^* . This concludes our proof of Corollary 4 \square .

It is worth making the following observation. In the current setting, the formulas for \mathfrak{S}_{jk}^* and \mathfrak{A}_{jk}^* in (19) are computed with respect to the standard basis $\{\mathbf{e}_k\}$, through the definition of $\tilde{\mu}_{jk}(\lambda) = \langle \mathbf{Q}(\lambda)\mathbf{g}_j, \mathbf{g}_k \rangle$ with $\mathbf{g}_k = -\boldsymbol{\Gamma}\mathbf{H}\mathbf{e}_k$. We now show that, given \mathfrak{S}_{jk}^* and \mathfrak{A}_{jk}^* , $j, k = 1, \dots, d$, the effective diffusivity matrix can be computed relative to any directions. This is due to the bilinearity of the inner-product underlying the definition of $\tilde{\mu}_{jk}(\lambda)$. More specifically, if $\boldsymbol{\xi}, \boldsymbol{\zeta} \in \mathbb{R}^d$ are arbitrary directions of interest, then $\langle \mathbf{Q}(\lambda)\boldsymbol{\Gamma}\mathbf{H}\boldsymbol{\xi}, \boldsymbol{\Gamma}\mathbf{H}\boldsymbol{\zeta} \rangle = \sum_{jk} a_j b_k \langle \mathbf{Q}(\lambda)\mathbf{g}_j, \mathbf{g}_k \rangle$, where the constants a_j and b_k , $j, k = 1, \dots, d$, are the coordinates of the vectors $\boldsymbol{\xi}$ and $\boldsymbol{\zeta}$ with respect to the standard basis. This immediately leads to integral representations for the effective diffusivity matrix relative to any desired directions. This observation had useful consequences in [17, 18].

Theorem 5 *The spectral measure μ_{jk} in Theorem 1 is identical to the spectral measure $\tilde{\mu}_{jk}$ in Corollary 4.*

$$\mu_{jk} \equiv \tilde{\mu}_{jk}. \quad (\text{D14})$$

Before we prove Theorem 5, we give a brief outline of the proof and display the key formulas that lead to the result in (D14). The vector field $\mathbf{g}_k = -\boldsymbol{\Gamma}\mathbf{H}\mathbf{e}_k$ defined in equation (D9) and the scalar field $g_k = (-\Delta)^{-1}u_k$ defined in (12) are (weakly) related by [44]

$$\mathbf{g}_k = \boldsymbol{\nabla} g_k. \quad (\text{D15})$$

The operator $\mathbf{A} = \mathbf{\Gamma}\mathbf{H}\mathbf{\Gamma}$ defined in equation (D9) and the operator $A = \Delta^{-1}[\mathbf{u}\cdot\mathbf{\nabla}]$ defined in (12), hence $\mathbf{M} = -\imath\mathbf{A}$ and $M = -\imath A$, are (weakly) related by

$$\mathbf{A}\mathbf{\nabla} = \mathbf{\nabla}A, \quad \mathbf{M}\mathbf{\nabla} = \mathbf{\nabla}M. \quad (\text{D16})$$

It follows that the masses and moments of the spectral measure μ_{jk} , $j, k = 1, \dots, d$, in Theorem 1 and the spectral measure $\tilde{\mu}_{jk}$ in Corollary 4 are identical.

$$\mu_{jk}^n = \tilde{\mu}_{jk}^n, \quad n = 0, 1, 2, \dots. \quad (\text{D17})$$

Since the self-adjoint operators \mathbf{M} and M are bounded, hence the spectra of these operators are bounded subsets of \mathbb{R} and the Hausdorff moment problem is determinate [1, 58], this establishes equation (D14).

Proof of Theorem 5. In [44], equations (D15) and (D16) were established in a more general context than our considerations here, where $\mathbf{u} = \mathbf{u}(\mathbf{x}, t)$ is periodic in both space and time t . We will see that the proof of equation (D17) essentially depends only on equations (D15) and (D16). Consequently, en route, we will also establish that equation (D17) holds for this more general, time-dependent context. Here, we will only sketch the key ideas that were developed at length in [44]. Equation (28), $\mathbf{u} = \mathbf{\nabla}\cdot\mathbf{H}$, and the definitions $\mathbf{\Gamma} = \mathbf{\nabla}(\Delta^{-1})\mathbf{\nabla}\cdot$, $\mathbf{g}_k = -\mathbf{\Gamma}\mathbf{H}\mathbf{e}_k$, and $g_k = (-\Delta)^{-1}u_k$, together yield [44] equation (D15)

$$\mathbf{g}_j = -\mathbf{\Gamma}\mathbf{H}\mathbf{e}_j = \mathbf{\nabla}(-\Delta)^{-1}u_j = \mathbf{\nabla}g_j. \quad (\text{D18})$$

Consequently, by equation (18) the masses μ_{jk}^0 and $\tilde{\mu}_{jk}^0$ of the spectral measures μ_{jk} and $\tilde{\mu}_{jk}$ are equal

$$\tilde{\mu}_{jk}^0 = \langle \mathbf{g}_j \cdot \mathbf{g}_k \rangle = \langle \mathbf{\nabla}g_j \cdot \mathbf{\nabla}g_k \rangle = \langle g_j, g_k \rangle_{1,2} = \mu_{jk}^0. \quad (\text{D19})$$

Since $\mathbf{\Gamma}\mathbf{\nabla}\xi = \mathbf{\nabla}\xi$ (weakly) [44], equation (28) and equation (29), $\mathbf{\nabla}\cdot[\mathbf{H}\mathbf{\nabla}] = [\mathbf{\nabla}\cdot\mathbf{H}]\cdot\mathbf{\nabla}$, imply that for all $\xi \in \mathcal{H}^{1,2}$

$$\mathbf{A}\mathbf{\nabla}\xi = \mathbf{\Gamma}\mathbf{H}\mathbf{\Gamma}\mathbf{\nabla}\xi = \mathbf{\Gamma}\mathbf{H}\mathbf{\nabla}\xi = \mathbf{\nabla}[(\Delta^{-1})\mathbf{u}\cdot\mathbf{\nabla}]\xi = \mathbf{\nabla}A\xi, \quad (\text{D20})$$

in a weak sense [44], which establishes equation (D16). It follows from (D15) and (D16) that

$$\tilde{\mu}_{jk}^1 = \langle \mathbf{M}\mathbf{g}_j \cdot \mathbf{g}_k \rangle = \langle \mathbf{M}\mathbf{\nabla}g_j \cdot \mathbf{\nabla}g_k \rangle = \langle \mathbf{\nabla}Mg_j \cdot \mathbf{\nabla}g_k \rangle = \langle Mg_j, g_k \rangle_{1,2} = \mu_{jk}^1 \quad (\text{D21})$$

$$\tilde{\mu}_{jk}^2 = \langle \mathbf{M}^2\mathbf{g}_j \cdot \mathbf{g}_k \rangle = \langle \mathbf{M}\mathbf{\nabla}Mg_j \cdot \mathbf{\nabla}g_k \rangle = \langle \mathbf{\nabla}M^2g_j \cdot \mathbf{\nabla}g_k \rangle = \langle M^2g_j, g_k \rangle_{1,2} = \mu_{jk}^2.$$

An inductive argument establishes equation (D17). This concludes our proof of Theorem 5 \square .

We conclude this section with the following corollary of Theorem 5.

Corollary 6 *For each $\xi \in \mathcal{H}^{1,2}$ we have $\nabla \xi \in \mathcal{H}_x$, and conversely, for each $\xi \in \mathcal{H}_x$ there exists unique $\xi \in \mathcal{H}^{1,2}$ such that $\xi = \nabla \xi$. Consequently, by Theorem 5, for every $\xi, \zeta \in \mathcal{H}^{1,2}$ and $\xi, \zeta \in \mathcal{H}_x$ related by $\xi = \nabla \zeta$ and $\zeta = \nabla \xi$ we have*

$$\mu_{\xi\zeta}^n = \tilde{\mu}_{\xi\zeta}^n, \quad n = 0, 1, 2, \dots. \quad (\text{D22})$$

This establishes that the spectral measures $\mu_{\xi\zeta}$ and $\tilde{\mu}_{\xi\zeta}$ are identical,

$$\mu_{\xi\zeta} \equiv \tilde{\mu}_{\xi\zeta}. \quad (\text{D23})$$

Moreover, equation (D22) also holds for the class of space-time periodic fluid velocity fields $\mathbf{u} = \mathbf{u}(\mathbf{x}, t)$ described in [44].

Proof of Corollary 6. The Hilbert spaces $\mathcal{H}^{1,2}$ and \mathcal{H}_x are in one-to-one isometric correspondence [44]. More specifically, for every $\xi \in \mathcal{H}^{1,2}$ we have $\nabla \xi \in \mathcal{H}_x$ satisfying $\|\xi\|_{1,2} = \|\nabla \xi\|$ and $\|A\xi\|_{1,2} = \|\mathbf{A}\nabla \xi\|$. Conversely, for each $\xi \in \mathcal{H}_x$ there exists unique [44] $\xi \in \mathcal{H}^{1,2}$ (up to equivalence class) such that $\xi = \nabla \xi$, $\|\xi\| = \|\xi\|_{1,2}$, and $\|A\xi\| = \|A\xi\|_{1,2}$. By this and Theorem 5 we have equations (D22) and (D23).

The proof of equation (D17) depends only on equations (D15) and (D16), which also hold [44] for the class of space-time periodic fluid velocity fields $\mathbf{u} = \mathbf{u}(\mathbf{x}, t)$ described in [44]. The argument in the previous paragraph above also holds for this time-dependent setting [44]. Therefore, equation (D22) holds for the time-dependent setting as well. This concludes our proof of Corollary 6 \square .

In order to establish equation (D23) for the time-dependent setting associated with operators having unbounded spectra [44], one must first establish Carleman's criterion [1], for example, associated with the Stieltjes or Hamburger moment problems. This requires an involved analysis that is outside of the scope of the current work. Our results in this direction will be published elsewhere.

Appendix E: Discrete setting: Hilbert space of curl-free fields

Here, we provide a matrix formulation for the effective parameter problem discussed in Appendix D 2, which provides discrete versions of the Stieltjes integral representations for \mathfrak{D}^*

shown in equation (19). These integrals involve a discrete spectral measure μ_{jk} analogous to the discrete measure in equation (35). More specifically, we use a discretized version of the cell problem in equation (D2) and (D9), written as $(\varepsilon I + \mathbf{A})\nabla\chi_k = \mathbf{g}_k$, to express the discrete spectral measure μ_{jk} explicitly in terms of the eigenvalues and eigenvectors of a matrix representation \mathbf{A} of the operator $\mathbf{A} = \boldsymbol{\Gamma}\mathbf{H}\boldsymbol{\Gamma}$. We then develop a *projection method* which additionally shows that the discrete measure μ_{jk} is actually determined by the eigenvalues and eigenvectors of a matrix that is much smaller than the matrix \mathbf{A} . This projection method is used in Appendix G to establish the equivalence of the two discrete approaches given in this appendix and Section IV, for the setting where the matrix gradient ∇ is rank-deficient. This equivalence proof establishes, en route, that the common discrete spectral measure can be computed by a method that combines the computational benefits of both approaches.

From the discussion in Section IV, the discrete representation of the projection operator $\boldsymbol{\Gamma} = \nabla(\Delta^{-1})\nabla\cdot$ is given by the symmetric projection matrix $\boldsymbol{\Gamma} = \nabla(\nabla^T\nabla)^{-1}\nabla^T$ satisfying $\boldsymbol{\Gamma}^2 = \boldsymbol{\Gamma}$ and $\boldsymbol{\Gamma}\nabla = \nabla$, where $(\nabla^T\nabla)^{-1}$ is now interpreted as a matrix inversion. We assume here that the matrix ∇ is of full-rank so that $(\nabla^T\nabla)^{-1}$ exists. The rank-deficient case, where the matrix $\nabla^T\nabla$ is singular, is examined in Appendix G. In this way, the integro-differential operator $\mathbf{A} = \boldsymbol{\Gamma}\mathbf{H}\boldsymbol{\Gamma}$ is represented by an antisymmetric matrix $\mathbf{A} = \boldsymbol{\Gamma}\mathbf{H}\boldsymbol{\Gamma}$ satisfying $\mathbf{A}^T = -\mathbf{A}$. In a similar way, the vectors $\mathbf{g}_k = -\boldsymbol{\Gamma}\mathbf{H}\mathbf{e}_k$, $k = 1, \dots, d$, are redefined for this matrix setting. For simplicity, we will not make a notational distinction between the continuum and discrete cases for the vectors \mathbf{g}_k and \mathbf{e}_k as well as the matrix \mathbf{H} , as the context will be clear.

The spectrum of the antisymmetric matrix \mathbf{A} of size N , say, is comprised of eigenvalues v_n , $n = 1, \dots, N$, with corresponding eigenvectors \mathbf{w}_n satisfying $\mathbf{A}\mathbf{w}_n = v_n\mathbf{w}_n$. Since \mathbf{A} is skew-symmetric, the eigenvalues v_n are purely imaginary [25], $v_n = i\lambda_n$ with $\lambda_n \in \mathbb{R}$. Therefore, the matrix $\mathbf{M} = -i\mathbf{A}$ is Hermitian ($\mathbf{M}^\dagger = \mathbf{M}$) and it has the same eigenvectors \mathbf{w}_n as the matrix \mathbf{A} and real eigenvalues given by $\lambda_n = \text{Im } v_n$. The eigenvectors \mathbf{w}_n , $n = 1, \dots, N$, of the Hermitian matrix \mathbf{M} form an orthonormal basis for \mathbb{C}^N [25, 28], i.e., $\mathbf{w}_n^\dagger \mathbf{w}_m = \delta_{nm}$ and for every $\xi \in \mathbb{C}^N$ we have $\xi = \sum_n (\mathbf{w}_n^\dagger \xi) \mathbf{w}_n = (\sum_n \mathbf{w}_n \mathbf{w}_n^\dagger) \xi$. Consequently, defining $\mathcal{Q}_n = \mathbf{w}_n \mathbf{w}_n^\dagger$, $n = 1, \dots, N$, to be the mutually orthogonal Hermitian projection matrices onto the eigenspaces spanned by the \mathbf{w}_n , we have the following analogue of equation (34)

$$\sum_{n=1}^N \mathcal{Q}_n = \mathbf{I}, \quad \mathcal{Q}_n = \mathbf{w}_n \mathbf{w}_n^\dagger, \quad \mathcal{Q}_l \mathcal{Q}_m = \mathcal{Q}_l \delta_{lm}. \quad (\text{E1})$$

With an argument similar to the one in the paragraph following equation (34), one can show

that for all $\xi, \zeta \in \mathbb{C}^N$ and complex-valued polynomials $f(\lambda)$ and $h(\lambda)$, the bilinear functional $\langle f(\mathbf{M})\xi \cdot h(\mathbf{M})\zeta \rangle$ has the integral representation in equation (17), with M substituted by \mathbf{M} and the scalars ξ and ζ replaced by vectors ξ and ζ . Moreover, the complex-valued function $\mu_{\xi\zeta}(\lambda) = \langle Q(\lambda)\xi, \zeta \rangle$ in equation (17) is now given by $\mu_{\xi\zeta}(\lambda) = \langle \mathcal{Q}(\lambda)\xi \cdot \zeta \rangle$, where the associated matrix representation $\mathcal{Q}(\lambda)$ of the projection operator $Q(\lambda)$ and the discrete spectral measure $d\mu_{\xi\zeta}(\lambda)$ are given by the following analogue of equation (35)

$$\mathcal{Q}(\lambda) = \sum_{n: \lambda_n \leq \lambda} \theta(\lambda - \lambda_n) \mathcal{Q}_n, \quad d\mu_{\xi\zeta}(\lambda) = \sum_{n: \lambda_n \leq \lambda} \langle \delta_{\lambda_n}(d\lambda) [\mathcal{Q}_n \xi \cdot \zeta] \rangle. \quad (\text{E2})$$

We are now ready to present the main results of this section, given in the following corollary of Theorem 3.

Corollary 7 Consider the standard eigenvalue problem $\mathbf{M}\mathbf{w}_n = \lambda_n \mathbf{w}_n$ associated with the Hermitian matrix $\mathbf{M} = -i\mathbf{A}$. Let \mathbf{W} be the matrix with columns consisting of the eigenvectors \mathbf{w}_n and Λ be the diagonal matrix with eigenvalues λ_n on its diagonal. The discrete, matrix representations of the bilinear functional formulas for \mathfrak{S}_{jk}^* and \mathfrak{A}_{jk}^* in equation (D4) with \mathbf{H} replaced by \mathbf{A} , as discussed right before equation (D10), are given by

$$\mathfrak{S}_{jk}^* = \varepsilon(\delta_{jk} + \langle \nabla \chi_j \cdot \nabla \chi_k \rangle), \quad \mathfrak{A}_{jk}^* = \langle \mathbf{A} \nabla \chi_j \cdot \nabla \chi_k \rangle, \quad (\text{E3})$$

which is analogous to equation (36). Also, the discrete representation of the resolvent formula for $\nabla \chi_j$ in equation (D9) is given by

$$\nabla \chi_j = \mathbf{W}(\varepsilon I + i\Lambda)^{-1} \mathbf{W}^\dagger \mathbf{g}_j, \quad \mathbf{g}_j = -\Gamma \mathbf{H} \mathbf{e}_j, \quad (\text{E4})$$

which is analogous to equation (37). The discrete representations of the bilinear functional formulas for \mathfrak{S}_{jk}^* and \mathfrak{A}_{jk}^* in (D10) are given by

$$\begin{aligned} \mathfrak{S}_{jk}^* &= \varepsilon(\delta_{jk} + \langle (\varepsilon I + i\Lambda)^{-1} \mathbf{W}^\dagger \mathbf{g}_j \cdot (\varepsilon I + i\Lambda)^{-1} \mathbf{W}^\dagger \mathbf{g}_k \rangle), \\ \mathfrak{A}_{jk}^* &= \langle i\Lambda(\varepsilon I + i\Lambda)^{-1} \mathbf{W}^\dagger \mathbf{g}_j \cdot (\varepsilon I + i\Lambda)^{-1} \mathbf{W}^\dagger \mathbf{g}_k \rangle \end{aligned} \quad (\text{E5})$$

which are analogous to those in equation (38). Consequently, the formulas for \mathfrak{S}_{jk}^* and \mathfrak{A}_{jk}^* in (E5) have the following series representations

$$\mathfrak{S}_{jk}^*/\varepsilon - \delta_{jk} = \sum_{n=1}^N \frac{\operatorname{Re}[\overline{(\mathbf{w}_n^\dagger \mathbf{g}_j)}(\mathbf{w}_n^\dagger \mathbf{g}_k)]}{\varepsilon^2 + \lambda_n^2}, \quad \mathfrak{A}_{jk}^* = \sum_{n=1}^N \frac{\lambda_n \operatorname{Im}[\overline{(\mathbf{w}_n^\dagger \mathbf{g}_j)}(\mathbf{w}_n^\dagger \mathbf{g}_k)]}{\varepsilon^2 + \lambda_n^2}, \quad (\text{E6})$$

which is analogous to equation (39). Finally, recalling the projection matrix $\mathcal{Q}_n = \mathbf{w}_n \mathbf{w}_n^\dagger$ in (E1), we have

$$\overline{(\mathbf{w}_n^\dagger \mathbf{g}_j)} (\mathbf{w}_n^\dagger \mathbf{g}_k) = \mathcal{Q}_n \mathbf{g}_j \cdot \mathbf{g}_k, \quad (\text{E7})$$

which is analogous to equation (40). It follows from equation (E7) that the series representations for \mathfrak{S}_{jk}^* and \mathfrak{A}_{jk}^* in (E6) have the Stieltjes integral representations in equation (19), involving the discrete spectral measure μ_{jk} in (E2) with $\xi = \mathbf{g}_j = -\Gamma \mathbf{H} \mathbf{e}_j$ and $\zeta = \mathbf{g}_k = -\Gamma \mathbf{H} \mathbf{e}_k$.

Proof of Corollary 7. Equation (E3) follows from the discrete version of (D4) and $\Gamma \nabla = \nabla$ so $\langle \mathbf{H} \nabla \chi_j \cdot \nabla \chi_k \rangle = \langle \mathbf{A} \nabla \chi_j \cdot \nabla \chi_k \rangle$. Consider the spectral decomposition $\mathbf{M} = \mathbf{W} \Lambda \mathbf{W}^\dagger$ of the Hermitian matrix $\mathbf{M} = -\imath \mathbf{A}$ involving the real eigenvalues λ_n comprising the main diagonal of the diagonal matrix Λ and the eigenvectors \mathbf{w}_n comprising the columns of the unitary matrix \mathbf{W} satisfying $\mathbf{W}^\dagger \mathbf{W} = \mathbf{W} \mathbf{W}^\dagger = \mathbf{I}$ [25]. Equation (E4) follows from this spectral decomposition of $\mathbf{A} = \imath \mathbf{M}$, the discrete version of the resolvent formula in equation (D9) written as $\nabla \chi_j = (\varepsilon \mathbf{I} + \mathbf{A})^{-1} \mathbf{g}_j$, the fact that \mathbf{W} is unitary satisfying $\mathbf{W}^\dagger = \mathbf{W}^{-1}$, and elementary properties of matrix inversion [25]. Substituting the resolvent formula for $\nabla \chi_j$ in (E4) into equation (E3) and using $\mathbf{W}^\dagger = \mathbf{W}^{-1}$ yields equation (E5). The quadratic form $\mathbf{W}^\dagger \mathbf{g}_j \cdot \mathbf{W}^\dagger \mathbf{g}_k$ arising in (E5) can be written in terms of the projection matrices $\mathcal{Q}_n = \mathbf{w}_n \mathbf{w}_n^\dagger$ defined in (E1) as follows

$$\mathbf{W}^\dagger \mathbf{g}_j \cdot \mathbf{W}^\dagger \mathbf{g}_k = \sum_{n=1}^N \overline{(\mathbf{w}_n^\dagger \mathbf{g}_j)} (\mathbf{w}_n^\dagger \mathbf{g}_k) = \sum_{n=1}^N \mathcal{Q}_n \mathbf{g}_j \cdot \mathbf{g}_k. \quad (\text{E8})$$

Exactly as in Theorem 3 we have equation (E6), which can be written in terms of the integral representations in equation (19) involving the discrete spectral measure $d\mu_{jk}(\lambda)$ in equation (E2) with $\xi = \mathbf{g}_j = -\Gamma \mathbf{H} \mathbf{e}_j$ and $\zeta = \mathbf{g}_k = -\Gamma \mathbf{H} \mathbf{e}_k$. This concludes our proof of Corollary 7 \square .

We conclude this section with the development of a *projection method* that is used in the proof of Theorem 10 below. This method shows that the presence of the projection matrix Γ in the operator $\Gamma \mathbf{H} \Gamma$ and $\mathbf{g}_k = -\Gamma \mathbf{H} \mathbf{e}_k$ projects out contributions of the null space of Γ in the series representation for \mathfrak{D}^* in (E6). This is reminiscent of problems encountered for many elliptic equations on periodic domains, where the analysis requires a deficient dimension to be projected out [7]. Theorem 10 establishes that the discrete framework developed in

Section IV and this section yield equivalent Stieltjes integral representations for the effective diffusivity matrix \mathfrak{D}^* , involving a discrete spectral measure, and also generalizes this result to the setting where the matrix ∇ is rank-deficient. The proof of Theorem 10 demonstrates that the common discrete spectral measure can be computed by a method that combines the computational benefits of both approaches. This, in turn, is used in our numerical computations of Stieltjes integral representations of \mathfrak{D}^* in Section V.

Theorem 8 (Projection Method) *The real-symmetric projection matrix Γ of size N has eigenvalues satisfying $\gamma_n = 0, 1$, hence the spectral decomposition*

$$\Gamma = \mathbf{P}\mathbf{G}\mathbf{P}^T, \quad \mathbf{G} = \text{diag}(\mathbf{0}_{N_0}, \mathbf{1}_{N_1}), \quad \mathbf{P} = [\mathbf{P}_0 \ \mathbf{P}_1]. \quad (\text{E9})$$

Here, $\mathbf{0}_{N_0}$ and $\mathbf{1}_{N_1}$ are vectors of zeros and ones with N_0 and N_1 components, respectively, where $N = N_0 + N_1$. Moreover, the columns comprising the $N \times N_0$ matrix \mathbf{P}_0 and the $N \times N_1$ matrix \mathbf{P}_1 are orthonormal eigenvectors that span the null space and range of Γ , respectively. Consequently, the matrix Γ can be written as

$$\Gamma = \mathbf{P}_1 \mathbf{P}_1^T. \quad (\text{E10})$$

Consider the spectral composition of the antisymmetric matrix $\mathbf{P}_1^T \mathbf{H} \mathbf{P}_1$ of size N_1 ,

$$\mathbf{P}_1^T \mathbf{H} \mathbf{P}_1 = i \mathbf{R}_{11} \Lambda_{11} \mathbf{R}_{11}^\dagger, \quad (\text{E11})$$

where \mathbf{R}_{11} is a unitary matrix, $\mathbf{R}_{11}^\dagger \mathbf{R}_{11} = \mathbf{R}_{11} \mathbf{R}_{11}^\dagger = \mathbf{I}_{11}$, Λ_{11} is a real-valued diagonal matrix, and \mathbf{I}_{11} is the identity matrix of size $N_1 \times N_1$. It follows that the matrix $\mathbf{A} = i\Gamma \mathbf{H} \Gamma$ has the spectral decomposition

$$\mathbf{A} = i \mathbf{W} \Lambda \mathbf{W}^\dagger, \quad \mathbf{W} = [\mathbf{P}_0 \ \mathbf{P}_1 \mathbf{R}_{11}], \quad \Lambda = \text{diag}(\mathbf{0}_{00} \ \Lambda_{11}). \quad (\text{E12})$$

Equations (E10) and (E12), and the mutual orthogonality of the matrices \mathbf{P}_0 and \mathbf{P}_1 yield

$$\mathbf{W}^\dagger \mathbf{g}_k = \mathbf{W}^\dagger \Gamma \mathbf{H} \mathbf{e}_k = [\mathbf{0}_0 \ \mathbf{P}_1 \mathbf{R}_{11}]^\dagger \mathbf{H} \mathbf{e}_k, \quad (\text{E13})$$

where $\mathbf{0}_0$ is a matrix of zeros of size $N \times N_0$. Consequently, equation (E8) can be written

$$\mathbf{W}^\dagger \mathbf{g}_j \cdot \mathbf{W}^\dagger \mathbf{g}_k = (\mathbf{P}_1 \mathbf{R}_{11})^\dagger \mathbf{H} \mathbf{e}_k \cdot (\mathbf{P}_1 \mathbf{R}_{11})^\dagger \mathbf{H} \mathbf{e}_k. \quad (\text{E14})$$

Moreover, the spectral weights in equation (E8) associated with $\gamma_n = 0$ are identically zero $[\mathcal{Q}_n \mathbf{g}_j \cdot \mathbf{g}_k] = 0$.

Proof of Theorem 8. Using the spectral decomposition $\Gamma = \mathbf{P}\Gamma\mathbf{P}^T$ in (E9), we write the matrix $\mathbf{A} = \Gamma\mathbf{H}\Gamma$ as $\mathbf{A} = \mathbf{P}[\mathbf{G}(\mathbf{P}^T\mathbf{H}\mathbf{P})\mathbf{G}]\mathbf{P}^T = \mathbf{P}\text{diag}(\mathbf{O}_{00} \mathbf{P}_1^T\mathbf{H}\mathbf{P}_1)\mathbf{P}^T$, where \mathbf{O}_{00} is a matrix of zeros of size $N_0 \times N_0$. Due to the skew-symmetry of \mathbf{H} , the $N_1 \times N_1$ matrix $\mathbf{P}_1^T\mathbf{H}\mathbf{P}_1$ is also skew-symmetric. Consequently, it has the spectral decomposition in equation (E11), hence $\mathbf{A} = \mathbf{P}\text{diag}(\mathbf{O}_{00} \imath\mathbf{R}_{11}\Lambda_{11}\mathbf{R}_{11}^\dagger)\mathbf{P}^T$. Writing this in block matrix form [42] and multiplying yields equation (E12). Equations (E10) and (E12), and the mutual orthogonality of the matrices \mathbf{P}_0 and \mathbf{P}_1 yield equation (E13). This concludes our proof of Theorem 8 \square .

Appendix F: Discrete equivalence of the effective parameter problems

In Section III, we provided Stieltjes integral representations for the symmetric \mathfrak{S}^* and antisymmetric \mathfrak{A}^* parts of the effective diffusivity matrix \mathfrak{D}^* , associated with an incompressible fluid velocity field. A discrete version of this mathematical framework was formulated in Section IV. An alternate approach to the effective parameter problem was formulated in Appendix D, and its discrete version was formulated in Appendix E. In this section, we demonstrate that the discrete versions of these effective parameter problems yield equivalent spectral representations of \mathfrak{D}^* when the matrix ∇ is of full-rank, as in the case of Dirichlet boundary conditions, so that the matrix Laplacian is invertible. In Appendix G, this result is extended to the setting where ∇ is rank-deficient, as in the case of periodic boundary conditions.

Let $\nabla = \mathbf{U}\Sigma\mathbf{V}^T$ be the singular value decomposition (SVD) of the matrix ∇ of size $N \times K$, where $K = L^d$ and $N = Kd$. Here, $\Sigma = \text{diag}(\sigma_1, \dots, \sigma_K)$, where $0 \leq \sigma_1 \leq \dots \leq \sigma_K$, and the matrices \mathbf{U} and \mathbf{V} are of size $N \times K$ and $K \times K$, respectively, and satisfy [14]

$$\mathbf{U}^T\mathbf{U} = \mathbf{I}, \quad \mathbf{V}^T\mathbf{V} = \mathbf{V}\mathbf{V}^T = \mathbf{I}, \quad (\text{F1})$$

where \mathbf{I} is the $K \times K$ identity matrix. The columns of \mathbf{U} are called left singular vectors, the columns of \mathbf{V} are called right singular vectors, and the σ_i are called singular values.

It follows from $\nabla = \mathbf{U}\Sigma\mathbf{V}^T$ and equation (F1) that the spectral decomposition of the negative matrix Laplacian $\nabla^T\nabla$ is given by $\nabla^T\nabla = \mathbf{V}\Sigma^2\mathbf{V}^T$ [14]. We assume that ∇ is of full-rank so that $\sigma_i > 0$ for all $i = 1, \dots, K$. This implies that Σ^{-1} exists so that the matrix Laplacian is invertible. In this case, it follows from $\nabla = \mathbf{U}\Sigma\mathbf{V}^T$ and equation (F1) that the

projection matrix $\Gamma = \nabla(\nabla^T \nabla)^{-1} \nabla^T$ is given by

$$\Gamma = \mathbf{U}\mathbf{U}^T, \quad (\text{F2})$$

which is a $N \times N$ symmetric projection matrix satisfying $\Gamma^2 = \Gamma$ and $\Gamma\nabla = \nabla$. A key property of the SVD of the *full-rank* matrix ∇ is that its range is spanned by the columns of \mathbf{U} [14], hence $\Gamma = \mathbf{U}\mathbf{U}^T$ projects subspaces of \mathbb{R}^N onto the range of ∇ .

From equations (F1) and (F2), we can write the eigenvalue problem $-\imath\Gamma\mathsf{H}\Gamma\mathbf{w}_n = \lambda_n\mathbf{w}_n$ discussed in Appendix E as

$$[-\imath\mathbf{U}^T\mathsf{H}\mathbf{U}][\mathbf{U}^T\mathbf{w}_n] = \lambda_n[\mathbf{U}^T\mathbf{w}_n]. \quad (\text{F3})$$

Now consider the generalized eigenvalue problem $-\imath\nabla^T\mathsf{H}\nabla\mathbf{z}_n = \alpha_n\nabla^T\nabla\mathbf{z}_n$ discussed in Section IV and recall that $\nabla = \mathbf{U}\Sigma\mathbf{V}^T$ and $\nabla^T\nabla = \mathbf{V}\Sigma^2\mathbf{V}^T$. Since Σ is invertible, by equation (F1) we can write this generalized eigenvalue problem as the following standard eigenvalue problem

$$[-\imath\mathbf{U}^T\mathsf{H}\mathbf{U}][\Sigma\mathbf{V}^T\mathbf{z}_n] = \alpha_n[\Sigma\mathbf{V}^T\mathbf{z}_n]. \quad (\text{F4})$$

Comparing the formulas in equations (F3) and (F4) indicates that spectrum associated with each of these eigenvalue problems is identical, $\alpha_n = \lambda_n$, and that the eigenvectors are related by $\mathbf{U}^T\mathbf{w}_n = \Sigma\mathbf{V}^T\mathbf{z}_n$. Since Γ is a projection matrix, $\Gamma^2 = \Gamma$, the eigenvalue problem $\Gamma\mathsf{H}\Gamma\mathbf{w}_n = \imath\lambda_n\mathbf{w}_n$ can be written as $\Gamma\mathsf{H}\Gamma[\Gamma\mathbf{w}_n] = \imath\lambda_n[\Gamma\mathbf{w}_n]$, which implies that $\Gamma\mathbf{w}_n = \mathbf{w}_n$. Consequently, applying the matrix \mathbf{U} to both sides of the formula $\mathbf{U}^T\mathbf{w}_n = \Sigma\mathbf{V}^T\mathbf{z}_n$ and recalling that $\Gamma = \mathbf{U}\mathbf{U}^T$ and $\nabla = \mathbf{U}\Sigma\mathbf{V}^T$ we have

$$\mathbf{w}_n = \nabla\mathbf{z}_n. \quad (\text{F5})$$

In the following lemma, we make precise the correspondence between the standard eigenvalue problem $-\imath\Gamma\mathsf{H}\Gamma\mathbf{w}_n = \lambda_n\mathbf{w}_n$ and the generalized eigenvalue problem $-\imath\nabla^T\mathsf{H}\nabla\mathbf{z}_n = \alpha_n\nabla^T\nabla\mathbf{z}_n$, as well as the associated spectral measures in equations (E2) and (35), respectively.

Lemma 9 *Consider the standard eigenvalue problem and the generalized eigenvalue problem given, respectively, in equations (F6) and (F7) below*

$$-\imath\Gamma\mathsf{H}\Gamma\mathbf{w}_n = \lambda_n\mathbf{w}_n, \quad (\text{F6})$$

$$-\imath\nabla^T\mathsf{H}\nabla\mathbf{z}_n = \lambda_n\nabla^T\nabla\mathbf{z}_n. \quad (\text{F7})$$

Let $\nabla = \mathbf{U}\Sigma\mathbf{V}^T$ be the SVD of the matrix ∇ , which we assume to be of full-rank. Then equation (F6) implies and is implied by equation (F7), with \mathbf{w}_n and \mathbf{z}_n related as in equation (F5). This implies that the spectrum associated with each of these eigenvalue problems is identical. Moreover, the spectral weights in equations (E8) and (40) are identical; specifically

$$\mathcal{Q}_n \Gamma \mathbf{H} \mathbf{e}_j \cdot \Gamma \mathbf{H} \mathbf{e}_k = \nabla \mathbf{Q}_n [\nabla^T \nabla]^{-1} \mathbf{u}_j \cdot \nabla [\nabla^T \nabla]^{-1} \mathbf{u}_k. \quad (\text{F8})$$

This, in turn, implies that the associated spectral measures in equations (E2) and (35) are identical.

Proof of Lemma 9

Recall that $\nabla = \mathbf{U}\Sigma\mathbf{V}^T$, $\nabla^T \nabla = \mathbf{V}\Sigma^2\mathbf{V}^T$, and $\Gamma = \mathbf{U}\mathbf{U}^T$, where Σ is invertible, and the matrices \mathbf{V} and \mathbf{U} satisfy equation (F1). First consider equation (F6) written as in equation (F3), $[-i\mathbf{U}^T \mathbf{H} \mathbf{U}] [\mathbf{U}^T \mathbf{w}_n] = \lambda_n [\mathbf{U}^T \mathbf{w}_n]$. Since the matrix Σ is invertible and $\mathbf{V}^T \mathbf{V} = \mathbf{I}$, we can rewrite equation (F3) as

$$\mathbf{V}\Sigma[-i\mathbf{U}^T \mathbf{H} \mathbf{U}] (\Sigma\mathbf{V}^T) (\mathbf{V}\Sigma^{-1}) [\mathbf{U}^T \mathbf{w}_n] = \lambda_n (\mathbf{V}\Sigma^2\mathbf{V}^T) (\mathbf{V}\Sigma^{-1}) [\mathbf{U}^T \mathbf{w}_n], \quad (\text{F9})$$

which is precisely equation (F7) written in terms of $\nabla = \mathbf{U}\Sigma\mathbf{V}^T$ with $\mathbf{z}_n = \mathbf{V}\Sigma^{-1}\mathbf{U}^T \mathbf{w}_n$. This formula for \mathbf{z}_n , equation (F1), and the formula $\Gamma \mathbf{w}_n = \mathbf{w}_n$ above equation (F5) imply that $\mathbf{w}_n = \mathbf{U}\Sigma\mathbf{V}^T \mathbf{z}_n = \nabla \mathbf{z}_n$, which is the formula in (F5). Now consider equation (F7) written as in (F4), $[-i\mathbf{U}^T \mathbf{H} \mathbf{U}] [\Sigma\mathbf{V}^T \mathbf{z}_n] = \lambda_n [\Sigma\mathbf{V}^T \mathbf{z}_n]$. Since $\mathbf{U}^T \mathbf{U} = \mathbf{I}$, we can rewrite equation (F4) as

$$\mathbf{U}[-i\mathbf{U}^T \mathbf{H} \mathbf{U}] (\mathbf{U}^T \mathbf{U}) [\Sigma\mathbf{V}^T \mathbf{z}_n] = \lambda_n \mathbf{U} [\Sigma\mathbf{V}^T \mathbf{z}_n], \quad (\text{F10})$$

which is precisely (F6) written in terms of $\Gamma = \mathbf{U}\mathbf{U}^T$ with $\mathbf{w}_n = \mathbf{U}\Sigma\mathbf{V}^T \mathbf{z}_n = \nabla \mathbf{z}_n$.

We now establish equation (F8). From the formula $\mathbf{u} = \nabla \cdot \mathbf{H}$ in (28), for the continuum setting, we have that $u_j = (\nabla \cdot \mathbf{H}) \cdot \mathbf{e}_j = \nabla \cdot (\mathbf{H} \mathbf{e}_j)$. Since $\nabla = \mathbf{U}\Sigma\mathbf{V}^T$, the discrete version of this formula is given by

$$\mathbf{u}_j = -\nabla^T \mathbf{H} \mathbf{e}_j = -\mathbf{V}\Sigma\mathbf{U}^T \mathbf{H} \mathbf{e}_j. \quad (\text{F11})$$

From $\nabla = \mathbf{U}\Sigma\mathbf{V}^T$ and $(\nabla^T \nabla)^{-1} = \mathbf{V}\Sigma^{-2}\mathbf{V}^T$ we have $\nabla(\nabla^T \nabla)^{-1} = \mathbf{U}\Sigma^{-1}\mathbf{V}^T$. Consequently, $\Gamma = \mathbf{U}\mathbf{U}^T$, and equations (F1) and (F11), yield $\nabla(\nabla^T \nabla)^{-1} \mathbf{u}_j = -\Gamma \mathbf{H} \mathbf{e}_j$. Equation (F8) now follows from the formula $\mathbf{w}_n = \nabla \mathbf{z}_n$ in (F5)

$$\begin{aligned} \mathbf{w}_n \mathbf{w}_n^\dagger \nabla(\nabla^T \nabla)^{-1} \mathbf{u}_j \cdot \nabla(\nabla^T \nabla)^{-1} \mathbf{u}_k &= [(\nabla^T \nabla)^{-1} \nabla^T \mathbf{w}_n] [(\nabla^T \nabla)^{-1} \nabla^T \mathbf{w}_n]^\dagger \mathbf{u}_j \cdot \mathbf{u}_k \\ &= [(\nabla^T \nabla)^{-1} \nabla^T \nabla \mathbf{z}_n] [(\nabla^T \nabla)^{-1} \nabla^T \nabla \mathbf{z}_n]^\dagger \mathbf{u}_j \cdot \mathbf{u}_k \\ &= \mathbf{z}_n \mathbf{z}_n^\dagger \mathbf{u}_j \cdot \mathbf{u}_k, \end{aligned} \quad (\text{F12})$$

where we have used that the inverse of a symmetric matrix is also symmetric [25]. The equivalence of equations (F8) and (F12) now follows from equations (E1), (34), and (40). This concludes our proof of Lemma 9 \square .

We conclude this section with a discussion regarding numerical computations of the effective diffusivity matrix \mathfrak{D}^* . The approach discussed in this section and the projection method discussed in Theorem 8 demonstrate that a hybrid of these two approaches leads to the most efficient algorithm for numerical computations of spectral representations for \mathfrak{D}^* — combining the computational advantages of both the methods discussed in Appendix E and Section IV. More specifically, in the full rank setting, the spectral measure underlying the discrete integral representation for \mathfrak{D}^* was calculated in Appendix E in terms of the *standard* eigenvalue problem $-\imath\Gamma\mathsf{H}\Gamma\mathbf{w}_m = \lambda_n\mathbf{w}_n$, where the matrix $-\imath\Gamma\mathsf{H}\Gamma$ is of size $N \times N$. In Section IV, \mathfrak{D}^* was calculated in terms of the *generalized* eigenvalue problem $-\imath\nabla^T\mathsf{H}\nabla\mathbf{z}_n = \lambda_n\nabla^T\nabla\mathbf{z}_n$, involving the $K \times K$ matrices $-\imath\nabla^T\mathsf{H}\nabla$ and $\nabla^T\nabla$. Since $\nabla^T = (\nabla_1^T, \dots, \nabla_d^T)$ is of size $K \times N$ we have that $K = N/d < N$. However, the generalized eigenvalue problem is more computationally intensive than the standard eigenvalue problem [47]. For the case of randomly perturbed flows, many statistical iterations are necessary to compute \mathfrak{D}^* and the efficiency of the numerical algorithm is key. Neither of the methods discussed in Appendix E and Section IV are optimal.

The projection method developed in Theorem 8 demonstrates that, by first computing the standard eigenvalue decomposition of the non-random matrix Γ , the spectral statistics of the eigenvalue problem $-\imath\Gamma\mathsf{H}\Gamma\mathbf{w}_n = \lambda_n\mathbf{w}_n$ can then be obtained by repeatedly computing the standard eigenvalue decomposition of smaller matrices. They are of size $K \times K$ by equations (E10)–(E12) and (F2). We emphasize that in the setting of full-rank ∇ , the parameter K in this section and N_1 in Theorem 8 both denote the rank of the matrix Γ , i.e., $K = N_1$. Note, computing the matrix $\Gamma = \nabla(\nabla^T\nabla)^{-1}\nabla^T$ itself involves the cost of numerically solving N linear systems of size $K \times K$. Alternatively, the proof of Lemma 9 illustrates that by first computing the SVD of the matrix gradient, $\nabla = \mathbf{U}\Sigma\mathbf{V}^T$, the spectral statistics of the generalized eigenvalue problem $-\imath\nabla^T\mathsf{H}\nabla\mathbf{z}_n = \lambda_n\nabla^T\nabla\mathbf{z}_n$ can then be obtained by repeatedly computing the *standard* eigenvalue decomposition of the matrix $-\imath\mathbf{U}^T\mathsf{H}\mathbf{U}$ which is of size $K \times K$. When N is large, these equivalent methods are more numerically efficient than the other approaches discussed in Appendix E and Section IV.

In Appendix G, we generalize Lemma 9 to the case where ∇ is rank-deficient with rank

K_1 satisfying $K_1 < K$. Our analysis demonstrates that the two formulations discussed in Appendix E and Section IV yield equivalent spectral representations of the effective diffusivity matrix \mathfrak{D}^* in this rank-deficient setting. Moreover, en route, a more efficient numerical algorithm for computations of \mathfrak{D}^* is revealed. More specifically, we demonstrate by first computing the SVD of the matrix gradient, \mathfrak{D}^* can be computed via a *standard* eigenvalue problem for matrices of size $K_1 \times K_1$. Consequently, the rank deficiency of the problem actually increases the numerical efficiency of computations.

Appendix G: Rank deficiency and a unifying standard eigenvalue problem

In Section IV and Appendix E we provided two discrete, matrix formulations of the effective parameter problem for advection enhanced diffusion, which led to discrete Stieltjes integral representations for the effective diffusivity matrix \mathfrak{D}^* involving spectral measures of Hermitian matrices. These two formulations assume that the $N \times K$ matrix ∇ is of full-rank K so that the negative matrix Laplacian $\nabla^T \nabla$ is invertible. Lemma 9 of Appendix F shows that, given this condition, the two formulations yield equivalent spectral representations of \mathfrak{D}^* . This analysis also demonstrates that a hybrid of the two formulations leads to a numerical algorithm for computing \mathfrak{D}^* that is more efficient than the numerical algorithms for either approach. In this section, we generalize Lemma 9 to the case where ∇ is rank-deficient, with rank K_1 satisfying $K_1 < K$. We demonstrate that the two formulations are equivalent in this rank-deficient setting and we also derive an efficient hybrid numerical algorithm for computations of \mathfrak{D}^* . This framework is used in Section V to compute \mathfrak{D}^* for periodic flows, for which the matrix ∇ with periodic boundary conditions is rank-deficient.

Toward this goal, let $\nabla = \mathbf{U}\Sigma\mathbf{V}^T$ be the SVD of the matrix gradient ∇ of size $N \times K$, introduced in Section IV and Appendix F. We assume that ∇ is rank deficient so that $\nabla^T \nabla = \mathbf{V}\Sigma^2\mathbf{V}^T$ is singular, with K_1 non-zero eigenvalues and $K_0 = K - K_1$ zero eigenvalues, and write

$$\mathbf{U} = [\mathbf{U}_0 \ \mathbf{U}_1], \quad \Sigma = \text{diag}(\mathbf{O}_{00}, \Sigma_1), \quad \mathbf{V} = [\mathbf{V}_0 \ \mathbf{V}_1]. \quad (\text{G1})$$

Here, we denote \mathbf{O}_{ab} , $a, b = 0, 1$, to be matrices of zeros of size $K_a \times K_b$, \mathbf{U}_a is of size $N \times K_a$, \mathbf{V}_a is $K \times K_a$, and Σ_1 is a $K_1 \times K_1$ diagonal, *invertible* matrix. By equation (F1) the matrices \mathbf{U}_1 and \mathbf{V}_1 satisfy $\mathbf{U}_1^T \mathbf{U}_1 = \mathbf{I}_1$ and $\mathbf{V}_1^T \mathbf{V}_1 = \mathbf{I}_1$, where \mathbf{I}_1 is the $K_1 \times K_1$ identity matrix, but

$\mathbf{V}_1\mathbf{V}_1^T \neq \mathbf{I}$. Due to the blocks of zeros in the matrix Σ in equation (G1), we can write the matrix gradient as $\nabla = \mathbf{U}_1\Sigma_1\mathbf{V}_1^T$ and the negative matrix Laplacian as $\nabla^T\nabla = \mathbf{V}_1\Sigma_1^2\mathbf{V}_1^T$. An important property of the SVD of the matrix ∇ is that its null space is spanned by the columns of \mathbf{V}_0 and its range is spanned by the columns of \mathbf{U}_1 [14]. We emphasize that in the setting where ∇ is full-rank, we have $\mathbf{U}_1 = \mathbf{U}$, $\Sigma_1 = \Sigma$, and $\mathbf{V}_1 = \mathbf{V}$ satisfies $\mathbf{V}_1\mathbf{V}_1^T = \mathbf{V}_1^T\mathbf{V}_1 = \mathbf{I}$.

Consider the cell problem in equation (4) written, via (28) and $[\nabla \cdot \mathbf{H}] \cdot \nabla \varphi = \nabla \cdot [\mathbf{H} \nabla \varphi]$, as $\nabla \cdot \mathbf{H} \nabla \chi_j + \varepsilon \Delta \chi_j = -u_j$. Discretizing this formula yields (see the discussion following equation (29) for details regarding the discretization of these differential operators etc.),

$$\nabla^T \mathbf{H} \nabla \chi_j + \varepsilon \nabla^T \nabla \chi_j = \mathbf{u}_j, \quad (\text{G2})$$

where \mathbf{u}_j is the discrete, vector representation of the j th component of the fluid velocity field u_j , and similarly for χ_j . Substituting the formula for \mathbf{u}_j in (G2) into the discrete version $\mathfrak{D}_{jk}^* = \varepsilon \delta_{jk} + \langle \mathbf{u}_j \cdot \chi_k \rangle$ of equation (3) yields

$$\mathfrak{D}_{jk}^* = \mathfrak{S}_{jk}^* + \mathfrak{A}_{jk}^*, \quad \mathfrak{S}_{jk}^* = \varepsilon(\delta_{jk} + \langle \nabla \chi_j \cdot \nabla \chi_k \rangle), \quad \mathfrak{A}_{jk}^* = \langle \nabla^T \mathbf{H} \nabla \chi_j \cdot \chi_k \rangle, \quad (\text{G3})$$

where, as before, $\mathfrak{S}_{kj}^* = \mathfrak{S}_{jk}^*$ and $\mathfrak{A}_{kj}^* = -\mathfrak{A}_{jk}^*$. We are now ready to state the key result of this Appendix.

Theorem 10 *Let the matrix gradient ∇ be rank-deficient and let $\nabla = \mathbf{U}_1\Sigma_1\mathbf{V}_1^T$ be its SVD. Also, let $\mathbf{U}_1^T \mathbf{H} \mathbf{U}_1 = i\mathbf{R}_1 \Lambda_1 \mathbf{R}_1^\dagger$ be the spectral decomposition of the antisymmetric matrix $\mathbf{U}_1^T \mathbf{H} \mathbf{U}_1$. Consider the discrete formulation of the effective parameter problem developed in Section IV. We have the following generalization of equation (34)*

$$\sum_{n=1}^{K_1} \mathbf{Q}_n^1 = \mathbf{V}_1\mathbf{V}_1^T, \quad \mathbf{Q}_n^1 = \mathbf{z}_n^1 [\nabla \mathbf{z}_n^1]^\dagger \nabla, \quad \mathbf{Q}_l^1 \mathbf{Q}_m^1 = \mathbf{Q}_l^1 \delta_{lm}, \quad (\text{G4})$$

where the matrices \mathbf{Q}_n^1 , $n = 1, \dots, K_1$, are self-adjoint with respect to the discrete inner-product $\langle \cdot, \cdot \rangle_{1,2}$ defined by $\langle \boldsymbol{\xi}, \boldsymbol{\zeta} \rangle_{1,2} = \langle \nabla \boldsymbol{\xi} \cdot \nabla \boldsymbol{\zeta} \rangle$, i.e., $\langle \mathbf{Q}_n^1 \boldsymbol{\xi}, \boldsymbol{\zeta} \rangle_{1,2} = \langle \boldsymbol{\xi}, \mathbf{Q}_n^1 \boldsymbol{\zeta} \rangle_{1,2}$ for $\boldsymbol{\xi}, \boldsymbol{\zeta} \in \mathbb{C}^{K_1}$. Moreover, the generalization of the resolvent formula $\chi_j = \mathbf{Z}(\varepsilon \mathbf{I} + i\Lambda)^{-1} \mathbf{Z}^\dagger \mathbf{u}_j$ in equation (37) is given by

$$\mathbf{V}_1^T \chi_j = \mathbf{V}_1^T \mathbf{Z}_1 (\varepsilon \mathbf{I}_1 + i\Lambda_1)^{-1} \mathbf{Z}_1^\dagger \mathbf{u}_j, \quad \mathbf{Z}_1 = \mathbf{V}_1 \Sigma_1^{-1} \mathbf{R}_1. \quad (\text{G5})$$

Now consider the discrete formulation of the effective parameter problem developed in Appendix E. Let $\Gamma_1 \mathbf{H} \Gamma_1 = i\mathbf{W}_1 \tilde{\Lambda} \mathbf{W}_1^\dagger$ be the spectral decomposition of the antisymmetric matrix

$\Gamma_1 \mathsf{H} \Gamma_1$, where $\Gamma_1 = \mathbf{U}_1 \mathbf{U}_1^T$, $\tilde{\Lambda}$ is a diagonal real-valued matrix with $\tilde{\lambda}_n^1$, $n = 1, \dots, N$, on its diagonal, and W_1 is a unitary matrix with columns \mathbf{w}_n^1 . Then, equations (E1) and (E2) hold with \mathcal{Q}_n and λ_n replaced by $\mathcal{Q}_n^1 = [\mathbf{w}_n^1][\mathbf{w}_n^1]^\dagger$ and $\tilde{\lambda}_n^1$. Also, the resolvent formula in equation (E4) holds with W replaced by W_1 and Λ replaced by $\tilde{\Lambda}$.

These two discrete formulations of the effective parameter problem are related as follows. The diagonal eigenvalue matrices $\tilde{\Lambda}$ and Λ_1 are related by $\tilde{\Lambda} = \text{diag}(\mathsf{O}_{00}, \Lambda_1)$. The eigenvector matrices W_1 and Z_1 are related by the following generalization of equation (F5) (also see (E12))

$$\mathsf{W}_1 = [\mathsf{P}_0 \quad \nabla \mathsf{Z}_1], \quad \nabla \mathsf{Z}_1 = \mathbf{U}_1 \mathbf{R}_1. \quad (\text{G6})$$

where the columns of P_0 are eigenvectors of Γ_1 which span its null space. Moreover, the following formulas generalize equations (E14), (F8), and (F12),

$$\mathsf{W}_1^\dagger \Gamma_1 \mathsf{H} \mathbf{e}_j \cdot \mathsf{W}_1^\dagger \Gamma_1 \mathsf{H} \mathbf{e}_k = [\nabla \mathsf{Z}_1]^\dagger \mathsf{H} \mathbf{e}_j \cdot [\nabla \mathsf{Z}_1]^\dagger \mathsf{H} \mathbf{e}_k = \mathsf{Z}_1^\dagger \mathbf{u}_j \cdot \mathsf{Z}_1^\dagger \mathbf{u}_k. \quad (\text{G7})$$

In this rank-deficient setting, these two approaches both yield discrete Stieltjes integral representations for the functional formulas in (G3) for the symmetric \mathfrak{S}^* and antisymmetric \mathfrak{A}^* parts of the effective diffusivity matrix \mathfrak{D}^* . The two representations are equivalent by the relations discussed above and are given by equation (39), with \mathbf{z}_n and λ_n replaced by $\mathbf{z}_n^1 = \mathsf{V}_1 \Sigma_1^{-1} \mathbf{r}_n^1$ and λ_n^1 , $n = 1, \dots, K_1$, where $(\lambda_n^1, \mathbf{r}_n^1)$ are eigen-pairs of matrix $-\imath \mathbf{U}_1^T \mathsf{H} \mathbf{U}_1$. The results discussed here also hold for the setting where ∇ is of full-rank, and therefore generalize the discrete mathematical frameworks developed in Section IV, Appendix E, and Appendix F.

Proof of Theorem 10. We first work with equation (G2) directly and develop a mathematical framework which parallels the framework of Section IV for the rank-deficient setting. We then transform equation (G2) into a discrete analogue of equation (D9) written as $(\varepsilon \mathsf{I} + \Gamma \mathsf{H} \Gamma) \nabla \chi_j = -\Gamma \mathsf{H} \mathbf{e}_j$, with a suitable generalization of the formula for the matrix Γ in (F2), and develop a mathematical framework which parallels the framework of Appendix E. We then generalize Lemma 9 of Appendix F, establishing the equivalence of these two formulations for the rank-deficient setting and, en route, derive a hybrid numerical algorithm for computing spectral representations of \mathfrak{D}^* which is more efficient than both of the other numerical algorithms.

Since $\Sigma = \text{diag}(\mathbf{O}_{00}, \Sigma_1)$ we have $\nabla = \mathbf{U}_1 \Sigma_1 \mathbf{V}_1^T$ and $\nabla^T \nabla = \mathbf{V}_1 \Sigma_1^2 \mathbf{V}_1^T$, so the cell problem in (G2) can be written $[\mathbf{V}_1 \Sigma_1][\mathbf{U}_1^T \mathbf{H} \mathbf{U}_1][\Sigma_1 \mathbf{V}_1^T] \boldsymbol{\chi}_j + \varepsilon \mathbf{V}_1 \Sigma_1^2 \mathbf{V}_1^T \boldsymbol{\chi}_j = \mathbf{u}_j$. The $K_1 \times K_1$ antisymmetric matrix $\mathbf{U}_1^T \mathbf{H} \mathbf{U}_1$ has the spectral decomposition $\mathbf{U}_1^T \mathbf{H} \mathbf{U}_1 = i \mathbf{R}_1 \Lambda_1 \mathbf{R}_1^\dagger$, where Λ_1 is a diagonal real-valued matrix and \mathbf{R}_1 is a unitary matrix, $\mathbf{R}_1^\dagger \mathbf{R}_1 = \mathbf{R}_1 \mathbf{R}_1^\dagger = \mathbf{I}_1$. Equation (G5) follows from these formulas, which is an analogue of equation (37). The formula $\nabla = \mathbf{U}_1 \Sigma_1 \mathbf{V}_1^T$ and equation (G5), in turn, imply that $\nabla \boldsymbol{\chi}_j = \mathbf{U}_1 \mathbf{R}_1 (\varepsilon \mathbf{I}_1 + i \Lambda_1)^{-1} [\mathbf{V}_1 \Sigma_1^{-1} \mathbf{R}_1]^\dagger \mathbf{u}_j$.

Substituting this formula for $\nabla \boldsymbol{\chi}_j$ into the formula for \mathfrak{S}_{jk}^* in equation (G3) and using $\mathbf{U}_1^T \mathbf{U}_1 = \mathbf{I}_1$ and $\mathbf{R}_1^\dagger \mathbf{R}_1 = \mathbf{I}_1$, yields the functional formula for \mathfrak{S}_{jk}^* in (38) with Λ replaced by Λ_1 and Z replaced by $Z_1 = \mathbf{V}_1 \Sigma_1^{-1} \mathbf{R}_1$. We also have

$$\langle \nabla^T \mathbf{H} \nabla \boldsymbol{\chi}_j \cdot \boldsymbol{\chi}_k \rangle = \langle i [\mathbf{V}_1 \Sigma_1 \mathbf{R}_1] \Lambda_1 [\mathbf{R}_1^\dagger \Sigma_1 \mathbf{V}_1^T] \boldsymbol{\chi}_j \cdot \boldsymbol{\chi}_k \rangle = \langle i [\Sigma_1 \mathbf{R}_1 \Lambda_1 \mathbf{R}_1^\dagger \Sigma_1] \mathbf{V}_1^T \boldsymbol{\chi}_j \cdot \mathbf{V}_1^T \boldsymbol{\chi}_k \rangle. \quad (\text{G8})$$

This formula, $\mathbf{R}_1^\dagger \mathbf{R}_1 = \mathbf{I}_1$, $\Sigma_1^T = \Sigma_1$, and equations (G3) and (G5) yield the functional formula for \mathfrak{A}_{jk}^* in (38) with Λ replaced by Λ_1 and Z replaced by $Z_1 = \mathbf{V}_1 \Sigma_1^{-1} \mathbf{R}_1$. The quadratic form $Z_1^\dagger \mathbf{u}_j \cdot Z_1^\dagger \mathbf{u}_k$ arising in these functional formulas yields equation (42) with \mathbf{z}_n replaced by $\mathbf{z}_n^1 = \mathbf{V}_1 \Sigma_1^{-1} \mathbf{r}_n^1$ and other appropriate notational changes, where \mathbf{r}_n^1 , $n = 1, \dots, K_1$, are the orthonormal eigenvectors of the matrix $\mathbf{U}_1^T \mathbf{H} \mathbf{U}_1$ which comprise the columns of \mathbf{R}_1 . The formula $\mathbf{z}_n^1 = \mathbf{V}_1 \Sigma_1^{-1} \mathbf{r}_n^1$ can be written $\nabla \mathbf{z}_n^1 = \mathbf{U}_1 \mathbf{r}_n^1$. The orthogonality properties of \mathbf{R}_1 and \mathbf{U}_1 then imply that the vectors \mathbf{z}_n^1 satisfy the Sobolev-type orthogonality condition in equation (32), $\nabla \mathbf{z}_n^1 \cdot \nabla \mathbf{z}_m^1 = \delta_{nm}$. Moreover, since $\sum_n r_n^1 [r_n^1]^\dagger = I_1$ we also have equation (G4). It follows that the functional representations of \mathfrak{S}_{jk}^* and \mathfrak{A}_{jk}^* in equation (G3) have the discrete integral representations in equation (39) with \mathbf{z}_n and λ_n are replaced by \mathbf{z}_n^1 and λ_n^1 and $(\lambda_n^1, \mathbf{r}_n^1)$ are eigen-pairs of Hermitian matrix $-i \mathbf{U}_1^T \mathbf{H} \mathbf{U}_1$ of size K_1 . These summations have the same properties as the summations discussed in the proof of Theorem 3 and equations (44) and (45).

We now argue that the mathematical framework developed so far in this proof generalizes the full-rank case in Section IV. Indeed, in the full-rank setting the matrix $\mathbf{V}_1 = \mathbf{V}$ is orthogonal, $\Sigma_1 = \Sigma$ is invertible, and $\mathbf{R}_1 = \mathbf{R}$ is orthogonal, so that the matrix $Z_1 = Z$ defined in (G5) is given by $Z = \mathbf{V} \Sigma^{-1} \mathbf{R}$ and is invertible with $Z^{-1} = \mathbf{R}^\dagger \Sigma \mathbf{V}^T$. Equation (33) is satisfied with $Z^{-\dagger} = \mathbf{V} \Sigma \mathbf{R}$ and $\Lambda = \Lambda_1$ which, in turn, establishes the current rank-deficient setting generalizes the full-rank setting summarized by equations (30)–(42).

We now generalize the mathematical framework developed in Appendix E to the case that the matrix ∇ is rank deficient. Using $\nabla = \mathbf{U}_1 \Sigma_1 \mathbf{V}_1^T$, $\nabla^T \nabla = \mathbf{V}_1 \Sigma_1^2 \mathbf{V}_1^T$, $\mathbf{U}_1^T \mathbf{U}_1 =$

$\mathbf{V}_1^T \mathbf{V}_1 = \mathbf{I}_1$ and the invertibility of the matrix Σ_1 , the cell problem in (G2) can be written as $\mathbf{U}_1 [\mathbf{U}_1^T \mathbf{H} \mathbf{U}_1] [\mathbf{U}_1^T \mathbf{U}_1] [\Sigma_1 \mathbf{V}_1^T] \boldsymbol{\chi}_j + \varepsilon \mathbf{U}_1 \Sigma_1 \mathbf{V}_1^T \boldsymbol{\chi}_j = \mathbf{U}_1 \Sigma_1^{-1} \mathbf{V}_1^T \mathbf{u}_j$. Substituting $\mathbf{u}_j = -\nabla^T \mathbf{H} \mathbf{e}_j$ into this expression yields $(\varepsilon \mathbf{I} + \Gamma_1 \mathbf{H} \Gamma_1) \nabla \boldsymbol{\chi}_j = \mathbf{g}_j^1$, where $\Gamma_1 = \mathbf{U}_1 \mathbf{U}_1^T$ and $\mathbf{g}_j^1 = -\Gamma_1 \mathbf{H} \mathbf{e}_j$ which is analogous to equation (D9). As in Appendix F, the matrix $\Gamma_1 = \mathbf{U}_1 \mathbf{U}_1^T$ projects subspaces of \mathbb{R}^N onto the *range* of ∇ . The antisymmetric matrix $\Gamma_1 \mathbf{H} \Gamma_1$ has the spectral decomposition $\Gamma_1 \mathbf{H} \Gamma_1 = i \mathbf{W}_1 \tilde{\Lambda} \mathbf{W}_1^\dagger$, where $\tilde{\Lambda}$ is a diagonal real-valued matrix and \mathbf{W}_1 is a unitary matrix $\mathbf{W}_1^\dagger \mathbf{W}_1 = \mathbf{W}_1 \mathbf{W}_1^\dagger = \mathbf{I}$, which yields a generalization of (E4). From $\Gamma_1 \nabla = \nabla$ we have $\langle \nabla^T \mathbf{H} \nabla \boldsymbol{\chi}_j \cdot \boldsymbol{\chi}_k \rangle = \langle \Gamma_1 \mathbf{H} \Gamma_1 \nabla \boldsymbol{\chi}_j \cdot \nabla \boldsymbol{\chi}_k \rangle$. Exactly as in Appendix E, these formulas lead to generalizations of equations (E1)–(E14), with appropriate notational changes for the rank-deficient setting. In the case that the matrix ∇ is of full-rank, we have $\mathbf{U}_1 = \mathbf{U}$ hence $\mathbf{W}_1 = \mathbf{W}$, which establishes that the mathematical framework discussed in this paragraph generalizes the mathematical framework in Appendix E for the full-rank setting.

We now establish that these two different approaches provide equivalent spectral representations for the effective diffusivity matrix \mathfrak{D}^* for the rank-deficient setting. In equation (E9) of Theorem 8 we wrote the eigenvalue decomposition $\Gamma = \mathbf{P} \mathbf{G} \mathbf{P}^T$, where \mathbf{P} is an orthogonal matrix and \mathbf{G} is a diagonal matrix. Moreover, we wrote $\mathbf{P} = [\mathbf{P}_0 \ \mathbf{P}_1]$, where the columns of the matrices \mathbf{P}_0 and \mathbf{P}_1 are orthonormal eigenvectors that span the null space and range of Γ , respectively. Since the eigenvalues γ_n associated with the eigenvectors in the matrix \mathbf{P}_1 satisfy $\gamma_n = 1$, any linear combination of the corresponding eigenvectors is also an eigenvector of Γ with eigenvalue $\gamma_n = 1$. Therefore, since the orthonormal columns of the matrix \mathbf{U}_1 span the range of $\Gamma_1 = \mathbf{U}_1 \mathbf{U}_1^T$, we may take $\mathbf{P}_1 = \mathbf{U}_1$ so that $\mathbf{P} = [\mathbf{P}_0 \ \mathbf{U}_1]$. Consequently, we can rewrite equation (E11) as $\mathbf{U}_1^T \mathbf{H} \mathbf{U}_1 = i \mathbf{R}_{11} \Lambda_{11} \mathbf{R}_{11}^\dagger$. Identifying the notations of Appendix E with the current section, we have $\mathbf{R}_{11} = \mathbf{R}_1$ and $\Lambda_{11} = \Lambda_1$. This and equation (E12) establish that $\tilde{\Lambda} = \text{diag}(\mathbf{O}_{00}, \Lambda_1)$.

We now establish that the spectral weights associated with each approach are identical. Using the notation of the present section, equation (E12) yields $\mathbf{W}_1 = [\mathbf{P}_0 \ \mathbf{U}_1 \mathbf{R}_1]$. Consequently, from $\nabla = \mathbf{U}_1 \Sigma_1 \mathbf{V}_1^T$, $\mathbf{U}_1^T \mathbf{U}_1 = \mathbf{V}_1^T \mathbf{V}_1 = \mathbf{I}_1$, and the formula $\mathbf{Z}_1 = \mathbf{V}_1 \Sigma_1^{-1} \mathbf{R}_1$ in (G5), we have that $\nabla \mathbf{Z}_1 = \mathbf{U}_1 \mathbf{R}_1$, implying equation (G6), which is a generalization of equation (F5). Equation (G7) now follows from $\Gamma_1^T = \Gamma_1$, $\Gamma_1 \mathbf{P}_0 = \mathbf{O}$, $\Gamma_1 \mathbf{U}_1 = \mathbf{U}_1$, and the formula $\mathbf{u}_j = -\nabla^T \mathbf{H} \mathbf{e}_j$ in (F11). This establishes that the spectral weights associated with both of the approaches discussed in Section IV and Appendix E are identical which, in turn, establishes that both approaches provide equivalent spectral representations of the effective

diffusivity matrix \mathfrak{D}^* . This concludes our proof of Theorem 10 \square .

In Section V, spectral representations of the symmetric \mathfrak{S}^* and antisymmetric \mathfrak{A}^* parts of the effective diffusivity matrix \mathfrak{D}^* are computed for various periodic flows, and spectral characteristics are related to flow geometry and transport properties. We accomplish this by using equation (39) with \mathbf{z}_n and λ_n replaced by $\mathbf{z}_n^1 = \mathbf{V}_1 \Sigma_1^{-1} \mathbf{r}_n^1$ and λ_n^1 , respectively, where $(\lambda_n^1, \mathbf{r}_n^1)$ are eigen-pairs of matrix $-\imath \mathbf{U}_1^T \mathbf{H} \mathbf{U}_1$. We emphasize that this matrix is of size K_1 which is more than a factor of d smaller than the matrix $-\imath \Gamma_1 \mathbf{H} \Gamma_1$. Moreover, we have established that the discrete spectral measure at the heart of the integral representation for \mathfrak{D}^* is given in terms of the *standard* eigenvalues and eigenvectors of $-\imath \mathbf{U}_1^T \mathbf{H} \mathbf{U}_1$, which is a less costly numerical computation than the computation associated with the *generalized* eigenvalue problem [47] in (31). Consequently, in the process of establishing the equivalence of the effective parameter problems discussed in Section IV and Appendix E for the rank-deficient setting, we have also developed a hybrid numerical algorithm that is more efficient at computing the spectral representation of \mathfrak{D}^* than both of the other approaches.

- [1] N. I. Akhiezer. *The Classical Moment Problem*. Oliver & Boyd, 1965.
- [2] G. S. Aslanyan, I. L. Maikov, and I. Z. Filimonova. Simulation of pulverized coal combustion in a turbulent flow. *Combust., Expl., Shock Waves*, 30(4):448–453, 1994.
- [3] M. Avellaneda and A. Majda. Stieltjes integral representation and effective diffusivity bounds for turbulent transport. *Phys. Rev. Lett.*, 62:753–755, 1989.
- [4] M. Avellaneda and A. Majda. An integral representation and bounds on the effective diffusivity in passive advection by laminar and turbulent flows. *Comm. Math. Phys.*, 138:339–391, 1991.
- [5] M. Avellaneda and M. Vergassola. Stieltjes integral representation of effective diffusivities in time-dependent flows. *Phys. Rev. E*, 52(3):3249–3251, 1995.
- [6] G. A. Baker and P. R. Graves-Morris. *Padé Approximants*. Encyclopedia of Mathematics and its Applications. Cambridge University Press, 1996.
- [7] A. Bensoussan, J.-L. Lions, and G. Papanicolaou. *Asymptotic Analysis for Periodic Structures*. North-Holland, Amsterdam, 1978.
- [8] D. J. Bergman. Exactly solvable microscopic geometries and rigorous bounds for the complex dielectric constant of a two-component composite material. *Phys. Rev. Lett.*, 44:1285–1287,

1980.

- [9] R. Bhattacharya. Multiscale diffusion processes with periodic coefficients and an application to solute transport in porous media. *Ann. Appl. Probab.*, 9(4):951–1020, 1999.
- [10] R. N. Bhattacharya, V. K. Gupta, and H. F. Walker. Asymptotics of solute dispersion in periodic porous media. *SIAM J. Appl. Math.*, 49(1):86–98, February 1989.
- [11] L. Biferale, A. Crisanti, M. Vergassola, and A. Vulpiani. Eddy diffusivities in scalar transport. *Phys. of Fluids*, 7:2725–2734, 1995.
- [12] R. W. Bilger, S. B. Pope, K. N. C. Bray, and J. F. Driscoll. Paradigms in turbulent combustion research. *Proc. Combust. Inst.*, 30:21–42, 2005.
- [13] J. Bonn and R. M. McLaughlin. Sensitive enhanced diffusivities for flows with fluctuating mean winds: a two-parameter study. *J. Fluid Mech.*, 445:345–375, 10 2001.
- [14] J. W. Demmel. *Applied Numerical Linear Algebra*. SIAM, 1997.
- [15] E. Di Lorenzo, D. Mountain, H. P. Batchelder, N. Bond, and E. E. Hofmann. Advances in marine ecosystem dynamics from US GLOBEC: The horizontal-advection bottom-up forcing paradigm. *Oceanography*, 26(4):22–33, 2013.
- [16] R. Durrett. *Probability: Theory and Examples*. 4th Edition. Cambridge University Press, 2010.
- [17] A. Fannjiang and G. Papanicolaou. Convection enhanced diffusion for periodic flows. *SIAM J. Appl. Math.*, 54(2):333–408, 1994.
- [18] A. Fannjiang and G. Papanicolaou. Convection-enhanced diffusion for random flows. *J. Stat. Phys.*, 88(5-6):1033–1076, 1997.
- [19] G. B. Folland. *Introduction to Partial Differential Equations*. Princeton University Press, Princeton, NJ, 1995.
- [20] G. B. Folland. *Real Analysis: Modern Techniques and Their Applications*. Wiley–Interscience, New York, NY, 1999.
- [21] K. M. Golden, H. Eicken, A. L. Heaton, J. Miner, D. Pringle, and J. Zhu. Thermal evolution of permeability and microstructure in sea ice. *Geophys. Res. Lett.*, 34:L16501 (6 pages and issue cover), 2007.
- [22] K. M. Golden and G. Papanicolaou. Bounds for effective parameters of heterogeneous media by analytic continuation. *Commun. Math. Phys.*, 90:473–491, 1983.
- [23] Y. Gorb, D. Nam, and A. Novikov. Numerical simulations of diffusion in cellular flows at high Péclet numbers. *Discrete Contin. Dyn. Syst. Ser. B*, 15(1):75–92, 2011.

- [24] E. E. Hofmann and E. J. Murphy. Advection, krill, and Antarctic marine ecosystems. *Antarct. Sci.*, 16(04):487–499, 12 2004.
- [25] R. A. Horn and C. R. Johnson. *Matrix Analysis*. Cambridge University Press, 1990.
- [26] M. B. Isichenko and J. Kalda. Statistical topography II. 2D transport of passive scalar. *J. Nonlinear Sci.*, 4:375–397, 1991.
- [27] J. D. Jackson. *Classical Electrodynamics*. John Wiley and Sons, Inc., New York, 1999.
- [28] J. P. Keener. *Principles of Applied Mathematics: Transformation and Approximation*. Advanced book program. Westview Press, Cambridge, MA, 2000.
- [29] D. Khoshnevisan. *Probability*. Graduate studies in mathematics. American Mathematical Society, 2007.
- [30] N. Kraitzman, R. Hardenbrook, N. B. Murphy, E. Cherkaev, J. Zhu, and K. M. Golden. Bounds on convection enhanced thermal transport in sea ice. preprint, 2019.
- [31] J. V. Lukovich, D. G. Babb, and D. G. Barber. On the scaling laws derived from ice beacon trajectories in the southern Beaufort Sea during the International Polar Year — Circumpolar Flaw Lead study, 2007–2008. *J. Geophys. Res.-Oceans*, 116(C9):C00G07 (16pp.), 2011.
- [32] V. I. Lytle and S. F. Ackley. Heat flux through sea ice in the Western Weddell Sea: Convective and conductive transfer processes. *J. Geophys. Res.*, 101(C4):8853–8868, 1996.
- [33] A. Majda and P. R. Kramer. *Simplified Models for Turbulent Diffusion: Theory, Numerical Modelling, and Physical Phenomena*. Physics reports. North-Holland, 1999.
- [34] A. J. Majda and P. E. Souganidis. Large scale front dynamics for turbulent reaction-diffusion equations with separated velocity scales. *Nonlinearity (Bristol)*, 7(1):1–30, 1994.
- [35] D. McLaughlin, G. Papanicolaou, and O. Pironneau. Convection of microstructure and related problems. *SIAM J. Appl. Math.*, 45:780–797, 1985.
- [36] R. M. McLaughlin and M. G. Forest. An anelastic, scale-separated model for mixing, with application to atmospheric transport phenomena. *Phys. of Fluids*, 11(4):880–892, 1999.
- [37] R. C. McOwen. *Partial differential equations: methods and applications*. Prentice Hall PTR, 2003.
- [38] Y. A. Melnikov and M. Y. Melnikov. *Green's Functions: Construction and Applications*. De Gruyter studies in mathematics. De Gruyter, 2012.
- [39] G. W. Milton. Bounds on the complex dielectric constant of a composite material. *Appl. Phys. Lett.*, 37:300–302, 1980.

- [40] G. W. Milton. *Theory of Composites*. Cambridge University Press, Cambridge, 2002.
- [41] H. K. Moffatt. Transport effects associated with turbulence with particular attention to the influence of helicity. *Rep. Prog. Phys.*, 46(5):621–664, 1983.
- [42] N. B. Murphy, E. Cherkaev, C. Hohenegger, and K. M. Golden. Spectral measure computations for composite materials. *Commun. Math. Sci.*, 13(4):825–862, 2015.
- [43] N. B. Murphy, E. Cherkaev, J. Xin, and K. M. Golden. Spectral measures and iterative bounds for effective diffusivity for periodic flows. In Preparation, 2019.
- [44] N. B. Murphy, E. Cherkaev, J. Xin, J. Zhu, and K. M. Golden. Spectral analysis and computation of effective diffusivities in space-time periodic incompressible flows. *Ann. Math. Sci. Appl.*, 53:3–66, 2017.
- [45] N. Benjamin Murphy, Elena Cherkaev, and Kenneth M. Golden. Anderson transition for classical transport in composite materials. *Phys. Rev. Lett.*, 118:036401, January 2017.
- [46] G. Papanicolaou and S. Varadhan. Boundary value problems with rapidly oscillating coefficients. In *Colloquia Mathematica Societatis János Bolyai 27, Random Fields (Esztergom, Hungary 1979)*, pages 835–873. North-Holland, 1982.
- [47] B. N. Parlett. *The Symmetric Eigenvalue Problem*. Prentice-Hall, Inc., Upper Saddle River, NJ, USA, 1998.
- [48] G. A. Pavliotis. *Homogenization theory for advection-diffusion equations with mean flow*. PhD thesis, Rensselaer Polytechnic Institute Troy, New York, 2002.
- [49] G. A. Pavliotis. Asymptotic analysis of the Green–Kubo formula. *IMA J. Appl. Math.*, 75:951–967, 2010.
- [50] N. Peters. *Turbulent Combustion*. Cambridge Monographs on Mechanics. Cambridge University Press, 2000.
- [51] P. Rampal, J. Weiss, D. Marsan, and M. Bourgoin. Arctic sea ice velocity field: General circulation and turbulent-like fluctuations. *J. Geophys. Res.-Oceans*, 114(C10):C10014 (17pp.), 2009.
- [52] P. Rampal, J. Weiss, D. Marsan, R. Lindsay, and H. Stern. Scaling properties of sea ice deformation from buoy dispersion analysis. *J. Geophys. Res.-Oceans*, 113(C3):C03002 (12pp.), 2008.
- [53] M. C. Reed and B. Simon. *Functional Analysis*. Academic Press, San Diego CA, 1980.
- [54] W. Rudin. *Real and Complex Analysis*. McGraw-Hill, Inc., New York, NY, 1987.

- [55] P. J. Samson. Atmospheric transport and dispersion of air pollutants associated with vehicular emissions. In A. Y. Watson, R. R. Bates, and D. Kennedy, editors, *Air Pollution, the Automobile, and Public Health*, pages 77–97. National Academy Press (US), 1988.
- [56] I. Stakgold. *Boundary Value Problems of Mathematical Physics*. Classics in Applied Mathematics. SIAM, 2000. 2-volume set.
- [57] T.-J. Stieltjes. Recherches sur les fractions continues. *Annales de la faculté des sciences de Toulouse*, 4(1):J1–J35, 1995.
- [58] M. H. Stone. *Linear Transformations in Hilbert Space*. American Mathematical Society, Providence, RI, 1964.
- [59] R. J. Tabaczynski. Turbulent flows in reciprocating internal combustion engines. In J. H. Weaving, editor, *Internal Combustion Engineering: Science & Technology*, pages 243–285. Springer Netherlands, 1990.
- [60] G. I. Taylor. Eddy motion in the atmosphere. *Philos. Trans. Royal Soc. A*, 215(523–537):1–26, 1915.
- [61] G. I. Taylor. Diffusion by continuous movements. *Proceedings of the London Mathematical Society. Third Series*, 2:196–211, 1921.
- [62] H. J. Trodahl, S. O. F. Wilkinson, M. J. McGuinness, and T. G. Haskell. Thermal conductivity of sea ice; dependence on temperature and depth. *Geophys. Res. Lett.*, 28(7):1279–1282, 2001.
- [63] W. M. Washington and C. L. Parkinson. *An Introduction to Three-Dimensional Climate Modeling*. University Science Books, 1986.
- [64] E. Watanabe and H. Hasumi. Pacific water transport in the western Arctic Ocean simulated by an eddy-resolving coupled sea ice–ocean model. *J. Phys. Oceanogr.*, 39(9):2194–2211, 2009.
- [65] F. A. Williams. *Turbulent Combustion*, chapter 3, pages 97–131. Frontiers in Applied Mathematics. Society for Industrial and Applied Mathematics, SIAM, 3600 Market Street, Floor 6, Philadelphia, PA 19104, 1985.
- [66] J. Xin. *An Introduction to Fronts in Random Media*. Surveys and Tutorials in the Applied Mathematical Sciences. Springer New York, 2009.